

Spin Structure Function g_1 of the Deuteron

Nicholas David Kvaltine
Gainesville, Florida

Bachelor of Science in Physics, University of Florida, 2006
Bachelor of Arts in Mathematics, University of Florida, 2006
Master of Arts in Physics, University of Virginia, 2011

A Dissertation presented to the Graduate Faculty
of the University of Virginia in Candidacy for the Degree of
Doctor of Philosophy

Department of Physics

University of Virginia
August, 2013

Abstract

Previous scattering measurements in the 1980's revealed that the spin of the proton is not primarily the result of the valence quarks' spins. Since then, polarized scattering experiments have attempted to shed light on the source of the nucleon's spin. EG1-DVCS, an experiment run in Hall B at Jefferson Lab, took data on protons and deuterons, accumulating in excess of 27 billion events. This dissertation details the experimental setup and analysis of this data set for inclusive scattering on the deuteron. The spin structure function g_1^d is evaluated in the Q^2 range from 0.7 GeV² to 5 GeV². Results show substantially reduced errors and agreement with previous measurements.

Acknowledgements

As the old saying goes, “No man is an island”. This is surely true in physics, so I’d like to take a moment to send out some thanks.

Firstly, I’d like to thank my parents for all of their love and support. They may not understand what I do, but I wouldn’t have been able to do it without them.

Having a good set of comrades is vital to maintaining your sanity throughout the PhD program. In particular, I’d like to thank Petey. He was an invaluable source of physics knowledge as well as companionship, and basically dragged me through the qualifying exam. I could not have done it without him. Sucheta, who also got her PhD from eg1-dvcs, was an asset not just to me, but to the whole eg1-dvcs collaboration. She also became a good friend, and has been another integral piece in my PhD experience. James and Jonathan deserve thanks as my senior graduate students. They have been my role models in this venture, whether they realize it or not, and I appreciate everything they taught me. Additionally, I was lucky enough to have an excellent group of students in my year. I wish all of them the best in their future endeavors.

A number of people have provided an important advisory role to me. Of course, my actual advisor Don Crabb was a huge help as well as Donal Day, a sort of second advisor. When it comes to the analysis, two people were the most important in helping me through this: Peter and Yelena. Yelena Prok is one of Don’s former

Table 1: People to whom thanks should be extended

Family	Friends	Faculty	Staff
Mom	Petey	Don	Dawn
Dad	Sucheta	Peter Bosted	Tammie
	James	Yelena	B.H.
	Jonathan		Dave
			Beth
			Helen
			Suzie

students and was intimately familiar with the subject of my work. Peter Bosted is widely known at JLab, and for good reason. His depth and breadth of knowledge of nuclear physics is astounding. Josh and Nadia, other former students of Don and Donal's, were helpful in various ways, as well as Chris Keith and Chris Carlin from the Target Group at JLab.

I couldn't properly thank everyone without including the staff at UVA. They are instrumental in shepherding all of us students along and they keep the department running smoothly despite the best efforts of the faculty and students. Dawn, Tammie, Suzie, Helen, and Chris deserve particular mention. They have been there to chat and keep me sane through all the long hours. I'd be remiss if I didn't also thank Dave and B.H. These guys are a great source of entertaining conversations and I'll miss them when I leave.

I could not include everyone who had a hand in helping me graduate or my acknowledgements would be the longest chapter of my dissertation. I'm really grateful to everyone though; even if you aren't listed in Table 1 please know your help was appreciated.

Contents

I	Introduction	1
1	Historical Background	3
2	Motivation, Theory, and Formalism	6
2.1	Motivation	6
2.2	Theory and Formalism	8
2.2.1	Inclusive Scattering	8
2.2.2	Form Factors	10
2.2.3	Structure Functions	12
II	The Experiment	18
3	CEBAF	19
3.1	Polarized Electron Source	20
3.2	Accelerator	21
4	CLAS	23
4.1	Torus Magnet	25
4.2	Inner Calorimeter	29
4.3	Drift Chambers	31

4.4	Cherenkov Counter	34
4.5	Scintillator Counter	36
4.6	Electromagnetic Calorimeter	37
4.7	Trigger and Data Acquisition	39
5	Polarized Target	40
5.1	Dynamic Nuclear Polarization	41
5.1.1	Solid State Effect	42
5.1.2	Equal Spin Temperature Theory	43
5.1.3	Spin 1	45
5.1.4	Polarization Measurement	48
5.2	Target Apparatus	52
5.3	Ammonia	65
5.3.1	Freezing	65
5.3.2	Irradiation	66
5.3.3	Anneals	67
6	eg1-dvcs	69
6.0.4	Experimental Overview	69
6.0.5	Experimental Context	71
III	The Analysis	73
7	Data	74
7.1	Processing	75
7.2	Post-Processing	75
7.3	Calibrations	77

7.3.1	Standard Calibrations	77
7.3.2	Raster Corrections	78
7.3.3	Magnet Angle Correction	78
7.4	Event Selection/Particle Identification	79
7.5	Quality Checks	86
7.5.1	Beam Scraping	86
7.5.2	Rate Stability	86
7.5.3	Asymmetry Stability	87
7.5.4	Electron Detection Efficiency	89
7.5.5	Ad-hoc Momentum and Angle Corrections	90
7.5.6	Beam Energy	91
8	Asymmetry	93
8.1	Double Spin Asymmetry	93
8.2	Raw Asymmetry	94
8.3	Beam and Target Polarization ($P_b P_t$)	95
8.3.1	Deuteron Target Calibration	96
8.3.2	Proton Contamination Polarization	101
8.4	Dilution Factor	103
8.4.1	Target Length L (Length Between Banjo Windows)	106
8.4.2	Ammonia Length l_A (Packing Fraction)	108
8.4.2.1	Raster Correction to the Effective Length of ND_3	109
8.4.3	Scattering Measurement of Hydrogen Contamination in ND_3	111
8.4.4	NMR Measurement of Hydrogen Contamination in ND_3	115
8.4.5	Results	122
8.5	Pion and Pair-Symmetric Correction	122

8.6	Contribution from Polarized Nitrogen (c_1)	126
8.7	Correction for NH_3 in ND_3 (c_2)	129
8.8	Radiative Corrections	130
9	Results	135
9.1	g_1/F_1	135
9.1.1	$A_{ }$	136
9.1.2	Depolarization Factor and R	137
9.1.3	g_2 Correction	138
9.1.4	Combining Data Sets	139
9.2	Systematic Errors	140
9.2.1	R	140
9.2.2	Dilution Factor Systematics	140
9.2.3	Luminosity Dependence of Detection Efficiency	141
9.2.4	Error from beam charge asymmetry	143
9.2.5	Parity-violating background	144
9.3	Physics Results	144
9.3.1	g_1/F_1 as a function of W in bins of Q^2	144
9.3.2	Results and Discussion	145
	Appendix:	146
	A Deuteron Polarization Calibration Data	149

Part I

Introduction

Call me Stache-mael. Some years ago - never mind how long precisely - having little or no money and a particular interest in physics, I thought I would study a little and see the mathematical part of the world. [1]

Literary references aside, I began graduate school approximately 7 years ago and in that time I've learned a bit about physics, though I still have little to no money. This dissertation contains a description of all parts of my "thesis topic" but it assumes a depth and breadth of knowledge that will exceed most people. I will begin with a short historical background, starting from the development of atomic theory and ending with the parton model where it is relevant to my experiment. The motivation and theoretical aspects of this work round out the introduction and are followed by in-depth discussion of the experimental setup and the analysis.

Chapter 1

Historical Background

The foundations of atomic theory were laid by the chemists beginning in the late 1700's and lasting throughout the 1800's. The Law of Conservation of Mass was formulated by Antoine Lavoisier in 1789, along with a rudimentary periodic table, and in the next decades observations regarding the proportions of elements produced by chemical extraction were described. In 1805, John Dalton suggested that elements were composed of indivisible "atoms" of a particular type and had a substantial amount of evidence to support the proposition. Over the next 5 decades, the atomic theory was expanded and revised; Mendeleev's periodic table, the direct precursor to our modern one, was published in 1869.

While chemists had been successful in elucidating the chemical nature of atoms, they were thought to be indivisible. In 1897, JJ Thomson is credited with discovering the electron while working with cathode rays. His theory was that electrons, which he showed to be negatively charged, were embedded in a sea of positive charge (the Plum Pudding Model) resulting in a neutral atom. A mere 12 years later, Ernest Rutherford, a student of Thomson's, directed the classic "gold foil experiment" which would show that the charge and mass of an atom were concentrated in a small "nu-

cleus". The resulting model of the atom, that of the positively charge nucleus with orbiting electrons, was at odds with established physics, namely that accelerating charged particles should radiate energy, and thus collapse the atom. An increasingly accurate model was developed by Neils Bohr by using the recently postulated discrete (quantum) nature of light. An unsatisfactory explanation for many reasons, it would be enhanced with the development of quantum mechanics. At this point, the understanding of the atom is nearly complete. Isotopes, elements with the same chemical properties but different atomic weights, were discovered in 1913, but the discovery of the neutron would wait until 1932. It was also 1932 that the deuteron, the focus of the experiment described in this dissertation, was discovered through fractional distillation of hydrogen and spectroscopy [2].

In the mean time, particle physics was also developing. Paul Dirac's relativistic quantum theory required negative energy solutions, which he eventually predicted to be anti-electrons [3]. This prediction, made in 1931, would be confirmed in 1932 using a cloud chamber and cosmic rays. Particle accelerators had not yet invented, so the discovery of the pion in 1947 was also made using cosmic rays and photographic plates. There were found to be three kinds of pions: positive, negative, and neutral. With the advent of accelerators, a plethora of new particles were discovered. Originally developed as a convenient organizing scheme for these new particles, the quark model was validated by scattering experiments which showed that the proton was not point-like, and instead composed of discrete particles. These quarks have fractional charge and can not exist alone: three are found in each proton and neutron, and 2 in each meson like the pion. Gluons, the carrier for the force which confines quarks in a nucleon (a nucleon is a proton or a neutron), are also considered in the parton model. The current state of particle physics, the so-called "Standard Model", includes 3 generations of particles, divided between leptons, quarks, and force carriers. See Fig. 1.1.

Chapter 2

Motivation, Theory, and Formalism

2.1 Motivation

In the enduring quest to understand the nature of nature, we have penetrated far beyond the regime where simple observations by the unaided human senses could provide deeper knowledge. Even the most advanced light microscopes are unable to image an atom, since the resolving power is limited by the wavelength of the light used as a probe. The discovery of quantum mechanics provided a means to access smaller features; since all particles are also waves it is possible to investigate the structure of matter at a smaller scale using matter itself.

Electron scattering is not as straightforward as using a light microscope. To interpret the results of scattering experiments, a theory of the interaction of particles is required. For electromagnetism alone, Quantum Electrodynamics (QED) provides one of the most accurate theories in physics. Interactions within the nucleon require a more complicated theory, Quantum Chromodynamics (QCD). QED tells us that any interaction with an electron is mediated by the force carrier, the photon. Fig. 2.1 shows an example of how an elastic collision would be depicted. As an example,

consider that the photon from a 5 GeV electron that is detected with 1 GeV after scattering would have a wavelength of approximately 10^{-17} m [4]. The proton is about 10^{-15} m in size, so this scattering event, easily in the range produced at Jefferson Lab, has enough resolution to investigate the internal structure of the proton.

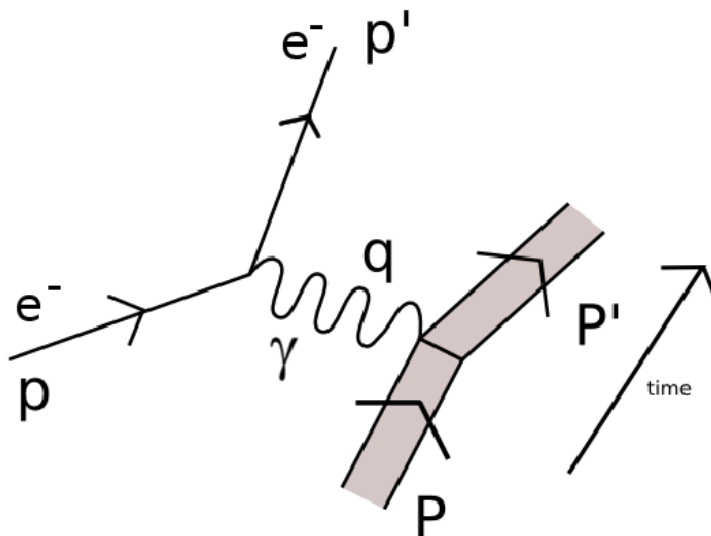


Figure 2.1: An example of an electron elastically scattering from a proton. Image courtesy of J. Mulholland [4]

Although the electron and photon interactions are well described by QED, the dynamics of the interaction with the nucleon must come from QCD. Unfortunately, the calculations which can be done from first principles using QCD are few and far between. Some conclusions can be made about the nucleon's structure however; the mathematical details will be described in section 2.2. One of the details of the nucleon's structure that is of interest is the source of its spin. This became a topic of intense research when experiments showed that the spin of the quarks themselves contribute very little to the spin of the nucleon. This is the so-called “spin crisis”, alternatively known by the less hyperbolic name “spin puzzle”. Subsequent tests of the original findings suggest that gluons as well as the orbital angular momentum

of the quarks all contribute significantly to the proton's spin. The subject of this dissertation, the spin structure function g_1 of the deuteron, is a means to shed light on this puzzle. g_1 is also able to test QCD via the Bjorken sum rule, which is a strict QCD prediction [5]

2.2 Theory and Formalism

This chapter is intended to provide the theoretical underpinnings for the analysis which is the main topic of this dissertation. A brief description of inclusive scattering will be given, followed by an explanation of how information about the nucleon can be obtained from cross sections and asymmetries.

2.2.1 Inclusive Scattering

Inclusive scattering refers to scattering events in which only an electron is detected in the final state. Often written like $ep \rightarrow e'X$, with X representing the rest of the unknown final state, inclusive scattering encompasses a range of processes which vary based on energy. At lower energy transfers, elastic scattering occurs, and the only other particle in the final state is the struck nucleon. In that case, the kinematics of the nucleon are precisely determined from the measured kinematics of the electron. In the resonance region, enough energy is transferred to excite some of the nucleon resonance states. Beyond the resonance region, the structure functions, discussed later, smooth out and their dependence on energy transfer is more amenable to analysis. This is the Deep Inelastic Scattering (DIS) region and is where most of the data for the experiment described herein was taken.

The energy transfer, discussed above, has a well-defined meaning for inclusive scattering. There are also several other variables which are useful for discussing inclusive

scattering. p^μ is the 4-momentum of the incident electron, p'^μ the 4-momentum of the outgoing final-state electron, and the \hat{z} direction taken to be along the beam. The difference between the electron's incoming and outgoing momentum is q^μ . Some definitions of useful variables are:

$$Q^2 = -q^\mu q_\mu = 2EE'(1 - \cos\theta) \quad (2.1)$$

$$\nu = E - E' = \frac{p \cdot q}{M} \quad (2.2)$$

$$x_{bj} = \frac{Q^2}{2p \cdot q} = \frac{Q^2}{2M\nu} \quad (2.3)$$

$$W = \sqrt{(p + q)^2} = \sqrt{M^2 + 2M\nu - Q^2} \quad (2.4)$$

$$y = \frac{E - E'}{E} = \frac{\nu}{E} \quad (2.5)$$

The momentum transfer squared, Q^2 , is the variable used most often when discussing the energy ranges of experiments or the scale of scattering. It can also be considered as the mass of the photon exchanged by the electron. In the limit $Q^2 \rightarrow 0$, it is a real photon. The energy transfer, ν , is also used when discussing the scale of interaction since it is the energy carried by the virtual photon that is probing the nucleon. x_{bj} is referred to as Bjorken x , and is in fact often written as just “ x ”. x is an important variable, but its interpretation is more complicated. First, the “Breit Frame” must be defined. The Breit frame is a reference frame where $\nu = 0$; since the virtual photon is carrying no energy, the momentum of the struck quark in the \hat{z}

direction must not change in magnitude. Since it does acquire a change in momentum q , we see that its direction must reverse. Using this information, it becomes obvious that x represents the fraction of the nucleon's momentum that is carried by the struck quark (in the Breit frame). The variable W is the “missing mass”, so-called because it is simply the invariant mass of part of the final state which is not detected. It is calculated from 4-momentum conservation. The resonance region, as discussed earlier, is seen as peaks in cross-section centered on the mass of the state in W .

2.2.2 Form Factors

The ideas used for scattering in quantum field theory (QFT) stem from analogous ideas from quantum mechanics. The “form factor” can be used to extend scattering from point charges to extended sources. The scattering of a particle is described by Fermi's golden rule:

$$w = \frac{2\pi}{\hbar} |M_{if}|^2 \rho_f \quad (2.6)$$

where w is the scattering probability per unit time, M_{if} is the transition matrix element between initial and final states, and ρ_f is the density of final states [6]. The matrix element M_{if} can be approximated with perturbation theory when the potential is small, like so:

$$M_{if} = \int \psi_f^* V \psi_i \, d\tau \quad (2.7)$$

It can be shown that the matrix element amounts to a Fourier transform of the perturbation. With a charge distribution with spatial extent $\rho(R)$, the perturbation is a convolution of $\rho(R)$ and $V(r - R)$, so then the convolution theorem tells us

the matrix element is a product of the Fourier transform of V and a function $F(q^2)$ which is called the “Form Factor.” The charge distributions of many nuclei have been measured using the form factor derived from scattering over a range of momentum transfer q^2 .

The Quantum Field Theoretical derivation of the formula for the cross-section is more involved than is appropriate in this context; see [7]. The salient point is that the entirety of the physics of an interaction is contained in the scattering matrix, similar to the previous discussion. For example, the matrix element for electron scattering from heavy point-like fermions is:

$$M = e^2[\bar{u}(p')\gamma^\mu u(p)]\frac{1}{p}[\bar{u}(P')\gamma_\mu u(P)] \quad (2.8)$$

where $u(k)$ is the Dirac spinor for a fermion with 4-momentum k [8]. The first term in brackets results from the electron-photon vertex, and the second is the fermion-photon vertex. This matrix element is calculated from the sum of all the appropriate Feynman diagrams, which is in general an infinite sum. Each additional vertex in the Feynman diagram adds a factor of α , the fine structure constant, however, so it can be considered a perturbation series, and then calculations are generally done up to some particular order of α . Since the nucleon is not a point-like particle, its vertex cannot simply be written as γ_μ . Instead, it is replaced with Γ^μ ; it can be shown using Lorentz invariance, parity, and the Ward identity that it must have the form:

$$\Gamma^\mu = \gamma^\mu F_1(q^2) + \frac{i\sigma^{\mu\nu}q_\nu}{2m} F_2(q^2) \quad (2.9)$$

The two functions, F_1 and F_2 , are the form factors. They can be found by measuring the q^2 dependence of the cross-section and give useful information about the physical process which they represent, e.g. the anomalous magnetic moment of the electron is

related to $f_2(0)$.

2.2.3 Structure Functions

The nucleon interaction is more complicated than a simple interaction between point-like particles, and in general not calculable from first principles. Fortunately, the interaction can be parameterized in the same way as was done with form factors. When considered for the case of inelastic scattering, this results in “structure functions”.

The elastic form factors for nucleons are written as $F_1^N(q^2)$ and $F_2^N(q^2)$ where the N can be p , n , or d for the proton, neutron, or deuteron, respectively. The elastic form factors are also often expressed as the “Sachs Form Factors” [8]:

$$G_E(Q^2) = F_1(Q^2) - \frac{Q^2}{4M^2}F_2(Q^2) \quad (2.10)$$

$$G_M(Q^2) = F_1(Q^2) + F_2(Q^2) \quad (2.11)$$

These are called the electric and magnetic form factors (denoted by the E and M subscripts) because at $Q^2 = 0$, $eG_E^N(0) = q^N$ and $G_M^N(0) = \mu^N$, where the N means either a proton or neutron, q is the charge of the specified nucleon, and μ is the magnetic moment. Similarly to the form factors discussed earlier, the Fourier transforms of these give the charge and magnetization density of the nucleons (in the non-relativistic regime).

The Sachs form factors describe elastic scattering, but the reaction of interest here is inclusive, inelastic scattering. This is more complicated still, due to the indeterminate nature of the final state. The Optical Theorem provides a way around this by relating the matrix for a process to a sum over all the final states. Reference [7] will

provide a more detailed description of the Optical Theorem for enthusiastic readers. Applying the Optical Theorem in this way results in:

$$|M(ep \rightarrow e'X)|^2 = \frac{e^4}{q^4} L_{\mu\nu} W^{\mu\nu} \quad (2.12)$$

where $L_{\mu\nu} = \bar{u}(k')\gamma_\mu u(k)\bar{u}(k)\gamma_\nu u(k')$ is the leptonic tensor and $W^{\mu\nu}$ is the hadronic part of the matrix element. The leptonic tensor becomes

$$L_{\mu\nu} = 2[p_\mu p'_\nu + p'_\mu p_\nu - g_{\mu\nu} p \cdot p'] \quad (2.13)$$

when summed of final states and averaged over initial lepton spin states. The hadronic tensor is parameterized by two functions, W_1 and W_2 :

$$W_{\mu\nu} = (-g_{\mu\nu} + \frac{q_\mu q_\nu}{q^2})W_1(Q^2, \nu) + (P_\mu - q_\mu \frac{P \cdot q}{q^2})(P_\nu - q_\nu \frac{P \cdot q}{q^2}) \frac{W_2(Q^2, \nu)}{M^2} \quad (2.14)$$

These two functions are known as the ‘‘Structure Functions’’ for inclusive, unpolarized electron-nucleon scattering.

The leptonic and hadronic tensors, Eqs. 2.13 and 2.14, are both for unpolarized scattering and include a sum over initial spin states and an average over the final states. Including the spin state explicitly, the leptonic tensor is:

$$L_{\mu\nu} = 2[p_\mu p'_\nu + p'_\mu p_\nu - g_{\mu\nu} p \cdot p' + i\epsilon_{\mu\nu\alpha\beta} s^\alpha q^\beta] \quad (2.15)$$

The difference is the additional imaginary term, which is anti-symmetric in μ and ν . It can be separated into symmetric and anti-symmetric parts:

$$L_{\mu\nu} = L_{\mu\nu}^S + L_{\mu\nu}^A. \quad (2.16)$$

Similarly, the hadronic tensor gains an anti-symmetric imaginary component when including spin:

$$W_{\mu\nu}^A = i\epsilon_{\mu\nu\alpha\beta}q^\alpha[G_a(\nu, Q^2)S^\beta + \frac{G_2(\nu, Q^2)}{M^2}(S^\beta P \cdot q - P^\beta S \cdot q)] \quad (2.17)$$

and can be split into anti-symmetric and symmetric parts:

$$W_{\mu\nu} = W_{\mu\nu}^S + W_{\mu\nu}^A. \quad (2.18)$$

With these tensors split as such, the cross section for polarized scattering is proportional to $L_{\mu\nu}^S W_{\mu\nu}^S + L_{\mu\nu}^A W_{\mu\nu}^A$. The symmetric component is obviously the same as for non-polarized scattering, so the asymmetric component is only amenable to measurement from polarized scattering. Although the structure functions G_1 and G_2 are included in the asymmetric part of the hadronic tensor, it is the “spin structure functions” g_1 and g_2 that are typically discussed when doing polarized DIS. These are defined thusly:

$$g_1(x, Q^2) = M^2\nu G_1(\nu, Q^2) \quad \text{and} \quad (2.19)$$

$$g_2(x, Q^2) = M\nu^2 G_2(\nu, Q^2). \quad (2.20)$$

To separate g_1 and g_2 from the unpolarized structure functions, asymmetries are measured, where the asymmetry is defined as the difference of the cross-section for aligned and anti-aligned particles divided by the sum. This still only gives a linear

combination of g_1 and g_2 however. By also measuring an asymmetry when the beam and target polarizations are at 90° to each other, a different linear combination of g_1 and g_2 is measured, so they can then be extracted separately. To have a polarized target at 90° to the beam requires a more complicated setup, and was not measured during the experiment discussed in this dissertation. A “ g_2 correction” is applied, which utilizes the data from earlier experiments to provide a value for g_2 and thus allow extraction of g_1 , the main topic for this dissertation.

In the quark-parton model, the Structure Functions can be expressed as a sum over partons:

$$F_1(x) = \frac{1}{2x} F_2(x) \quad (2.21)$$

$$F_2(x) = \sum_i e_i^2 x f_i(x) \quad (2.22)$$

where $f_i(x)$ is the momentum distribution of the i^{th} parton. In terms of the quarks present in the nucleon:

$$\frac{1}{x} F_2^{ep}(x) = \left(\frac{2}{3}\right)^2 [u(x) + \bar{u}(x)] + \left(\frac{1}{3}\right)^2 [d(x) + \bar{d}(x)] + \left(\frac{1}{3}\right)^2 [s(x) + \bar{s}(x)] \quad (2.23)$$

where $u(x), d(x)$, and $s(x)$ represent the distributions for the up, down, and strange quarks respectively. Any significant presence of heavier quarks is neglected. The spin structure functions can be parameterized in a similar way to the unpolarized structure functions shown in Eq. 2.23. Instead of the momentum distributions of each quark however, the parameterization is in terms of the spin distribution. Similarly to $f_i(x)$ in Eq. 2.22, functions $f^\uparrow(x)$ and $f^\downarrow(x)$ are defined as the distribution for a quark with

spin parallel or anti-parallel to the nucleon spin. Futhermore, if we then define

$$\Delta f(x) = f^\uparrow(x) - f^\downarrow(x) \quad (2.24)$$

It follows that

$$\frac{\Sigma q_f^2 \Delta f(x)}{\Sigma q_f^2 f(x)} = \frac{g_1}{F_1}. \quad (2.25)$$

From Eq. 2.25 we can infer that g_1 can be interpreted as the sum of the quarks' momentum distributions weighted by their spin distributions. Written explicitly, we have:

$$g_1(x, Q^2) = \frac{1}{2} \Sigma q_f^2 \Delta f(x, Q^2) = \frac{4}{18} \Delta u(x, Q^2) + \frac{1}{18} \Delta d(x, Q^2) + \frac{1}{18} \Delta s(x, Q^2) \quad (2.26)$$

The preceeding equations represent the naive quark-parton model; within this model framework, the structure functions depend only on x (x -scaling). However, at finite values of momentum transfer (Q^2), x -scaling is violated and the structure functions depend on both Q^2 and x . To understand this behavior, it is necessary to use Quantum Chromo Dynamics (QCD).

When it was found, by integrating g_1^p , that the quarks only contribute around 20% of the nucleon spin, it was determined that all sources of spin needed to be accounted for. The total spin is then given by the ‘‘Nucleon Spin Sum Rule’’:

$$S_z^N = S_z^q + L_z^q + J_z^g = \frac{1}{2}, \quad (2.27)$$

where S_z^N is the nucleon spin, S_z^q and L_z^q are the quarks' spin and angular momentum, and J_z^g is the angular momentum of the gluons. In the low and moderate x range,

the sensitivity to sea quarks and gluons is high, as well as in the high Q^2 region. The interactions of the probing photon with the sea quarks and gluons produce an effective reduction of the valence quarks' momentum. Essentially, the momentum of the nucleon is shared between more of its constituents. Thus, the valence quark distribution functions decrease as Q^2 increases. The dependence of the distribution functions on Q^2 is described by the Altarelli-Parisi equations, and exhibit a logarithmic dependence which is due to gluon emission.

There are two sources of Q^2 dependence that occur with QCD: hard gluons, which are accounted for by QCD radiative corrections, and interactions between the quark and the other partons which are considered by higher twist corrections. Using perturbative QCD (pQCD) the complete Q^2 dependent expression for g_1 can be written in terms of polarized quark distribution functions (Δq_i) as well as polarized gluon distribution function (Δg):

$$g_1(x, Q^2) = \frac{1}{2} \sum_i e_i^2 C_q(x, \alpha_s) \otimes \Delta q_i(x, Q^2) + \frac{1}{N_f} C_g(x, \alpha_s) \otimes \Delta g(x, Q^2). \quad (2.28)$$

The number of quark flavors is N_f , and the functions that describe polarized photon-quark and photon-gluon hard scattering are $C_q(x, \alpha_s)$ and $C_g(x, \alpha_s)$.

The dependence of the spin structure function on gluon spins is made clear in Equation 2.28. If $C_q = \delta(1 - x)$ and $C_g = 0$, the naive parton model, written explicitly in Eq. 2.26, is obtained.

Part II

The Experiment

Chapter 3

CEBAF

To perform a scattering experiment, it is necessary to have a source of particles to use as your probe. The probe for the experiment described here is an electron beam, with an energy of approximately 6 GeV. Since this uses a stationary target, as opposed to colliding beams, all of the energy comes from the beam; the 6 GeV provided by the polarized electron beam enables the investigation of the structure of the nucleon. Providing this beam is a feat in itself, and requires a complex apparatus. That apparatus is the Continuous Electron Beam Accelerator Facility (CEBAF).

CEBAF is a racetrack-style recirculating accelerator. It uses superconducting radio frequency cavities along the straight portions of the racetrack to accelerate the beam, and can make up to 5 passes around the track. The beam is considered to be “continuous wave”, which means its duty cycle higher than most accelerators, though the beam still exists as 2 nanoseconds bunches. The beam can provide varying amounts of current to each of the three experimental halls, imaginatively named Hall A, Hall B, and Hall C, by means of three interlaced beams separated by 120° of radio-frequency phase [9]. The beam is also delivered with high polarization. Fig. 3.1 shows a schematic representation of the essential parts of CEBAF.

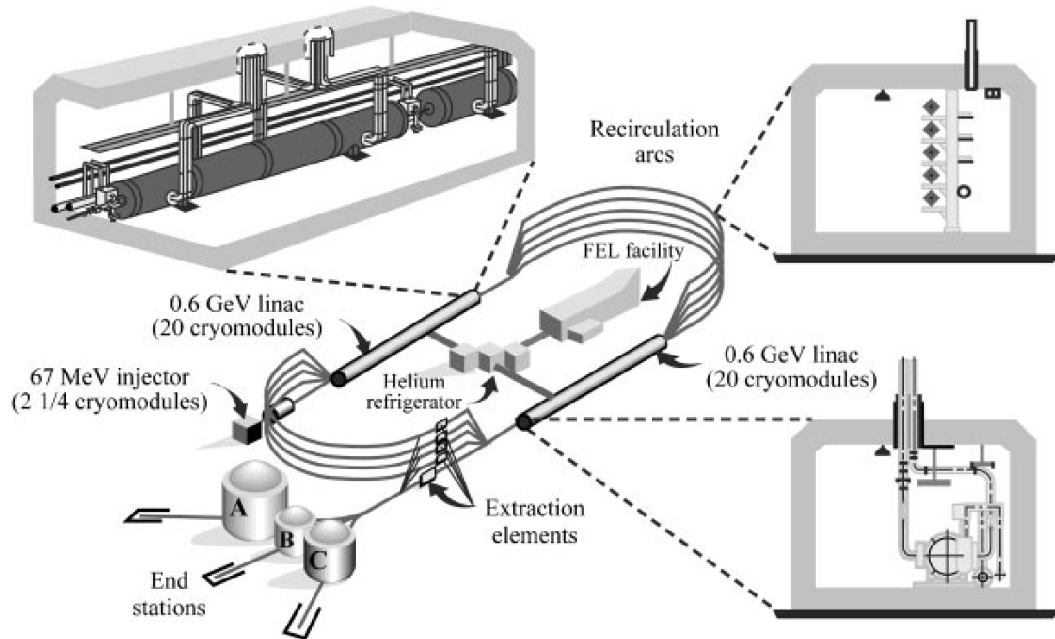


Figure 3.1: A schematic view of CEBAF. [9]

3.1 Polarized Electron Source

CEBAF can provide an electron beam with greater than 80% polarization. To accomplish this, it begins with a polarized electron source. The source is a cathode made from the semi-conductor Gallium Arsenide, which emits electrons when illuminated with laser light at a frequency corresponding to the band gap. If this light is circularly polarized, the resulting electrons will be linearly polarized. The helicity of the electrons can be varied by changing the helicity of the laser. The interaction between the light and the source is depicted in Fig. 3.2. Consider first the case of a regular GaAs source, the source type initially used with CEBAF. The laser can stimulate transitions from both $P_{3/2}$ and $P_{1/2}$ states due to their degeneracy; polarizations of 50% result due to unequal stimulation probabilities [10]. In a strained GaAs crystal, however, the degeneracy is lifted, allowing the light to stimulate only

the $P_{3/2}$ transition, and resulting in much higher polarizations. The crystal can be strained by growing it on a $\text{GaAs}_{0.72}\text{P}_{0.28}$ substrate [10]. The process and effects of the lattice straining are described thoroughly in Ref. [11].

Due to the nature of the transitions, the beam helicity depends directly on the laser helicity. The laser helicity is easily changed using a ‘‘Pockels cell’’, a crystal with electronically variable birefringence [12]. The helicity is flipped pseudo-randomly to help eliminate systematic errors, and a half-wave plate is periodically inserted or removed to accomplish this as well.

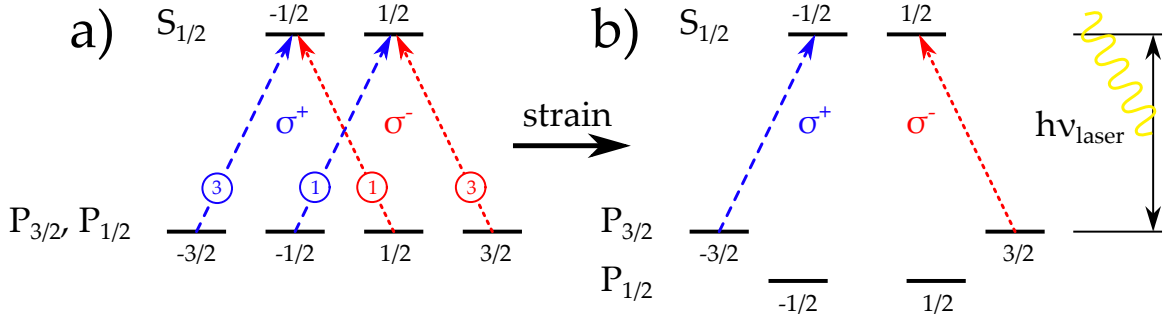


Figure 3.2: The energy levels stimulated by laser light are schematically depicted. a) is the case with normal GaAs and b) shows the difference for strained GaAs. Figure courtesy J. Maxwell [12]

3.2 Accelerator

The accelerating components of CEBAF are located in the straight portions of the racetrack. Polarized electrons from the source are injected at 67 MeV and each pass through a straight section gains about 600 MeV. Although usually 5 passes are made, some experiments require lower energy and can receive the beam after fewer passes.

Due to the increasing momentum of each ‘‘lap’’ around the track, electrons must be split by energy for the recirculating portions. The speed of the electrons does not change around each lap, however, since they are already traveling at the speed of light

upon leaving the injector. This means that the accelerating portions can be used for each energy with no change. Each accelerating portion consists of 20 “cryomodules” each of which are themselves composed of 8 superconducting RF cavities. The cavities are designed to operate at 1497 kHz, such that the 3 halls can each be served with a beam at 499 kHz [9]. Each cavity is supplied by a 5 kW klystron, and they must all be cooled to 2.08 K since power losses increase exponentially with temperature. As a result, a high capacity refrigerator station is required to supply CEBAF with liquid helium.



Figure 3.3: A pair of rf cavities. Each cavity has 5 cells and is 0.5 m in length [9]

Chapter 4

CLAS

CLAS is the nested acronym for CEBAF Large Acceptance Spectrometer. When fully expanded, this reads “Continuous Electron Beam Accelerator Facility Large Acceptance Spectrometer”. CLAS is the detector used in Hall B. It can be used with an electron beam or a photon beam which is produced in the hall from the electron beam. It is also capable of accepting multiple target types, including polarized targets, provided that they will fit. The main components, in the order a particle would intercept them, are the Inner Calorimeter, the Drift Chambers, the Cherenkov Calorimeter, the Scintillation Counter, and the Electromagnetic Calorimeter, all of which will be discussed. The best reference for CLAS information is [13].

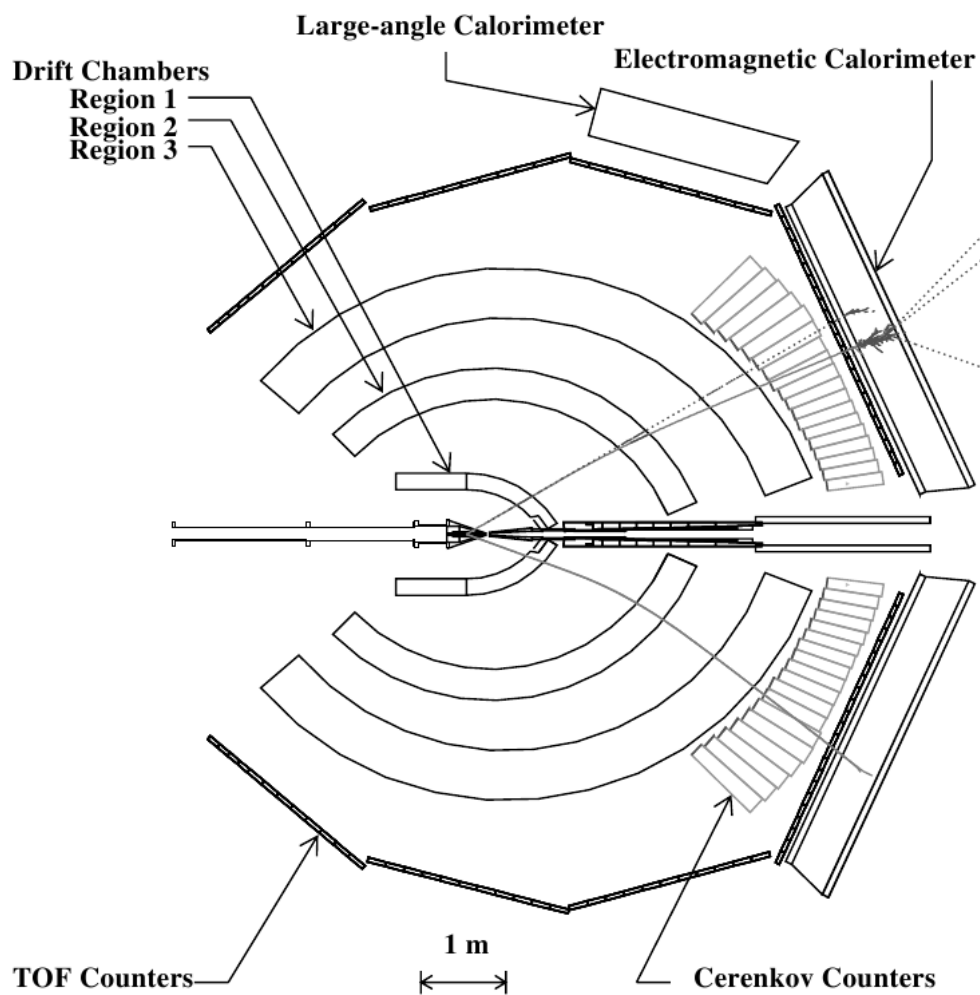


Figure 4.1: A cross-section of CLAS showing the main components with photon, electron, and proton tracks drawn to demonstrate their trajectory through CLAS. [13]

4.1 Torus Magnet

To measure the momentum of charged particles in CLAS, a magnetic field is required. The magnetic field must have a component perpendicular to the velocity of the particle, provided here by a magnetic field that circles the beam line azimuthally. The CLAS Torus provides just such a field, and Fig. 4.3 shows in a cross-section perpendicular to the beam the behavior of the magnetic field. The torus is composed of six segments, which creates a logical way to divide CLAS into six sectors. These segments are superconducting coils encased in their own cryostats, which must be cooled with liquid helium.

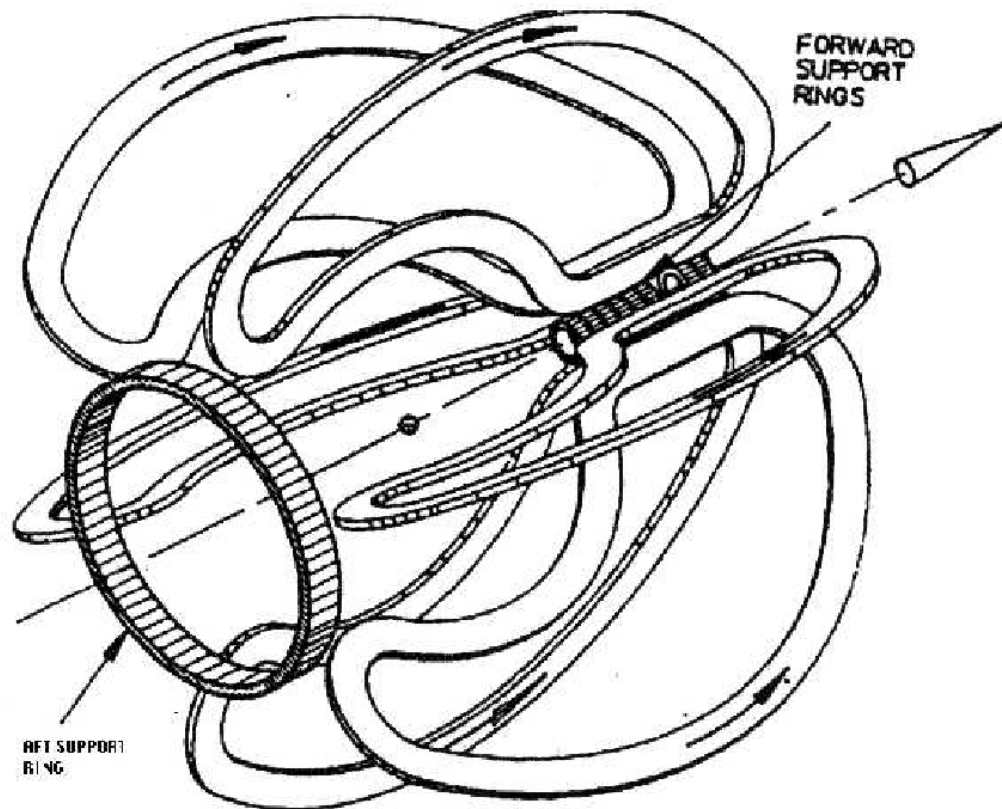


Figure 4.2: A sketch of the CLAS torus magnet. The individual coils divide CLAS into 6 sectors. [10]

Additionally, the configuration of the coils, as seen in Fig. 4.2, provides a “field-free” region at the center of CLAS. This allows for the operation of polarized targets.

During the experimental runs for this experiment, the torus had a current of 2250 Amps. The standard direction of current causes negatively charged particles to curve towards the beam line; this is called “inbending”. Approximately halfway through taking data, the current in the torus is reversed, such that positively charged particles bend inwards; these are “outbending” runs. There are multiple reasons for this: it alters the kinematic coverage, allowing lower Q^2 electrons to be detected, which would otherwise pass through the beam line, and it also allows for comparisons to be made with positrons. This is a useful technique to determine a pair-symmetric correction, as discussed in Sec. 8.5.

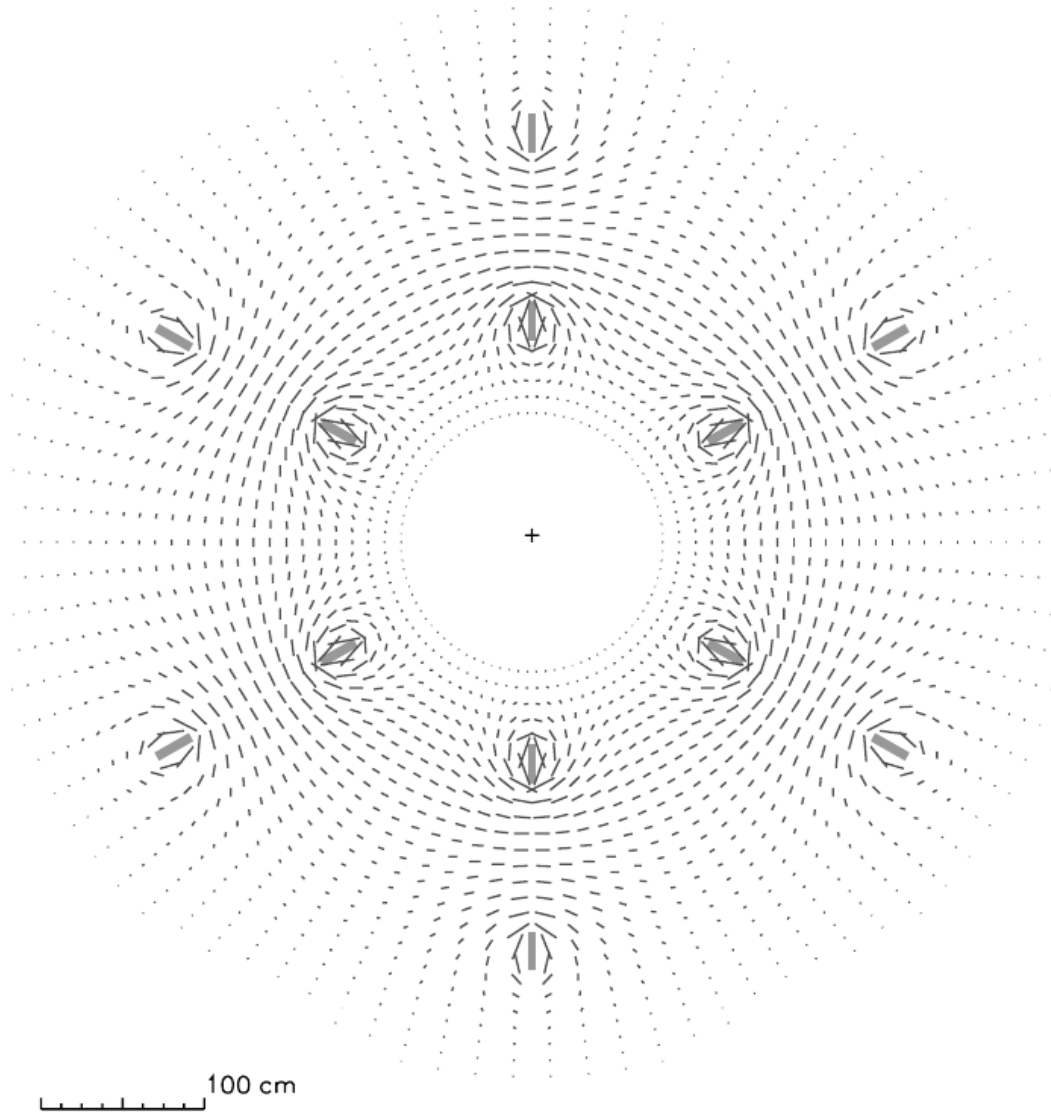


Figure 4.3: Magnetic field vectors for the CLAS toroid transverse to the beam in a plane centered on the target. The length of each line segment is proportional to the field strength at that point. The six coils are seen in cross-section. [13]

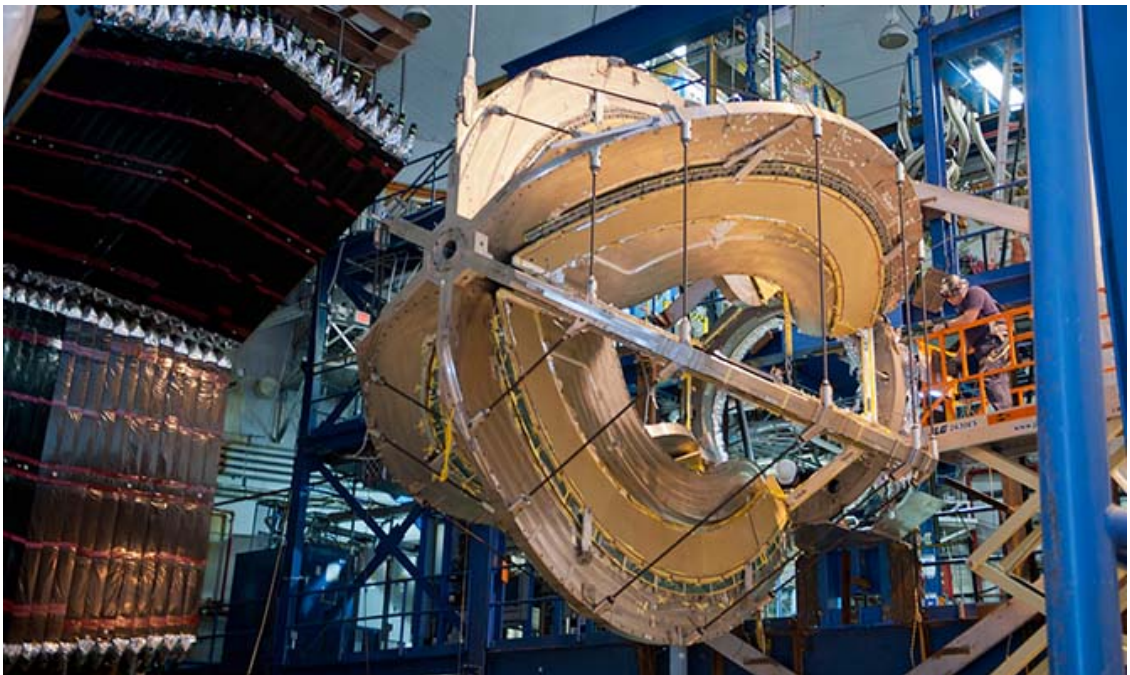


Figure 4.4: The CLAS torus, as it is prepared for disassembly. All six sectors are visible with their supporting rods and retainers. At left is a section of the Scintillation Counter. For a sense of scale, there is a puny human on the far right.

4.2 Inner Calorimeter

For certain exclusive analyses the detection of neutral particles is of particular importance. Although the analysis described herein did not make use of the IC, it does affect the acceptance of electrons, so it will be discussed briefly.

The standard configuration of CLAS detects neutral particles only down to 10° . To increase acceptance from 5° to 16° , the IC was designed and incorporated into CLAS. It is inserted between the target and the drift chambers as shown in Fig. 4.6. The IC is composed of 424 Lead Tungstate crystals, which are tapered and 16 cm long, which have avalanche photodiodes attached at the rear. The photodiodes are connected to preamplifiers, which interface with the data acquisitions system via ADC's and TDC's [14].

Due to the mass of the IC, electrons which hit it are no longer available for inclusive analysis. Therefore, the acceptance below approximately 17° in polar angle is effectively zero for this analysis.

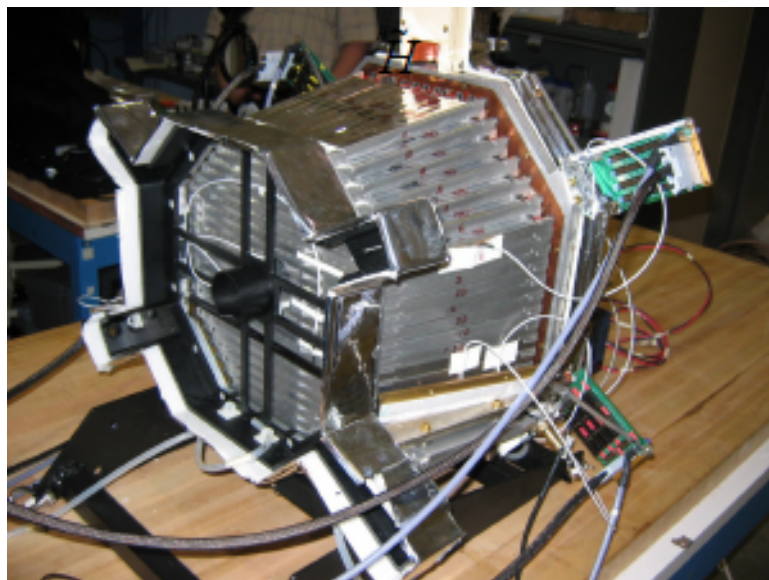


Figure 4.5: A photograph of the Inner Calorimeter surrounded by its electronics. The IC fits between CLAS and the polarized target and is approximately a meter in diameter; the central hole allows the beam to go through [15]

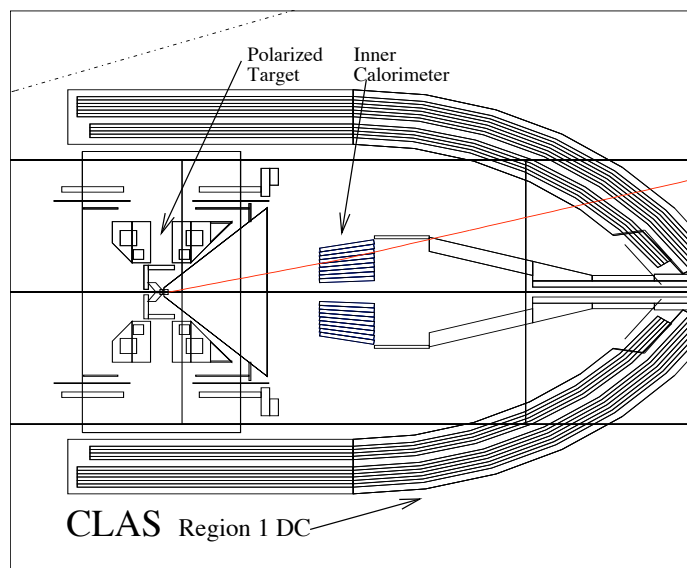


Figure 4.6: A schematic drawing of the polarized target, the IC, and region 1 of the drift chambers. For scale, the polarized target is approximately a meter in width. The red line depicts a the path which a particle originating in the target might take [15]

4.3 Drift Chambers

The drift chambers are used to track charged particles. This precise position measurement allows the momentum of the particle to be determined by measuring the curvature of the track. The premise of detection in the drift chambers is as follows: a number of wires are maintained at high potential inside a gas-filled chamber. When a charged particle passes through the gas in the DC, an 88% to 12% mixture of Argon and CO_2 , it ionizes gas molecules. These ions then drift towards the wires and the resulting currents are measured to determine where the particle traveled. An example track is shown in Fig. 4.8.

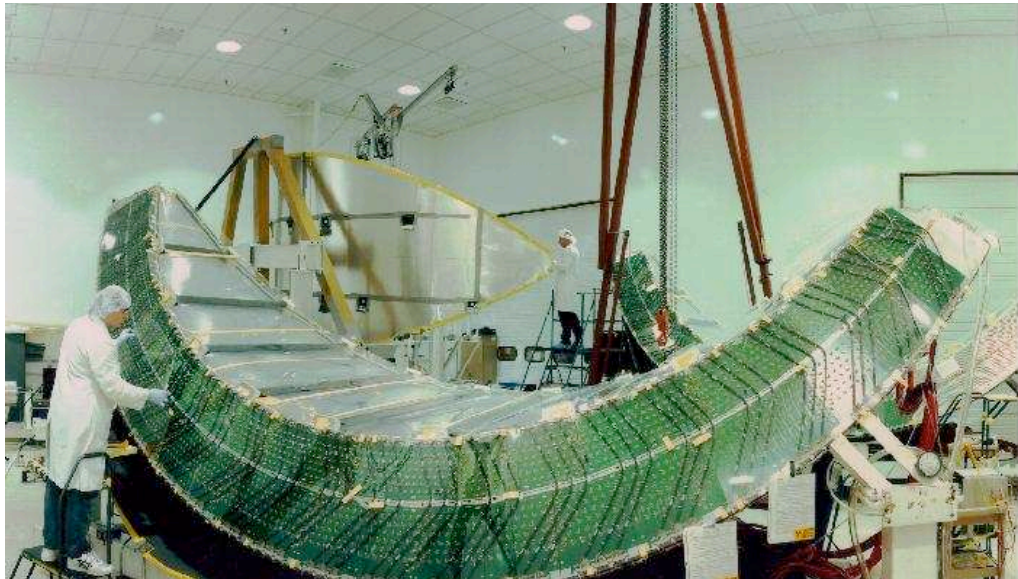


Figure 4.7: A photograph of a section of the drift chambers as they are being prepared for installation.

Each sector of CLAS is essentially an independent detector. The drift chambers in each sector stretch from one torus coil to another, which gives the end plates a 60° tilt with respect to each other. Wires are stretched from one endplate to the other such that they are perpendicular to the beam line. The drift chambers are composed of 3 regions, which each contain 2 super-layers; super-layers in region 1, closest to the

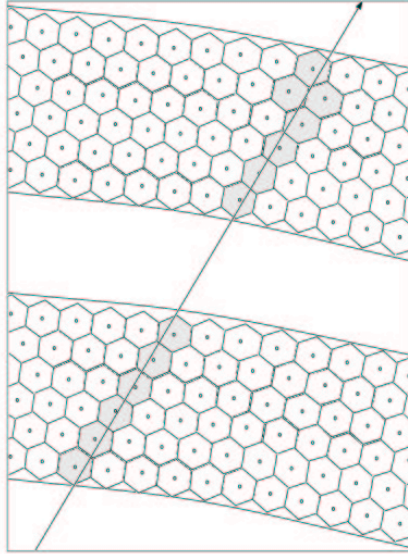


Figure 4.8: An example of a charged particle passing through the drift chambers. The particle path is depicted by the arrow, and the cells activated by the particle are shaded. Fig from Ref. [15]

beam line, have first 6 and then 4 layers due to space constraints, while super-layers in regions 2 and 3 each have 6 layers [13].

One “cell” of wires is made up of one “sense” wire that is maintained at a high positive potential and 6 “field” wires that have a negative potential of half the magnitude of the sense wire. The magnitudes are set in this way so that the net potential of the drift chambers is 0 and does not interfere with other components of CLAS. The super-layers of wires are set at alternating angles, to allow for positioning in the azimuthal direction; one super-layer is oriented azimuthally to the beam line, while the next is tilted 6° to that.

The signal from each of the 35,148 sense wires [13] is sent to a pre-amplifier, from where bundles of 16 are sent to a post-amplifier and discriminator which turns them into digital pulses. These pulses are then used for a time-to-digital converter (TDC). Despite the large size and complexity, the DC works quite well. The fractional

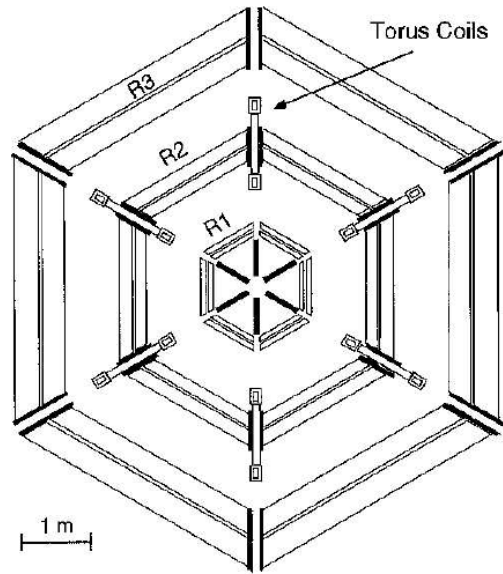


Figure 4.9: A cross-sectional view of the drift chambers. The torus magnet position is indicated.

momentum resolution ranges from $\frac{1}{2}\%$ to 1% due to non-uniform dispersion. The polar angle resolution is approximately 1 mrad, while the resolution on the azimuthal angle is approximately 4 mrad [13].

4.4 Cherenkov Counter

The Cherenkov counter (CC) relies on the eponymous radiation to discriminate electrons from pions. Cherenkov radiation is the radiation given off by a charged particle which is moving faster through a material than the speed of light in that material. Due to the difference in masses of electrons and pions, there is a large difference in the threshold for cherenkov production between the two: the threshold for electrons is 9 MeV/c while that for pions is 2.5 GeV/c [13]. This threshold depends on the gas which the particles pass through. In CLAS, the gas is C_4F_{10} with an index of refraction of 1.00153 [13]; this gas is recirculated and maintained at a constant pressure.

To maximize the acceptance, the CC was designed to have the photomultipliers positioned in the “shadow” of the torus coils. Elliptic and hyperbolic mirrors, as shown in Fig. 4.11, direct the emitted light towards the photomultipliers (PMT). Each PMT sits at the base of a “Winston” cone, which further focuses the light on to the PMT. The CC in each section is divided into 18 segments which provide coverage up to 45° and allow for some information about the polar angle of impinging particles to be preserved.

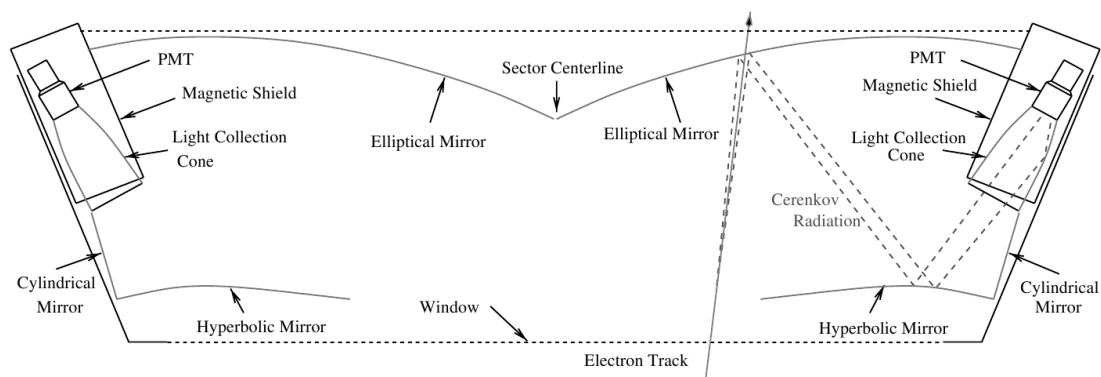


Figure 4.10: A schematic overview of one section of the CC. An electron track is shown passing through the CC, while the resulting Cherenkov radiation is reflected into the photomultiplier. [13]

Optical Mirror System

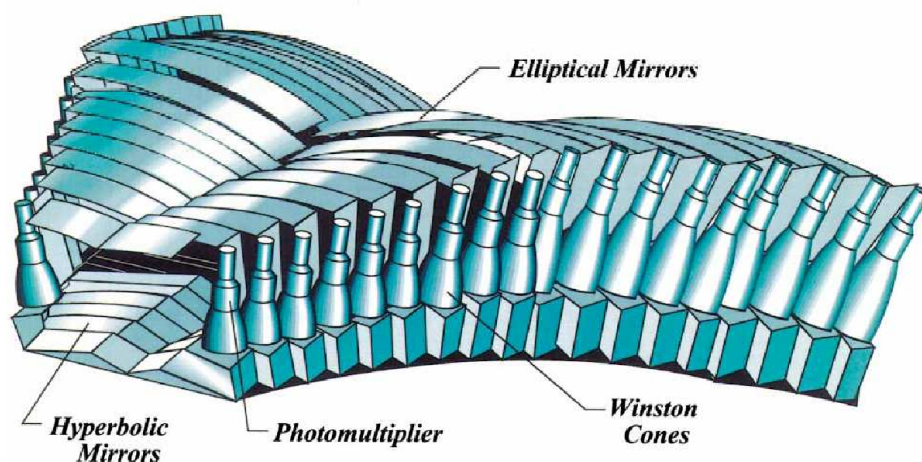


Figure 4.11: An illustration of the mirror system and photomultipliers for the CC. All 18 segments for one sector are shown. Each sector Has hyperbolic and parabolic mirrors to focus light towards the edges, where a “Winston” cone funnels it into a photomultiplier tube. [16]

4.5 Scintillator Counter

The Scintillator Counter (SC) or Time of Flight (TOF) counters enable measurement of the time of flight of a particle. When an electron hit is detected in the SC the time is calculated based on the measured path of the electron in the DC and the RF signal from the accelerator. Since all electrons detected are traveling sufficiently fast that they can be considered to be moving at the speed of light, it is a simple matter to find the moment at which the interaction producing them must have occurred. This interaction time can then be used, along with the DC track length, to find the time of flight for each other detected particle in an event.

The SC covers from 8° to 142° in polar angle. The scintillator strips are all 5.08 cm [13] thick, although their width varies with angular position so that they occupy approximately 1.5° . Each strip is instrumented with 2 photomultipliers, which are positioned in the shadow of the torus coils so as to not affect the acceptance.

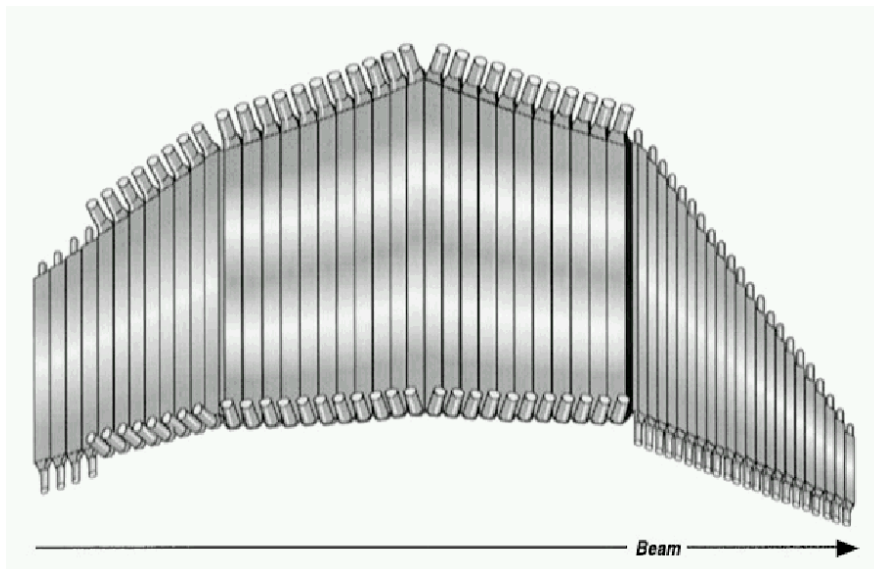


Figure 4.12: An illustration depicting the orientation of scintillator strips for one sector of the SC. Beam direction is shown for reference [15]

4.6 Electromagnetic Calorimeter

The function of the Electromagnetic Calorimeter (EC) is to detect electrons with energy higher than 0.5 GeV, photons with energy higher than 0.2 GeV, and neutrons [13]. The “forward” part of the EC covers up to 45° , while the “large-angle” section covers from 45° to 75° but only for two sectors. The EC is composed of alternating strips of scintillator and lead. The scintillator allows for detection, while the lead provides a dense material for particles to interact with. It is a sampling calorimeter, which means it does not detect all of the energy of the incident particle. The ratio of incident particle energy to the energy deposited in the scintillators is called the “sampling fraction” and depends on the radiation length of the calorimeter and the ratio of scintillator to lead. For the EC, the sampling fraction is about 0.3.

Electrons, when impinging on a material, will typically produce positron-electron pairs, which can also produce more positron-electron pairs if energetic enough. In this way, an electron will create a “shower” of particles proportional to its energy when it hits the EC. In contrast, hadrons such as pions are “minimum ionizing particles” and in general only interact by directly ionizing atoms. This means they leave a signal that is independent of their energy. In this way it is possible to discriminate between particles.

The EC in each sector is an equilateral triangle. It is composed of 39 alternating layers of lead and scintillator. Lead layers are cut from lead sheets 2.2 mm thick and scintillator layers are made from 36 strips of 10 mm thick scintillator. Each scintillator layer is oriented at 120° with respect to the previous layer to allow for location information to be determined. Light from the scintillators is directed to photomultipliers via waveguides along the edges of the EC sections.

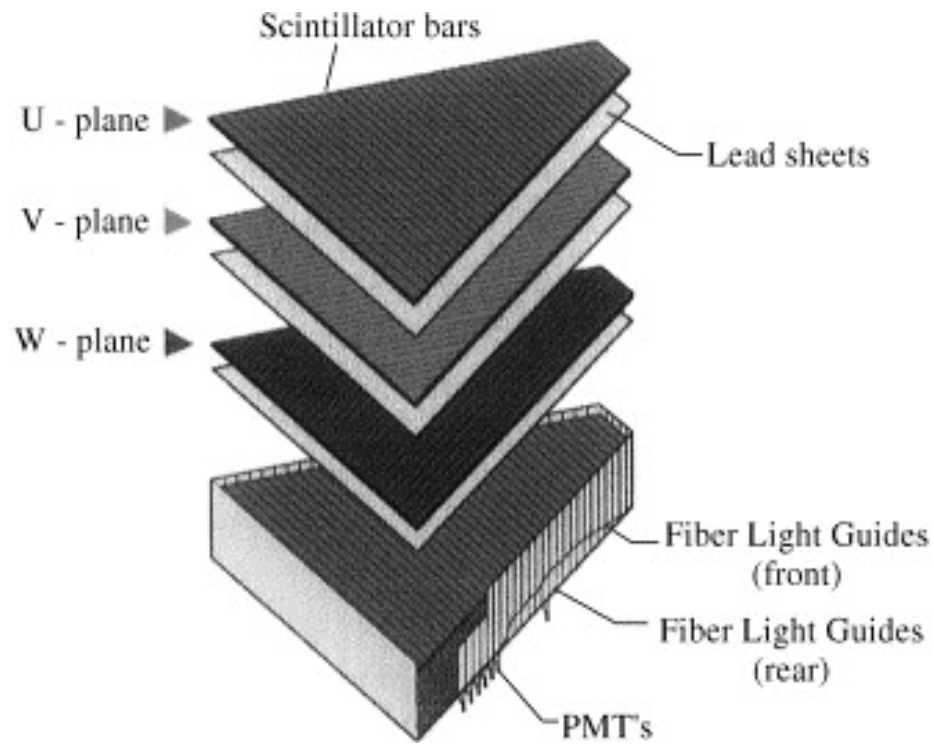


Figure 4.13: A diagram of a section of the EC. Alternating layers of lead and scintillator are depicted, and the separate orientations of each layer of scintillator strips are shown, labeled as U, V, and W planes. Light guides collect light from the scintillator strips and direct it to PMT's mounted in the rear. [17].

4.7 Trigger and Data Acquisition

All of the various detectors previously discussed generate a large amount of data. The amount of data generated is far larger than it would be possible to collect. To select only useful events, there is a two level trigger system. The first level operates within 90.5 nanoseconds according to definitions set by each experiment [15]. Events which pass the first trigger are sent to the second, which finds tracks in the DC. Events which pass the first trigger and have a plausible track are sent to be recorded.

Data acquisition occurs in three processes, the Event Builder (EB), Event Transport (ET), and Event Recorder (ER) [13]. The EB assembles the data from all the detectors and from the separate sets of detector electronics into a complete event, adds a run number, an event number, and event types, and then passes the event on to the ET. The ET manages the event on shared memory to allow for online reconstruction, analysis, and monitoring [13] and passes the event to the ER. The ER writes events to a local RAID array and also to the remote tape silo. Events are organized into files and runs, with each run consisting of up to 100 files or about 3 hours of data. Since the tape silo records slowly, consecutive files are not guaranteed to be on the same tape.

Chapter 5

Polarized Target

In addition to a beam line and a detector, a target is also required to do scattering experiments on the nuclei of atoms. In general, a target consists of a sample of a material that contains the nuclei of interest. For investigating the structure of nucleons the smallest atoms are best, since there are fewer effects from the nuclear environment. In these cases, hydrogen is often used, generally as a liquid due to the increased density and therefore increased event rate. The hydrogen atom, while being simple, contains no neutrons so experiments intending to investigate the neutron generally involve deuterium due to the instability of (and difficulty of producing) the free neutron. There are also experiments where the goal is to investigate the structure of the nuclei as a whole. To serve that purpose, atoms with larger atomic number are used, such as elemental copper or gold.

While these targets are all useful, the desire to measure the spin properties of nucleons require polarized targets, and consequently different materials. While there are multiple techniques for polarizing a target material, only one, Dynamic Nuclear Polarization, was used. The materials used for the experiment described in this dissertation were ammonia, NH_3 , and deuterated ammonia, ND_3 . Other polarized

targets, which can use different schemes for polarization, such as the “brute force” approach, include Lithium Hydride/Deuteride and Hydrogen Deuteride.

5.1 Dynamic Nuclear Polarization

The Dynamic Nuclear Polarization (DNP) technique is the name for the process we use to orient the spins of the nuclei of the target material in a specific direction. The technique exploits different physical effects, those described by the Solid State Effect and those described by Equal Spin Temperature Theory. Both of these effects can be applied to spin $\frac{1}{2}$ or spin 1 systems, but the simplicity of the spin $\frac{1}{2}$ system offers a better opportunity to explain the process. Following the explanation for spin $\frac{1}{2}$, an explanation of the differences for spin 1 nuclei will be provided.

In a material with no external magnetic field, the nuclei will be randomly oriented, producing no net polarization. To break the symmetry a magnetic field is applied which separates the states into those parallel to the magnetic field and those anti-parallel, with differing energies. The polarization is then defined by:

$$A = \frac{N^\uparrow - N^\downarrow}{N^\uparrow + N^\downarrow} \quad (5.1)$$

where $N^{\uparrow(\downarrow)}$ is the number of nuclei parallel or anti-parallel to the magnetic field, respectively. The ratio of the population of these two states is given by the Boltzmann distribution:

$$\frac{n^\uparrow}{n^\downarrow} = e^{\frac{-\mu B}{k_B T}} \quad (5.2)$$

so using Eq. 5.1 and Eq. 5.2 the polarization is:

$$P = \tanh \frac{\mu B}{k_B T} \quad (5.3)$$

The only free parameters in this equation are the magnetic field, B , and the temperature, T . To increase the polarization, B must be increased and T decreased. The temperature and magnetic field used in our apparatus is 1 Kelvin and 5 Tesla, these being relatively achievable values for a laboratory setting. Even so, the polarization for protons in this condition is approximately 0.5%. Electrons, however, due to their much larger magnetic moment of 9×10^{-24} J/T, obtain polarizations of about 99.7%. Of course, most electrons in an atom form pairs that are spin anti-aligned; the polarization given is only for unpaired electrons, also known as “free radicals” or “paramagnetic centers.” These centers must be added to the material either chemically or through irradiation so that it may be polarized. Once enough free-radicals are distributed in the material and polarized, their polarization must be transferred to the nuclei. The DNP process uses microwaves of a particular frequency to accomplish this feat. The exact mechanism by which this occurs depends on the density of radicals; the two dominant processes are discussed next.

5.1.1 Solid State Effect

The Solid State Effect (SSE) is conceptually clearer and gives a reasonable understanding of the physics behind DNP. For materials where the density of radicals is low enough so that they can be considered non-interacting, the SSE provides an excellent description of the actual process at work. Unfortunately, materials which are doped with radicals by irradiation don’t fall into this category. Nonetheless, due to the explanatory power of the theory, the SSE will begin the discussion.

The application of a magnetic field lifts the degeneracy of the spin states for elec-

trons and protons and creates what is called the “Zeeman” splitting. The magnitude of the splitting is proportional to the magnetic moment, so the electron splitting is approximately three orders of magnitude larger than the proton splitting. The appropriate frequencies for driving these transitions with a 5 Tesla magnetic field are about 140 GHz and 213 MHz, respectively. Applying radiation at the frequency to drive one of these transitions will not result in net polarization since the up-to-down transition is driven with the same probability as the down-to-up transition. To achieve polarization, a transition in which both spins are flipped is used. For positive polarization, this is the electron transition, ν_e , plus the proton transition, ν_p . After flipping both spins, the electron quickly flips back, due to its strong coupling with the lattice. The proton however, does not couple as strongly, and has a characteristic relaxation time of roughly half an hour at our operating temperature [18]. The same process works for the alternate spin-pairing: $\nu_e - \nu_p$. This transition will lead to negative polarization though. This is, in fact, particularly convenient, since the polarization can be reversed without changing the direction of the magnetic field. Fig. 5.1 provides a schematic depiction of the process.

Polarization in this manner occurs solely through protons which are located close enough to a free radical to be electromagnetically coupled. Once polarized though, a proton can be involved in an isoenergetic transition where it exchanges spins with another proton. It is then free to be polarized again. In this way, called “spin diffusion”, polarization is distributed throughout the material.

5.1.2 Equal Spin Temperature Theory

For materials where the electron density is high enough that the spin-spin interaction can’t be neglected, the SSE does not provide the best answer. In that case, a more

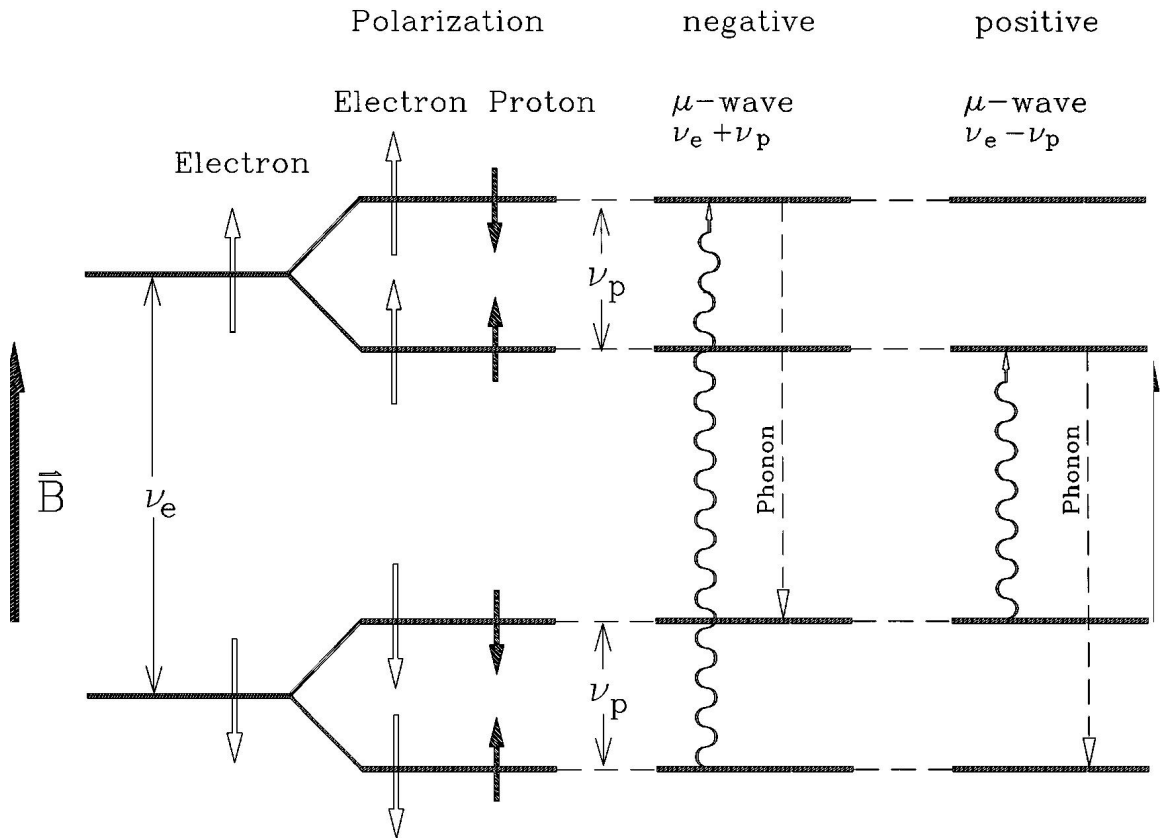


Figure 5.1: A schematic illustration of the process used to polarize the hydrogen nuclei of ammonia. Open arrows represent the electron, while closed arrows represent the proton. ν_e is the electron Zeeman splitting, and ν_p is the proton splitting. Photon lines demonstrate which transitions are driven by the polarizing microwaves, while dashed lines show transitions that are driven by phonon interaction with the lattice. Figure from Ref. [18].

complete picture results from the Equal Spin Temperature Theory (EST). For example, the SSE would suggest that the optimum polarization frequency is constant, however when polarizing ammonia, the frequency which gives the highest polarization changes substantially with the value of the overall polarization. This optimum frequency also changes over time as the material acquires more dose.

The spin-spin interaction causes the normally discrete states to spread into a continuum, where the population of the states is determined by Boltzmann distributions.

There are two “temperatures” to describe the system: T_{SS} , which determines the distribution for the spin-spin distribution, and T_{ZE} which determines the distribution for the Zeeman splitting. Fig. 5.2 shows these distributions and the varying effects that different temperatures can have on them.

The microwaves applied in the DNP process will shift an electron from one “Zeeman” band to the other, but they also will change the temperature of the spin-spin reservoir. It is thermal contact between this reservoir and the proton “Zeeman” reservoir that causes the protons to polarize. Since the microwaves are constantly putting in energy to the electron’s reservoirs, any energy that is transferred to the proton reservoirs is replaced. The net result is an increase in the net polarization of the protons. One interesting prediction of EST is that any spin system in thermal contact with the electron reservoir will also become polarized. In ammonia, this means that the nitrogen atom at the core of the ammonia molecule should also be polarized, depending only on the magnetic moment, μ , of the nucleus: $\tanh(\frac{\mu B}{kT_s})$ where T_s is the temperature of the spin reservoir. This can be measured, [19], and was found to be in agreement with EST.

5.1.3 Spin 1

The discussion so far has been entirely for the case of spin $\frac{1}{2}$ nucleons. This is useful for proton targets, like ammonia, but does not entirely apply for deuterated ammonia, which was the target material used for this experiment. A deuteron is a spin 1 nucleus, and as such the DNP process is slightly more complicated, though the preceding discussion should provide the basics.

In an applied magnetic field, the spin 1 nuclei forms a triplet with the following three states: $|\uparrow\uparrow\rangle$, $|\downarrow\downarrow\rangle$, and $|\uparrow\downarrow\rangle + |\downarrow\uparrow\rangle$. Henceforth, these states will be referred

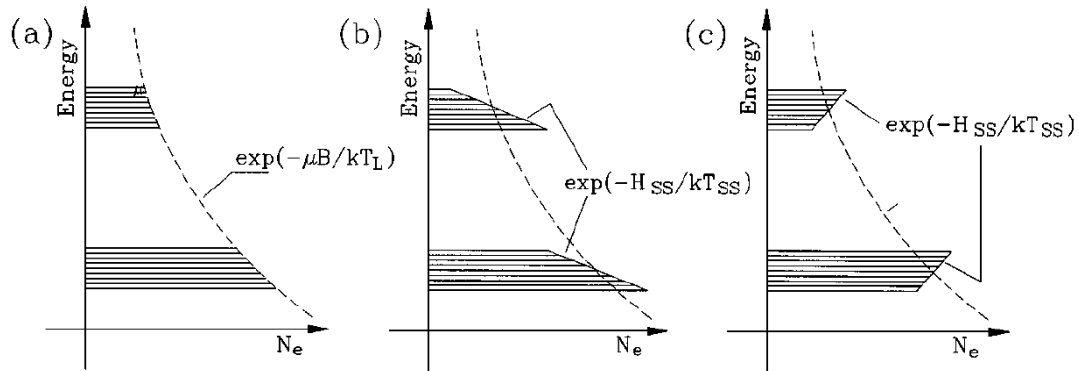


Figure 5.2: This diagram shows population densities of the electron levels for the spin-spin interaction and Zeeman reservoirs. (a) The spin-spin interaction reservoir and Zeeman reservoir are in thermal equilibrium with the lattice, (b) Both reservoirs have temperature greater than zero, with the Zeeman reservoir higher, (c) The spin-spin reservoir is at negative temperature, but with smaller magnitude than the positive temperature of the Zeeman reservoir. Figure from Ref. [18].

to by their z-component: 1, -1, and 0, respectively. Polarization is not as obviously defined as for spin $\frac{1}{2}$; the definition is:

$$P = \frac{N_1 - N_{-1}}{N_1 + N_{-1} + N_0} \quad (5.4)$$

Eq. 5.4 is also called the “vector polarization”, to be compared with the “tensor polarization” [20]. The vector polarization is measured by standard NMR techniques, and only the vector polarization is considered for this research, so it will be referred to simply as polarization for the duration of this dissertation.

The electron still has two states, of course, so the same ideas from earlier apply, but now the electron is coupling to the three deuteron states. Since the 1 and -1 states are shifted away from the 0 state by an equal amount, the -1 to 0 and 0 to 1 transitions are stimulated by the same frequency of microwaves. Obviously then, the final polarization will not be as high as for spin $\frac{1}{2}$ nuclei, since some nuclei will remain

in the 0 state.

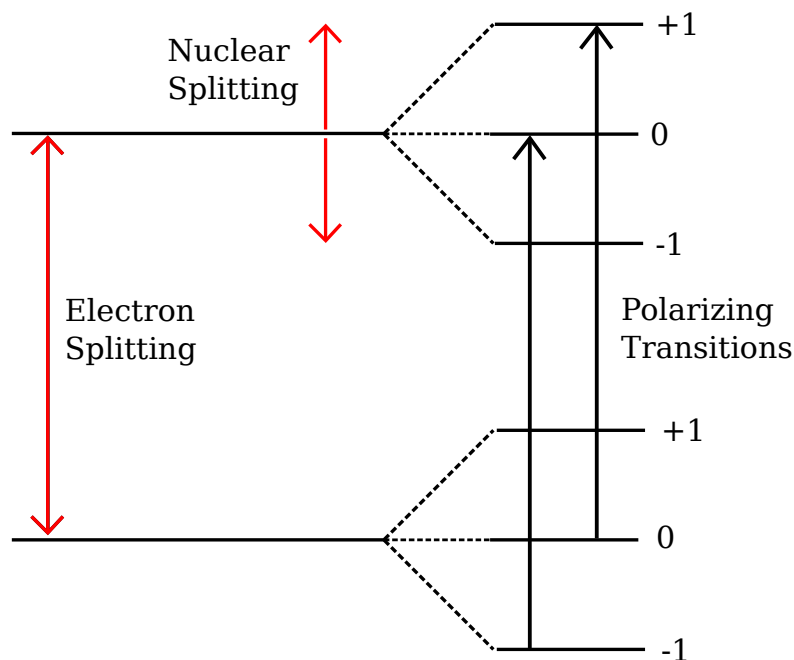


Figure 5.3: The DNP process as it applies to the deuteron. The separation between the 0 and 1 states is the same as that between the -1 and 0 states, so both of these transitions are driven by the polarizing microwaves.

In general, the three states of the deuteron are split equally as described above. In this case, the -1 to 0 and 0 to 1 transition are exactly the same and the NMR signal looks the same as it would for a spin- $\frac{1}{2}$ system. This is true for molecules where the deuteron sees external potentials with Cartesian or spherical symmetry. Due to the cubic nature of LiD crystals, this is exactly what happens in that material. In ammonia, however, there is an electric field gradient in the direction of the Nitrogen-Deuterium bond. This gradient interacts with the quadrupole moment of the deuteron to shift the +1 and -1 states down in energy relative to the 0 state, thus decreasing the energy of the 0 to 1 transition and increasing the energy of the -1 to 0 transition. This is reflected by shifts in the NMR spectrum of the deuteron.

5.1.4 Polarization Measurement

The polarization of this target is determined using an NMR set-up which measures the magnetic susceptibility of the target material, in our case deuterated ammonia. The output of the NMR system is a curve which represents the emitted or absorbed (depending on positive or negative polarization) power from the target as a function of the NMR frequency. The area under this curve is proportional to the polarization of the target. The constant of proportionality must be well known and, in addition, varies over the course of an experiment. In order to find the polarization, a method for determining this constant, known as the “calibration constant”, is necessary. By allowing the target to come to thermal equilibrium in the magnetic field used for polarizing, the target can acquire a polarization that is determined by statistical mechanics. This method, known as “taking a TE”, can be used for both proton and deuteron targets, although the deuteron TE signal is much smaller and harder to extract from the background noise.

The TE calibration process involves multiple steps. To accurately determine the area of the deuteron signal, the background must be removed. This is done by subtracting a “baseline” scan, where a scan consists of measuring the output of the NMR system over a spread of frequency. Each scan is averaged from a number of sweeps, where each sweep is a measurement spanning the lowest frequency to the highest and back. The baseline is done by decreasing or increasing the magnetic field until the deuteron signal is no longer in the range of frequencies which are being swept over. Then a scan is taken using a large number of sweeps, up to 5000 in some cases. When the magnet is returned to the resonant field, subtracting the baseline will remove effects from the electronics. Some background will still effect the measurement so this is subtracted with a quadratic fitting to the non-signal portions of the scan.

Then, to create a calibration constant which relates the area of the deuteron signal to the polarization, a measurement must be made at known polarization. At thermal equilibrium, the polarization of the deuteron is given by Eq. 5.5

$$P_D = \frac{4 \tanh \frac{\mu B}{2k_b T}}{3 + \tanh^2 \frac{\mu B}{2k_b T}}. \quad (5.5)$$

The sample must be allowed to relax to thermal equilibrium, which can take up to an hour for deuterated ammonia. As seen in Eq. 5.5, the temperature must also be known. Once the sample is at thermal equilibrium the polarization is known, so a series of scans are done to determine the area of the signal. The calibration constant is calculated by dividing the measured polarization by the measured area. After the target is polarized, this constant can be multiplied by the area of the enhanced signal to give the enhanced polarization.

It is possible to determine the deuteron polarization by an alternative method. Due to the dual nature of the deuteron transitions, the NMR signal looks substantially different from that of a proton. The proton signal is basically Gaussian, while the deuteron signal more closely resembles Batman. Fig. 5.4 shows examples of the proton and deuteron NMR signals, both polarization-enhanced and at thermal equilibrium. As the polarization of the deuteron grows, the signal becomes increasingly asymmetric. As can be seen in Fig. 5.5, the two transitions contribute unequally as their populations change. This enables the polarization to be determined not just by the area of the signal, but also by the line shape. A fitting program was developed [21] that can extract the polarization by fitting a line to the data. An example of the fit that is achieved is seen in Fig. 5.6. A discussion of the polarization calibration method used in this analysis can be found in Section 8.3.

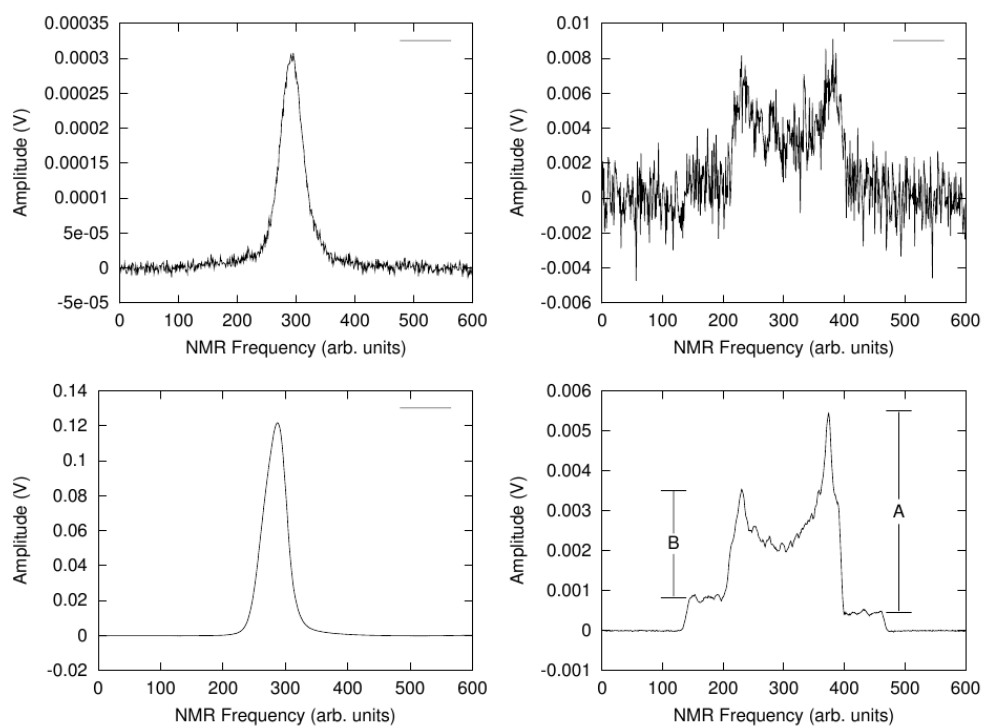


Figure 5.4: Example NMR scans for proton (left) and deuteron (right). The top graphs are thermal equilibrium signals, while the bottom graphs are taken from highly polarized samples. The smaller signal-to-noise ratio of the TE signals is evident. Figure from Ref. [22].

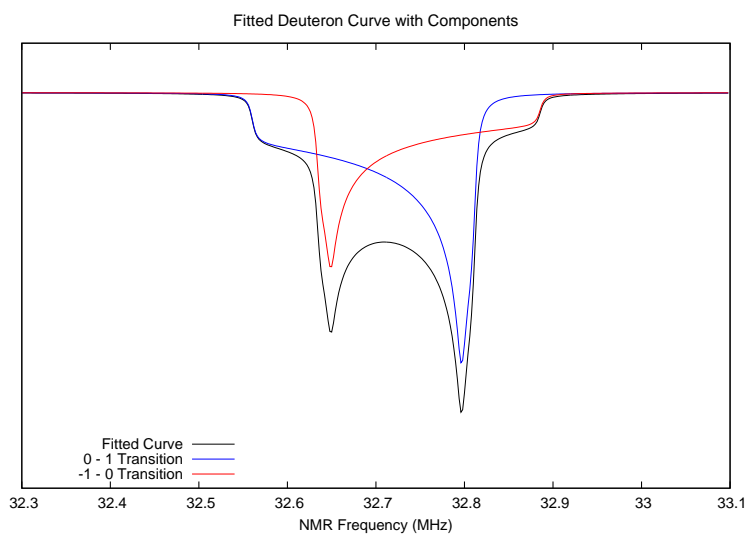


Figure 5.5: The nature of the deuteron signal is clearly shown when decomposed into its two superpositional components. The black curve shown here is a fit to actual data (see Fig. 5.6) and the red and blue curves are the separate transition curves derived from the fit.

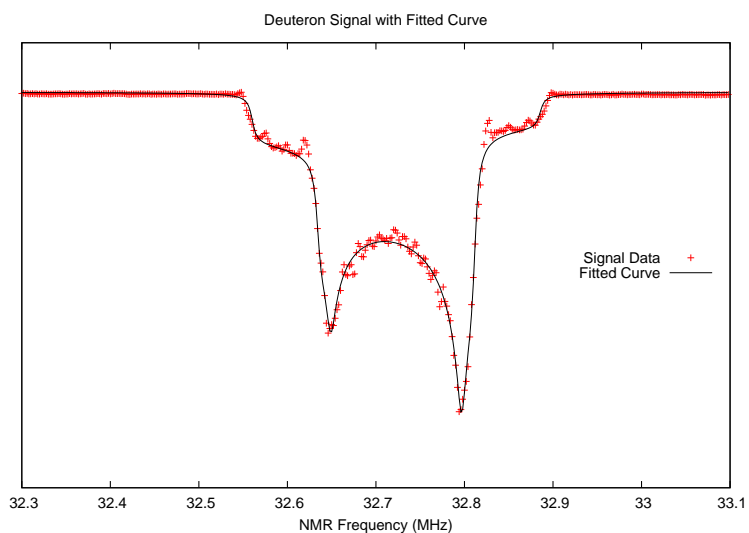


Figure 5.6: Shown is an NMR scan for an enhanced deuteron signal with the resulting fit line. Agreement is quite good.

5.2 Target Apparatus

To create a functioning polarized target requires a substantial apparatus: a superconducting magnet, with associated power and liquid helium supply, is required to provide the magnetic field, a refrigerator and pumps are needed to provide the requisite temperature, a microwave source which can be adjusted to optimize polarization, an NMR setup to measure the polarization, a system for inserting and removing the target, along with all the various devices to measure temperatures, pressures, and flow rates. The Polarized Target lab at the University of Virginia is equipped to polarize and record a number of materials, and contains all the appropriate equipment. Each component of the system will be discussed, first describing the lab apparatus, and then differences between it and the system used in Hall B at Jefferson Lab for actual measurements will be highlighted.

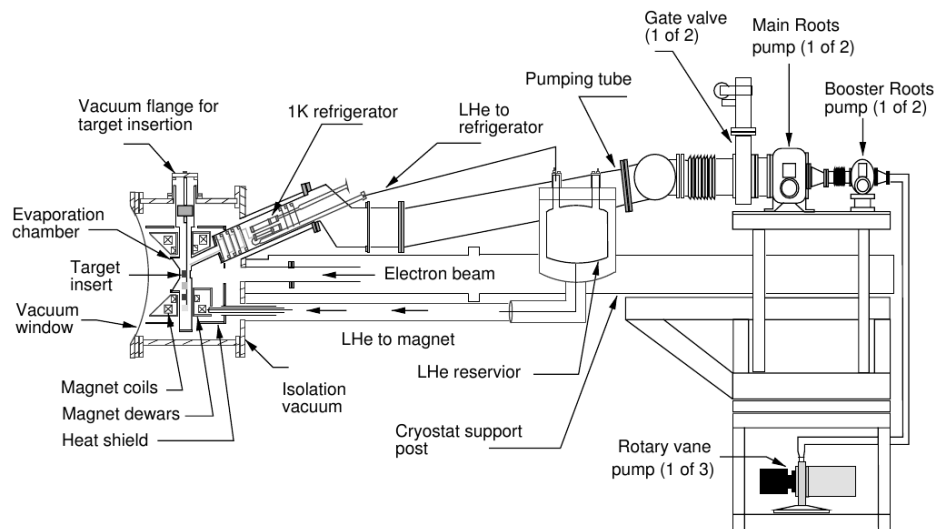


Figure 5.7: A detailed schematic view of the target apparatus, as used in Hall B, showing all the vital components for the target polarization system. Figure from Ref. [22].

Magnet The standard magnetic field used in tests in the lab is 5 Tesla. To provide this magnitude of magnetic field, a superconducting magnet is used. To remain superconducting, the magnet coils must be kept at liquid Helium (LHe) temperatures. The cryostat contains a large LHe reservoir which maintains the magnet temperature and is also used to supply the refrigerator with Helium. There also exists a jacket of liquid Nitrogen (LN_2) in the cryostat which helps to shield the helium reservoir from the ambient temperature. Since the space around the cryostats is evacuated, the main mode of heat transfer is radiative. The LN_2 jacket absorbs the radiative transfer from the room temperature outer can and radiates a much smaller load to the LHe reservoir.

Besides the high field, it is also a requirement that the magnetic field be highly uniform. The uniformity is important for the NMR system to return good measurements, and also for the DNP process itself to work. Since NMR and DNP both rely on stimulating specific transitions, the magnetic field must be the same in all parts of the sample for the energy levels of the transition to have the correct spacing. The uniformity must be at the 10^{-4} level or better [10]. To achieve this, the magnet is shaped like a solenoid (in the lab) or a Helmholtz pair (at JLab).

The main difference between the lab magnet and the magnet used at JLab is that the beam must pass through the target, and the target polarization must be aligned longitudinally with the beam. To accomplish this, a different magnet configuration must be used, since the coils of a solenoid would be in the way. Therefore, a Helmholtz configuration is used, which consists of a pair of coils oriented co-axially with the beam to allow the beam to pass through. It is also important that the coils block as few of the scattered particles as possible. The magnet can be seen in cross section in Fig. 5.8.

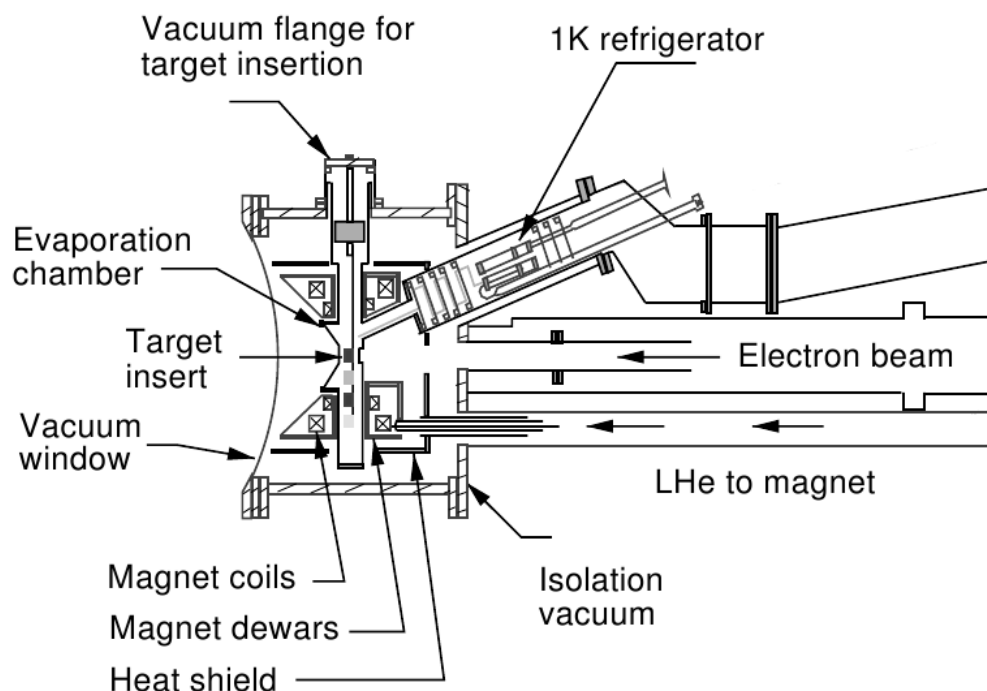


Figure 5.8: A detailed schematic view of the target apparatus, as used in Hall B, showing all the vital components for the target polarization system. In Hall B, the refrigerator enters at an angle, although the target stick is still positioned vertically. Figure from Ref. [22].

Refrigerator The refrigerator is what provides the low temperatures which allow the DNP process to work. It is a Helium evaporation refrigerator, which relies on evaporation to cool below the temperature of LHe at standard pressure. LHe is pumped into the “separator”, which is a small container about halfway down the refrigerator, from a LHe dewar. In the lab setup, the magnet reservoir also serves as this LHe supply. There, Helium gas is separated from the LHe by a porous plate, so that a consistent flow of LHe can be provided to the nose. The porous plate allows LHe to move through it, via gravity, to the lower half of the separator, and gas is

pumped out of the top by the separator pump, a compressor.

Two valves allow helium to flow from the separator to the “nose” of the refrigerator, where the target is. One is the “run” valve, and the other is the “bypass” valve. The main difference is that the run valve leads to the nose via a circuitous route through a tube and plate heat exchanger, which allows the cold helium gas that is being pumped out of the nose to pre-cool the LHe before it gets to the nose. Once the nose is full of helium, the temperature must be reduced from 2 K to 1 K. To accomplish this feat involves using a very large set of pumps to reduce the pressure in the nose. Similar to evaporation, higher energy Helium atoms leave the liquid in the nose, carrying away energy as they go, thus reducing the temperature. The large volume of gas that must be pumped away necessitates a large pair of Roots blowers, another smaller Roots, and several roughing pumps to back them.

The Hall B target setup has one main constraint that causes it to differ from the lab setup: it must fit into CLAS. To do this, a so-called “horizontal” fridge was designed. As seen in Fig’s. 5.7 and 5.10, the refrigerator comes in to the rest of the target at an angle. Additionally, due to the radiation environment of the hall, the run and bypass valves must be remotely controlled.

Microwaves The microwaves required for DNP at 5 T are 140 GHz with a power on the order of a few watts. The microwaves are transmitted through a couple meters of waveguide, so to deliver enough power to the target a microwave source of substantial power must be used. The source is an extended interaction oscillator (EIO) vacuum tube. Discussion of the workings of this tube is beyond the scope of this dissertation. The microwave frequency must also be tunable over approximately 1 GHz. A motorized mechanical adjustment provides this capability.

The microwave system used at JLab is fundamentally the same as the one used

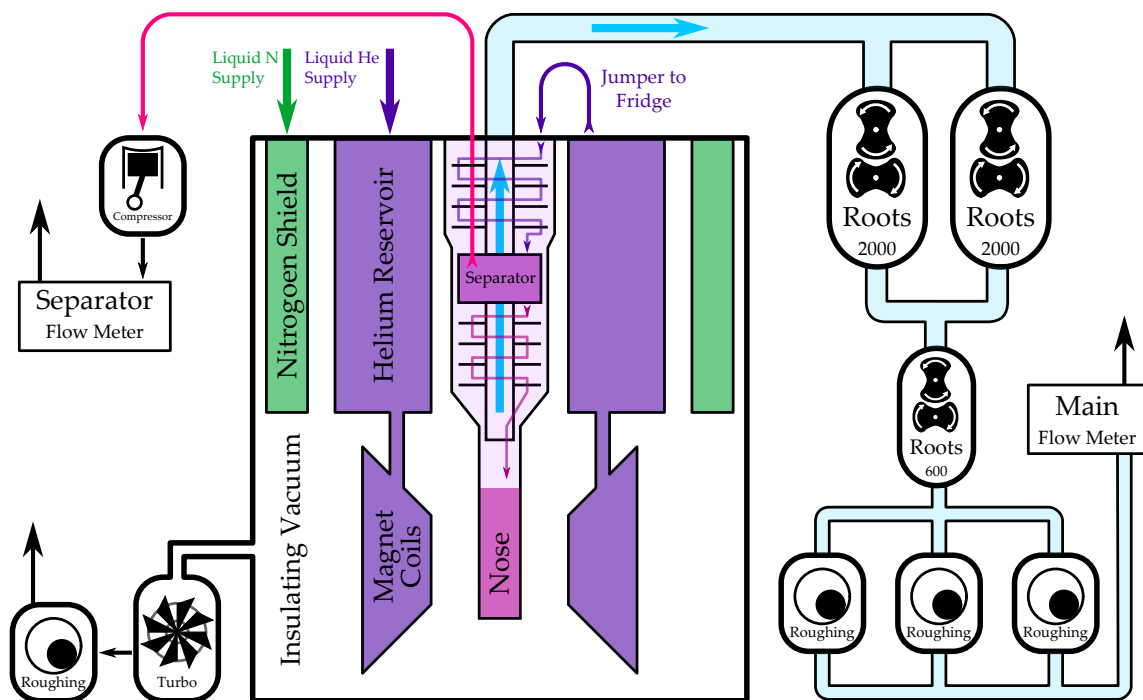


Figure 5.9: The drawing depicts the main mechanical components to the polarized target system. The magnet and cryostat are the large central box, and the assorted vacuum pumps are arrayed around it. The refrigerator is in the center, while the target material itself is inserted into the nose. Drawing courtesy of J. Maxwell [12].

in the test lab. The only difference is the amount and positioning of the waveguide to accommodate the unique configuration in Hall B.

NMR The NMR system is vital to the proper operation of the polarized target. First, it provides a measure of the polarization state of the target, which is an important attribute for analysis. Second, it allows for the optimization of the polarizing microwave frequency. Because this frequency changes with the polarization of the target as well as with the amount of dose the target material has received, it is a necessity to have some form of feedback.

The polarization of ammonia is a very weak signal and poses some problems for detection. The method of NMR is particularly suited to detecting small signals. The

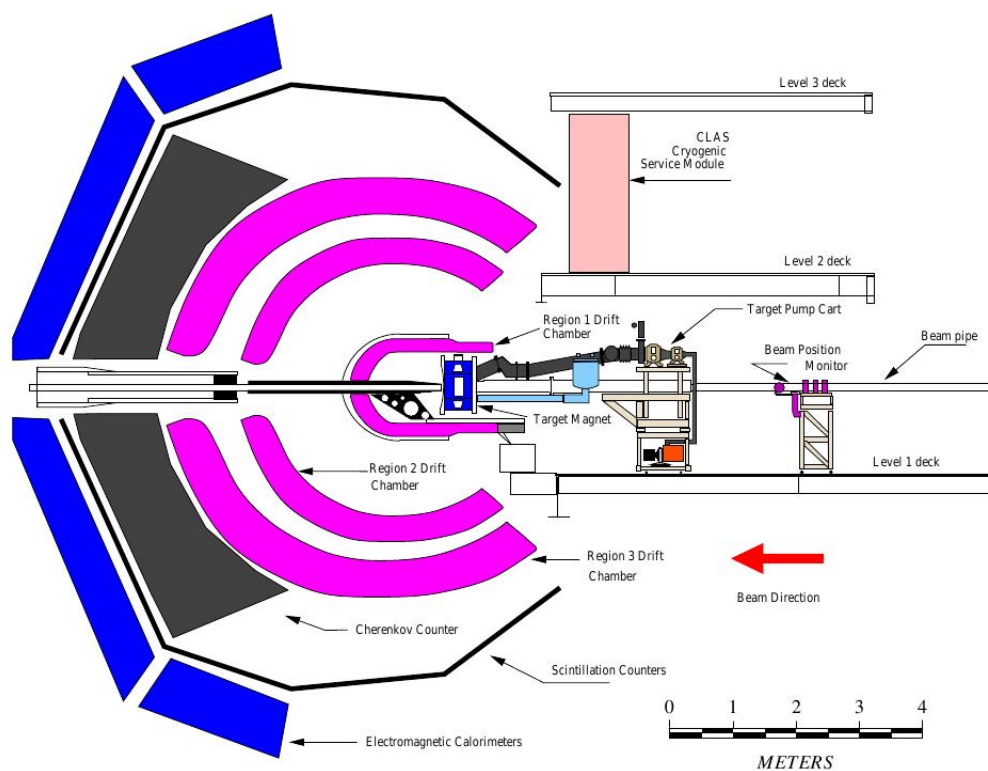


Figure 5.10: The polarized target apparatus, shown as it would be oriented in CLAS. The polarizing magnet and material are located near the center of CLAS, while the pumps and related gas handling setup extend in the direction of the beam line. [23]

NMR process involves sweeping an RF signal over a 800 kHz band centered on the frequency of the transition between the nucleus's spin states (213 MHz for protons, 32.7 GHz for deuterons) known as the "Larmor frequency". The detection of the signal is done with a piece of equipment known as a "Liverpool Q-meter." Fig. 5.11 gives a schematic representation of the Q-meter's workings; see also Ref. [24].

The ammonia target material is placed in a coil which forms the inductive part of a series RLC circuit. The inductance of the coil depends on the magnetic susceptibility of the material within it; the frequency dependent magnetic susceptibility can be described thusly:

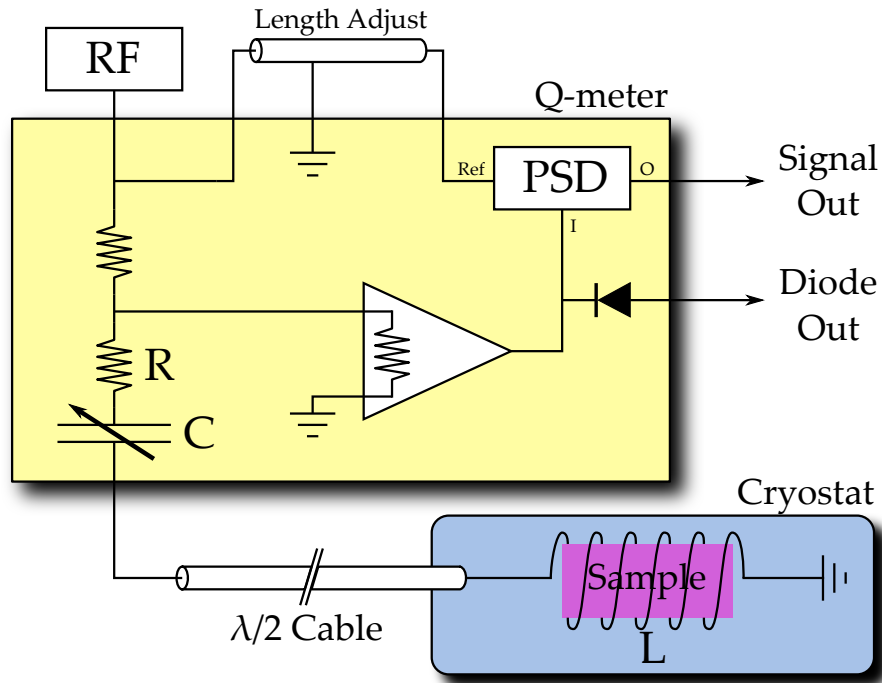


Figure 5.11: Shown is the NMR circuit. The yellow rectangle represents the actual Q-meter electronic box, while the blue shape represents the sample stick. RF is the NMR signal input. Drawing courtesy J. Maxwell. [12]

$$\chi(\omega) = \chi'(\omega) + i\chi''(\omega) \quad (5.6)$$

The magnitude of the absorptive term, $\chi''(\omega)$, is directly proportional to the polarization [18].

It is a basic fact that the phase shift for an LCR circuit is zero on resonance, where the resonance frequency is given by Eq. 5.7.

$$\omega_0 = \frac{1}{\sqrt{LC}} \quad (5.7)$$

The RLC circuit is tuned such that its resonant frequency, ω_0 , is the same as the Larmour frequency for the nucleus being measured. To do this tuning, a variable capacitor can be set such that the maximum magnitude of the Q-curve, as measured

by an RF diode, is centered in the sweeping band.

While the output from the RF diode does show the response of the material, a more sensitive method is to use a phase sensitive detector (PSD). The PSD used in the Q-meter is a balanced ring modulator (BRM), which is a three port device that takes two inputs. One input is a reference signal, taken by splitting the RF signal before the RLC circuit. The other input is the RF signal from the RLC circuit. The output is then proportional to $V \cos(\theta)$ where V and θ are the amplitude and phase of the second input relative to the reference [24]. The reference signal is passed through a length of cable that is adjusted such that the phase difference on resonance is 0; then the output of the BRM is just V .

The only significant difference between the NMR setup in the test lab and that used for the experiment is that the NMR at JLab places the capacitor in cryogenic liquid (LHe). This greatly reduces noise, allowing for better TE calibrations, at the cost of not being able to easily adjust the capacitance. Normally, the capacitance is adjusted with a small screwdriver as needed; with the capacitor under LHe, it must be set to the appropriate value before the system is cooled down as it cannot be changed without warming up again. This is known as “cold NMR” and for the deuteron, it drastically improves TE measurements, as shown in figure 5.12 and discussed in Ref. ???. With the normal warm NMR technique, the deuteron signal is barely recognizable, even with a substantial number of sweeps. The noise reduction of the cold NMR allows for more precise TE measurements of the deuteron, which results in less error in the measurement of polarization. Otherwise, the operation of the system is identical.

Target Stick Target material must be properly positioned inside of the magnet in order to reach the point of optimum field uniformity. It is also desirable to be able to

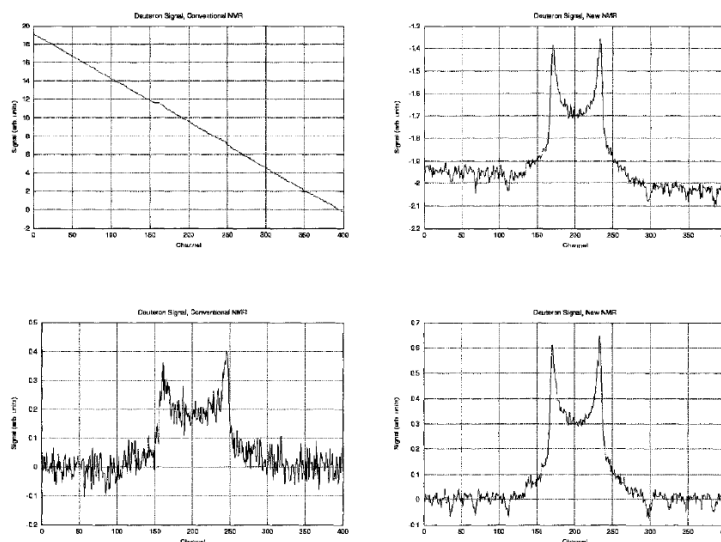


Figure 5.12: On the left are NMR signals taken with the conventional NMR setup, while the right is with the cold NMR. Top and bottom are the baseline-subtracted and polynomial-fit curves respectively. Figure taken from Ref. ??

polarize multiple separate loads of material without having to open the target, which takes time and warms up the nose. To accomplish this, a “stick” was designed with multiple cups for material. Each cup holds multiple cubic centimeters of material. Positioning is achieved via calibrated dowels, which hold the stick in place against the vacuum pressure. Also, various temperature readouts are mounted on the stick, so it also has a connector to pass these connections through the vacuum.

Fig. 5.14 depicts the stick used in the experiment, which is quite similar to the lab one. The main difference is that the stick used in Hall B is able to be raised and lowered remotely, and also has spaces for a carbon target and an empty target, which are used for calibrations. A photograph of the stick inside the apparatus is shown in Fig. 5.13, where one of the target cups can be seen in a mirror.

Measurements To run the apparatus properly, a variety of measurements must be taken. The vital measurement for determining polarization is the pressure in the

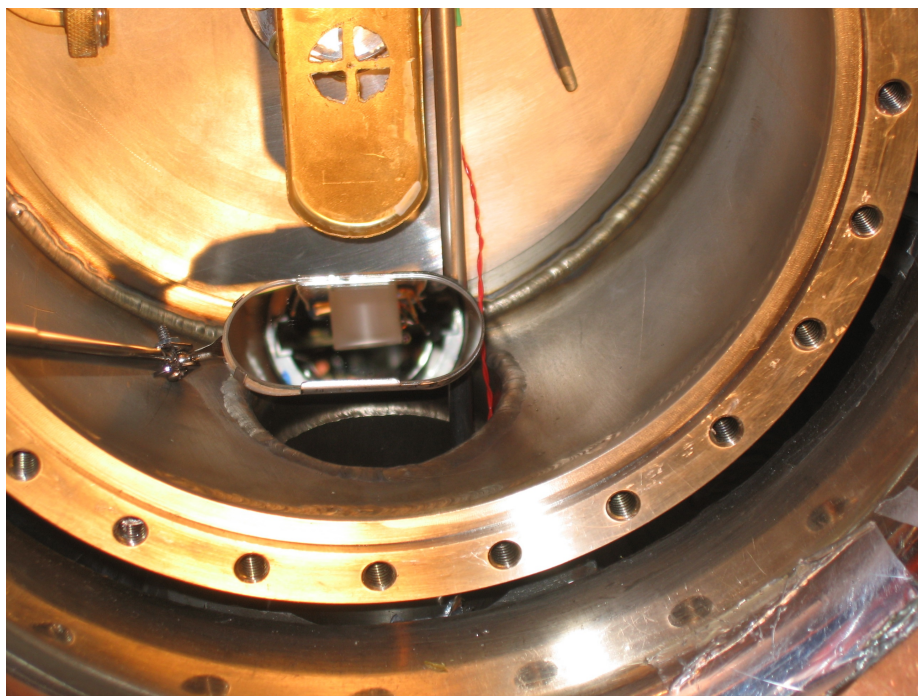


Figure 5.13: Photograph of banjo enclosure. Brass-colored piece at top is the target stick, with the cross-hairs target visible. The mirror shows a Kapton target cup mounted on the opposite side. The banjo is the cylindrical metal container. [15]

nose. This directly relates to the temperature of the LHe in the nose. Important for maintaining the level of helium are liquid levels gauges in the separator and nose, as well as flow rates for the separator and main refrigerator output. Chip resistors are also used to measure the temperature at several locations on the target stick. This is useful for knowing when the target is cooled down after a period of disuse, as well as for performing anneals.

Slow Raster As it passes through the target, the beam damages the ammonia, reducing its ability to polarize. With such a small beam spot, radiation damage would rapidly build up and render the granules useless. Additionally, the full amount of ammonia wouldn't be taken advantage of if the beam were to remain stationary. To solve these problems, the beam spot is rastered by a pair of magnets over the

target cup. This allows the beam to equally sample all the ammonia, as well as to deposit dose equally, extending the life of the target material. The raster magnet current values are recorded for each event, and a reconstruction of the target can be made. In this manner, it was discovered that part way through Part C, the ammonia granules had settled significantly, and the beam was hitting only LHe at the top. A decision was made to reduce the extent of the raster's vertical deflection, and so for the remainder of the run period, the raster scanned an oval instead of a circle.

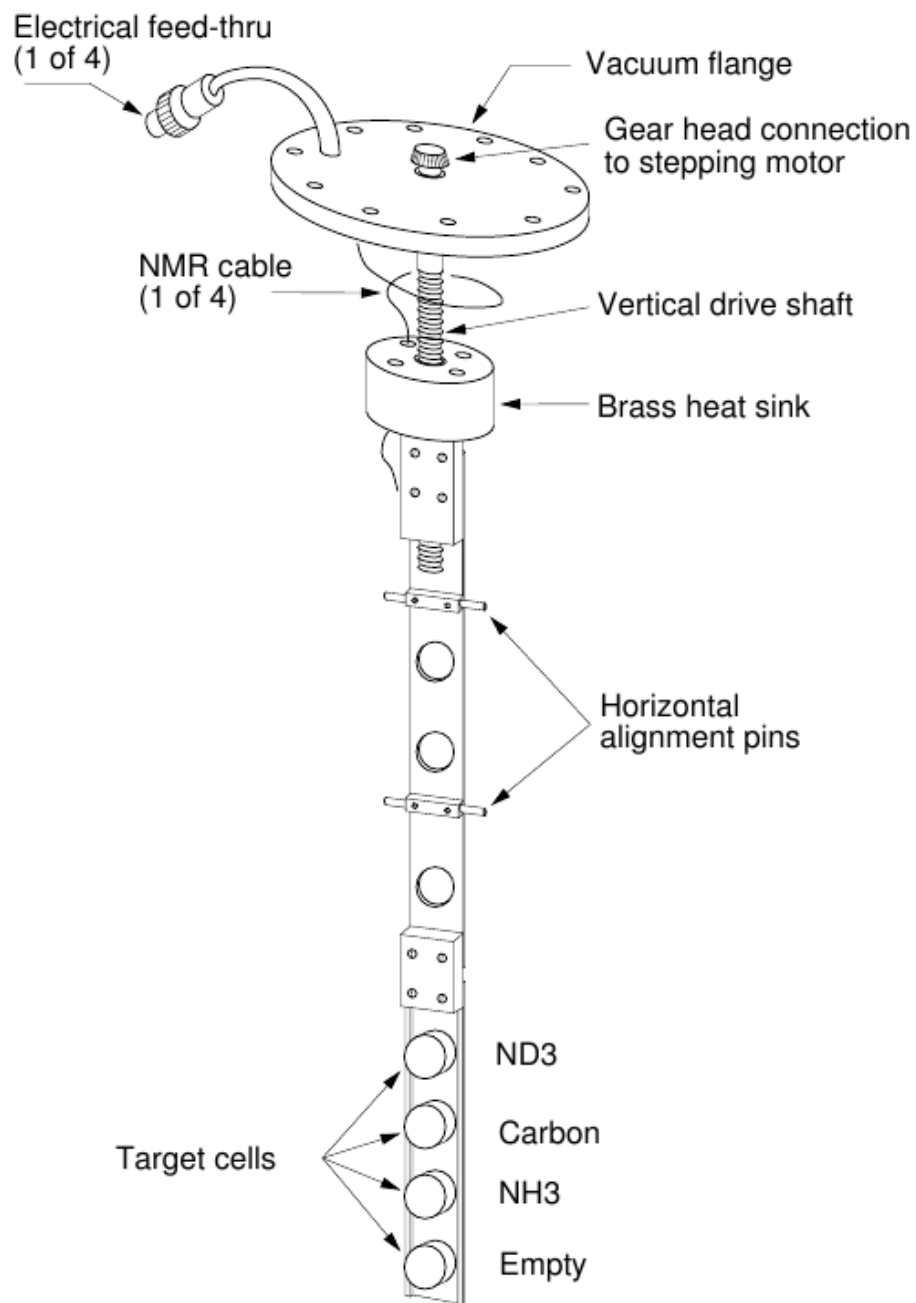


Figure 5.14: A drawing of the target stick. The mechanism for raising and lowering the stick in order to change which target cup is exposed to beam is shown, along with the position of target cups. The stick is approximately a meter in length and each cup has a radius of 1.5 cm. Figure from Ref. [22].

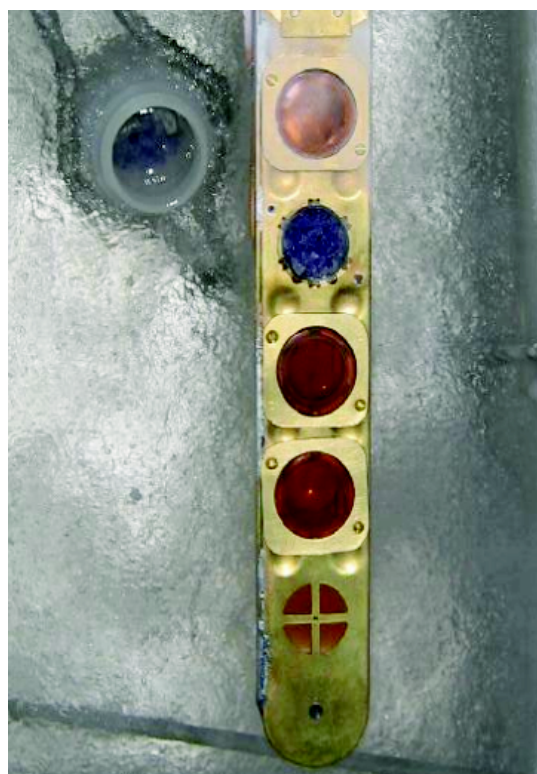


Figure 5.15: Shown is a digital photograph of the target stick after having been loaded with ammonia. The open cup is the cup referred to as “bottom” and the purple color inside is the ammonia. The bottle from which the ammonia was taken is held next to the stick for comparison. Both the stick and the bottle must remain submerged in nitrogen in order to preserve the radicals that were introduced by irradiation.

5.3 Ammonia

The choice of material for a polarized target relies on several variables. One of the most important is the maximum polarization that can be reached. Relatedly, how well the material maintains its polarization as it accumulates radiation damage while in the beam is also very important. Additionally, the density of polarizable nuclei in the material is important, and plays into the dilution factor, discussed in Sec. 8.4. Ammonia, being composed of one Nitrogen nucleus and three hydrogen (or deuterium) nuclei, has a polarizable nuclei ratio of 3/17 (or 6/20). Although some hydrocarbons contain larger ratios, the ability of ammonia to be polarized and to maintain polarization with radiation damage makes it the material of choice for electron scattering experiments.

5.3.1 Freezing

Ammonia is purchased from chemical supply companies in a gas cylinder because it is gaseous in phase at standard temperature and pressure. To create granules that are useful as a target material, the ammonia must be frozen, crushed, and graded.

Freezing is done in a small apparatus in a fume hood at UVA. The apparatus consists of some tubing to connect to the cylinder of ammonia, and a cylindrical stainless steel tube that has a removable bottom. The apparatus is first evacuated and then repeatedly flushed with nitrogen gas and evacuated to be sure there is very little contaminating air. Ammonia gas is then let into the system while the stainless tube is submersed in liquid nitrogen. Ammonia condenses and freezes into the tube, and once a sufficient volume is achieved, the plug of solid ammonia is dropped into a liquid nitrogen bath. This plug is crushed with a ceramic pestle in a specially made grating system which keeps the ammonia submersed in liquid nitrogen at all times.

“granules” of ammonia, approximately 2 mm in diameter on average, are obtained in this way; Fig. 5.16 shows a load of unirradiated ammonia.



Figure 5.16: Ammonia, frozen and crushed into granules.

5.3.2 Irradiation

To add the radicals necessary for DNP, the frozen ammonia is subjected to an electron beam. The MIRF (Medical Industrial Radiation Facility) at NIST is the standard provider for this service to the Polarized Target group at UVA, Irradiation is done under liquid argon, due to a small explosion problem that occurs when irradiating liquid nitrogen. In the past, a 19 MeV beam with about 10 μ Amps was used; however, due to radiological concerns, uncovered by the author, about the production of Chlorine-19, a radioactive element, the beam energy was reduced to 14 MeV. This new energy is below the threshold for the production of Chlorine-19, so the contamination is significantly reduced. The ammonia is placed into a “basket” like the one shown in Fig. 5.17, which must be rotated after about half the dose has been deposited so that

the ammonia within receives equal irradiation. After receiving about 10^{17} electrons per cm^2 , the material is removed from the beam. A properly irradiated sample will have taken on a deep purple color, such as in Fig. 5.18.



Figure 5.17: A basket used to hold frozen ammonia for irradiation. Length is slightly less than three inches, which is long enough to get the job done. Photo courtesy J. Maxwell [12]

5.3.3 Anneals

While taking beam, the ammonia receives radiation damage which decreases its maximum polarization. Luckily, the maximum polarization can be restored in a process called “annealing.” In this process, the ammonia is heated to somewhere in the range 70 K - 90 K and held at that temperature for a period of roughly half an hour. This is accomplished by running a current through a small coil of wire on the target stick. While this process can be done repeatedly, the next anneal will be required after a shorter amount of time in the beam due to the accumulation of radiation damage. Eventually, the time lost by pausing data taking to anneal outweighs the



Figure 5.18: Ammonia granules after receiving a dose of radiation. The drastic change in color from white to dark purple is indicative of a large dose of radiation.

benefits to polarization and so the target material must be replaced. In Hall B, only 6-9 nanoAmps of beam current are used, so radiation damage accumulates relatively slowly. Accordingly, an anneal is only required every 3-4 days, and the single target load of deuterated material sufficed for the entirety of Part C (see section Sec. 6 for a description of the experimental run period).

Chapter 6

eg1-dvcs

6.0.4 Experimental Overview

The experiment (nick-named “eg1-dvcs”) from which the data for this analysis was obtained used the 6 GeV longitudinally polarized electrons from CEBAF at Jefferson Lab. The beam was directed onto the polarized target, a 0.025 radiation length, longitudinally polarized, solid ammonia target immersed in liquid helium [25, 26] as described in Chapter 5. Scattered electrons were detected in CLAS [13], using the various subsystems described in Chapter 4.

The typical beam current was 7 nA, which, over the course of 6 months of data taking, resulted in approximately 2×10^{17} electrons encountering the target. The beam polarization, as periodically measured using Møller scattering in an up-stream polarimeter, averaged 85% for the first 3/4 of the experiment. A lower polarization of about 75% was delivered during the remaining time, in order to accommodate the needs of Hall A and Hall C[27].

About 70% of the running time was on polarized protons (NH₃ target), 20% on polarized deuterons (ND₃ target), and 10% on an unpolarized carbon target, used

as a reference. The 1.5 cm diameter cups typically contained 1 gm/cm^2 of material immersed in a 2-cm-long liquid helium bath. Due to the extreme narrowness (sub-millimeter-diameter) of the beam and the susceptibility of the target material to deleterious effects from beam-heating and radiation damage, the beam was uniformly rastered over the front face of the target, in a cycle lasting a few seconds. The beam position, averaged over a few minutes or longer, was kept stable at the 0.1 mm level using feedback from a set of beam position monitors. The split solenoid superconducting magnet used in the target polarization process provided a highly uniform 5 T magnetic field at the target, with a fringe field that extended about 20 cm forwards and backwards from the target center.

Scattered electrons were detected from about 17 to 48 degrees in the azimuthal direction. Particle momenta and scattering angles were measured with the drift chamber (DC) tracking system with a relative accuracy of 0.3% to 2% in momentum, and about 1 mr in angle. Electrons were separated from a significantly larger number of charged pions using the Cherenkov detectors and the electromagnetic calorimeter. A hardware trigger system made a first selection, rejecting about 90% of pions while keeping close to 99% of electrons, so that the data acquisition system would not waste time capturing useless events [27]. The hardware Cherenkov and calorimeter thresholds were adjusted to give a trigger rate of about 3000 Hz, and a “dead time” in which no trigger could be accepted of about 10%. An additional unbiased trigger was prescaled by a large factor in order to measure the efficiency of the main electron trigger[27].

The data taking was divided into three parts: Part A in early 2009 used NH_3 as the target, centered at 58 cm up-stream of CLAS center ($z_0 = -58 \text{ cm}$); Part B (mid 2009) also used NH_3 , this time at $z_0 = -68 \text{ cm}$; and Part C (September 2009) mostly used ND_3 as the target, again with $z_0 = -68 \text{ cm}$. The target position was changed

to increase the acceptance for π^+ and π^- events which are used for semi-inclusive (SIDIS) analysis. Each part had slightly different primary beam energies (between 5.7 and 6.0 GeV, with several days at 4.8 GeV at the end of Part A). The CLAS torus polarity was set to bend electrons inwards for almost all of parts A and B, and about two thirds of Part C. The field strength was 2/3 of maximum[27].

The main difference between this experiment and previous CLAS runs with polarized ammonia targets was the addition of the Inner Calorimeter. While not used in the present analysis, this device had the advantage of absorbing much of the background from Møller scattering, allowing for running at higher beam currents than usual, but the disadvantage of blocking electrons below scattering angles of 20 (17) degrees for Part A (parts B and C). Other differences included the use of a 50% longer target cell and nitrogen-14 instead of nitrogen-15 in the ammonia.

6.0.5 Experimental Context

CLAS has already been used to measure the inclusive spin structure functions of the deuteron (g_1^d) prior to the present experiment. The results from the 1998 run (“eg1a”) and 2000 run (“eg1b”) have been reviewed and published [28, 29]. A detailed archival paper for eg1b has been reviewed [30], and will soon be submitted for publication. The eg4 experiment, which ran from January to May 2006, is still under analysis. All the experiments, including eg1-dvcs, used the same polarized ammonia target [25]. Eg1a and eg1b used a wide range of beam energies (from 1.7 to 5.7 GeV) to cover a large kinematic range, from the nucleon resonance region to deep-inelastic scattering (DIS). Eg4 used lower beam energies and very forward scattering angles to focus on the resonance region at low Q^2 . The present experiment used only 6 GeV electrons (except for 4 days at 4.8 GeV, only for proton runs) and relatively larger scattering

angles to focus on the DIS region [27]. The main focus of eg1-dvcs was on semi-inclusive DIS (SIDIS) and deeply virtual Compton scattering (DVCS), both of which required detection of photons at small angles. For this reason, the Inner Calorimeter (IC) was installed.

The eg1-dvcs data set allows for several different physics analyses, most of which have many features in common. These include information of the beam and target parameters, improvements to data processing, and data quality checks. Most of these features are detailed in eg1-dvcs Technical Notes, which are referenced throughout this document, and a list of which can be found on the eg1-dvcs wiki: https://clasweb.jlab.org/rungroups/eg1-dvcs/wiki/index.php/Main_Page

Part III

The Analysis

Chapter 7

Data

The analysis presented in this dissertation is for the inclusive process, which means that all final scattering states are included in the analysis, as long as the scattered electron was detected. The various components of CLAS need to be calibrated and the overall quality of the data must be checked in order to insure the detector was performing properly. The detected particles must then survive a set of cuts designed to reject particles that are not electrons. Once these steps have been taken, the particles can then be counted and binned in their kinematic variables and helicity state of the beam for the calculation of the asymmetry.

During the running of the experiment, discussed previously, raw data amounting to approximately 50,000 files were taken. Each file is about 2 GB in size and stems from just a few minutes of beam time. The files are grouped into “runs” consisting of about 80 files, on average, that were collected consecutively. Generally, a run would consist of several hours of data, during which the experimental configuration should not have changed. This raw data is stored on the “silo”, which is Jefferson Lab’s automatic magnetic tape storage system.

7.1 Processing

Each file from the silo is processed in a procedure known as “cooking”. Cooking was done using the standard CLAS analysis package. Several iterations of analysis were performed as calibrations improved, with each iteration taking several weeks of run time on the Jefferson Lab computing farm. The results in this analysis are from Pass 1, version 5 for Part C. As of the time of writing, Parts A and B were using Pass 1, version 3.

The amount of data is very large and accessing this data from the tape silo is slow. To help alleviate this problem, the first step of the cooking process is to select a subset of the detected events that will be used by every analysis. This subset contains events that are reasonably likely to contain an electron. Because every analysis requires, at the least, detection of the scattered electron, these files are used for all of the physics analyses. This subset is stored on hard disk in both PAW ntuples and ROOT trees [31].

7.2 Post-Processing

After cooking with the standard analysis packages, there were a few enhancements that could be provided that were more specific to eg1-dvcs. One of these enhancements is an improved method of calculating how particles move through the target magnetic field. The standard method “swims” particles from their drift chamber tracks backwards to a plane perpendicular to the sector in which the tracks were detected. Since we are only looking for events with vertices in the target, a more accurate method is to swim back to the x and y coordinates specified by the raster magnet [27]. This method used the track coordinates at DC1 and a fit to a large ensemble of simulated

forward-swimming particles [27]. This method guarantees that the particle track will have originated from the beam position, as specified by the raster magnet setting. The outcome was approximately a factor of two improvement in angular resolution; this was verified by examining the width of the beam energy, E_0 , by reconstructing it from the electron and proton scattering angles in ep elastic scattering. Figure 7.1 shows the spectra both before and after correction; improvement is obvious. A full description of this method is contained in Ref. [32].

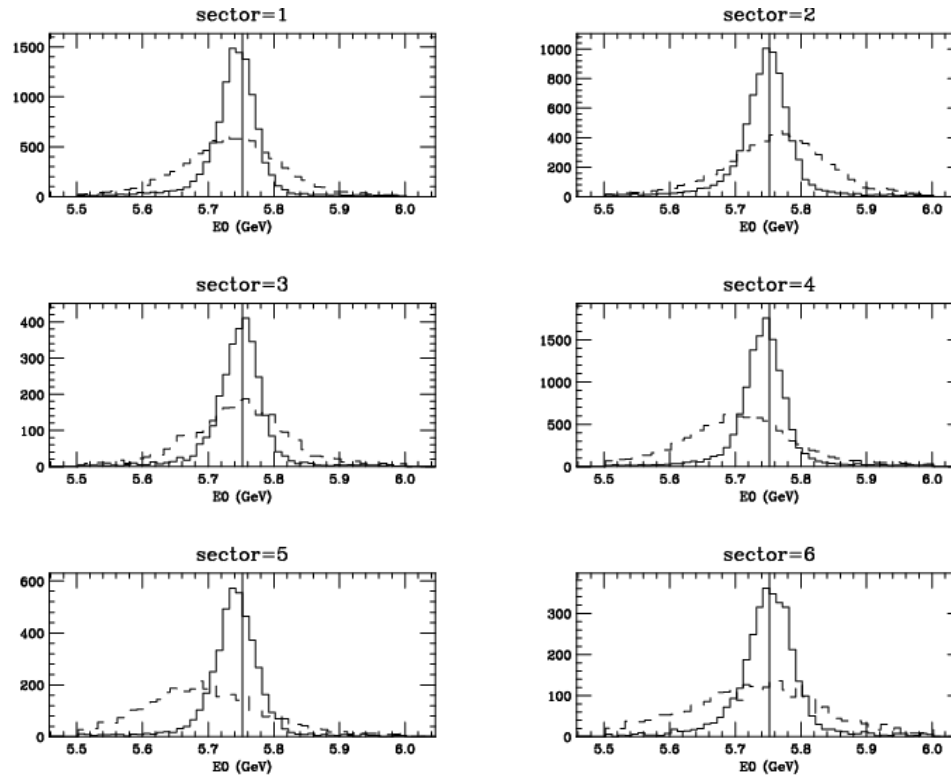


Figure 7.1: This shows the Beam Energy, E_0 , distribution derived from ep elastic angles for each sector for a typical NH_3 run. Solid-line histograms use the new method to fit to a line while dashed-line histograms are from the standard method. [32]

Another enhancement specific to eg1-dvcs relates to the helicity variable. Due to a concurrently running experiment in a different hall, the beam helicity was not directly available for each event during Part C. Instead, the information was delayed;

each event corresponded to that of the helicity “bucket” (a 1/30 sec time interval) previous to the present [27]. It was possible to obtain the actual helicity values in two separate ways: one way is to construct a look-up table by making multiple passes through the data, and the other is to use the known pattern of helicity reversals, which is determined by the first 32 helicity “buckets” in a given run. For all but two runs, we were able to reliably obtain the beam helicity for each event in Part C (see Ref. [33]).

7.3 Calibrations

7.3.1 Standard Calibrations

Standard calibration procedures were performed for each of the subsystems in CLAS. These include: drift chamber (DC) alignment using straight-through tracks [34]; DC timing alignments [35]; gas Cherenkov detector (CC) pulse height alignment using single photo-electron peak [36]; time-of-flight scintillator (SC) timing corrections; and electromagnetic calorimeter (EC) pulse height corrections using cosmic rays [27]. Timing and position resolutions for each of the systems, after calibration, were similar to those obtained during other electron running periods [13]. Calibrations were made frequently enough to ensure very good stability for most of the systems. The exception was the EC gain, which could vary substantially over a period of hours. Because the gains of the PMT’s in any given sector vary in a correlated way, an overall gain adjustment could be used to obtain constant energy resolution and normalization on a run-by-run basis.

7.3.2 Raster Corrections

An additional calibration specific to experiments with polarized targets was done. The beam position at the target needed to be calibrated because it depended on steering in the accelerator as well as the strength of the raster magnets. The raster magnets scan the beam over the target cell so that accumulated radiation damage does not destroy the polarization [37]. Section 5.2 describes this feature of the target further. The x and y magnetic fields (in units of “ADC counts”) were recorded for each event trigger. By minimizing the width of the reconstructed target position along the beam line (z), the relation between magnet current and beam position was determined. In the case of no raster magnetic field, the beam position relative to CLAS center was found. Also determined from the fit was the position of the target center along the beam line, relative to the center of CLAS. This was found to be -57.95 cm for Part A, and -67.95 cm for parts B and C of the run. These values are about 0.5 cm different than the physical survey values. See Ref. [37] for more details.

7.3.3 Magnet Angle Correction

Another calibration specific to this experiment was the determination of the orientation of the target solenoid with respect to the beam line. The primary method used was to make the opening angle of reconstructed electron-positron pairs (from photon conversions) as close to zero as possible. The result was an approximately 3 mr tilt, resulting in a significant polar deflection of charged particles, on top of the azimuthal rotation characteristic of a solenoidal field. The results were confirmed using the co-planarity of ep elastic events, and incorporated into the track reconstruction. See Ref. [32] for more details.

7.4 Event Selection/Particle Identification

All of the analyses for eg1-dvcs require detection of the scattered electron, and in this particular analysis, the only important particle is the electron; therefore it is crucial to properly identify this particle. A number of different criteria are used to select electrons, using data from all parts of CLAS. The two detectors that are most useful for particle ID, however, are the threshold gas Cherenkov detector (“CC”), which has a pion threshold of 2.6 GeV, and the lead-scintillator electromagnetic calorimeter (“EC”) [27]. Before any selections are made after the data is acquired, however, the electronic trigger requires at least 1 photo-electron (p.e.) in the CC and an energy deposition of 0.5 GeV in the EC.

The simplest check, just testing to make sure a proper event with enough information was recorded, is to first require that a time-based drift-chamber (“DC”) track have negative charge, use at least five of the six super-layers in the tracking system, and have a signal in each of the CC, EC, and scintillator time-of-flight counter system (“SC”). A further requirement was that the CLAS sector number for each the subsystems (DC, CC, SC, and EC) be matched. We then required seven additional particle ID cuts [27]:

- Number of photo-electrons (p.e.) in the CC greater than 2.0.
- Energy in EC divided by momentum P (with 0.12 GeV offset) greater than $0.80(E/P)_{peak}$, where $(E/P)_{peak}$ is the peak of the $E/(P - 0.12)$ distribution (from a first pass through the data), averaged over each run, for each sector separately. This procedure was performed to take out slow drifts in the EC gain, which were especially evident after the high voltage on the PMTs had been off for a significant period of time.

- Target vertex position along beam line (z) within 3 cm of the polarized target center.
- A $\pm 4^\circ$ cut was made on the difference between the electron's azimuthal angle at the first drift chamber layer and the azimuthal component of the electron's momentum at the same place. Particles with higher $\delta\phi_{DC1}$ are more likely to have scattered from materials that were not part of the target and so can have inaccurate kinematics. Fig. 7.8 shows the Z Vertex cut both with and without the $\delta\phi_{DC1}$ cut. Since it is plotted in log scale, several features are visible in the plot with the $\delta\phi_{DC1}$ cut, which correspond to various target and beamline vacuum windows and foils. See [38] for more details.
- Cherenkov mirror number aligned with value expected from track trajectory (as defined by nearby SC paddle number) within 2 SC paddle numbers. For historical reasons, we use a quantity called Cherenkov χ^2 (C2), which is the difference in radians squared. Two SC paddles corresponds to our cut value of 0.05. The definition of C2 was modified from the normally used one (specifically designed for inbending electrons from a target centered in CLAS along the beam line), in order to work properly for any torus field and any target position [39]. The new method uses the feature that the SC paddles and CC mirrors are close together so that their correlation is relatively insensitive to the track trajectories.
- Cherenkov signal time agrees with EC signal time within ± 4 nsec.
- The electron scattering angle θ_e was required to be less than 40 degrees for Part A, and less than 45 degrees for parts B and C. The reason was that particles at larger angles could pass through the significant amounts of heat shields and super-insulation in the target. The increased radiation length of these materials

resulted in high pair-symmetric backgrounds.

- Electrons whose trajectories passed too close to the lead shielding around the IC (or the IC support stand) were removed [40]. The looser of the two cuts described in this reference was used. Since the IC was octagonal in structure and has a thick support plate obscuring sectors 5 and 6 while CLAS is hexagonal, the cut depended on azimuthal angle but roughly corresponds to 20 degrees (16 degrees) for Part A (parts B and C) for an electron originating at the target center. The reason for this cut is that electrons passing through short lengths of the shielding could survive, but with strongly modified angles and momenta from multiple scattering and Bremsstrahlung, thus resulting in incorrect determination of their kinematic values. Most of these events have already been removed by the vertex and $\delta\phi_{DC1}$ cuts.

Figures 7.2 through 7.6 show the quantities being cut on, with each of the other cuts applied. It can be seen that the CC p.e. cut is the most powerful one in rejecting background, visible as the peak near 1 p.e. This background is primarily due to knock-on electrons from pions interacting in the Cherenkov window and gas medium. The next most powerful cut is the EC one. The EC to CC timing cut removes about 10% of events, which appear to be random coincidences. Note, the timing peak is not centered at zero for all runs (it is shifted to positive values for the run shown), so a wider cut than might be expected based on this plot was used.

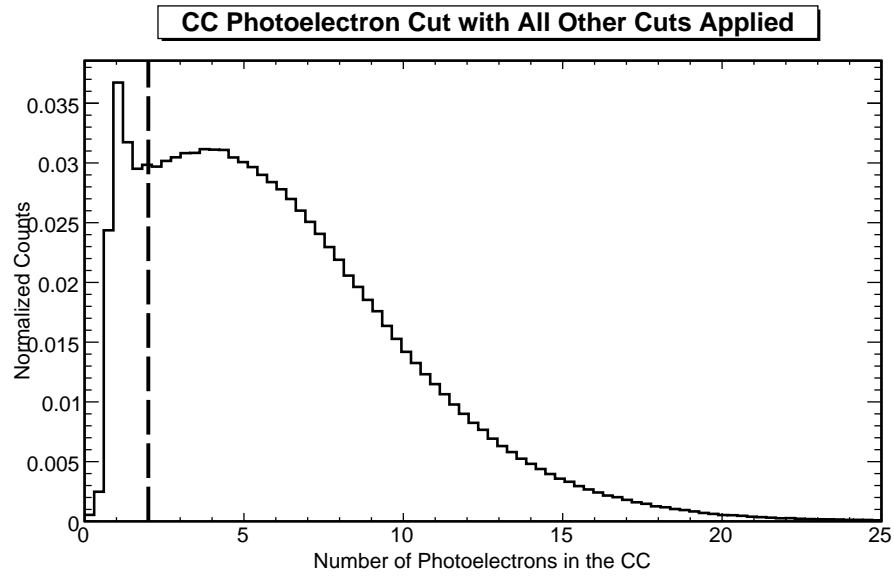


Figure 7.2: Distribution of p.e. in the CC for events with all other electron cuts applied. The vertical line shows the cut value used in the analysis.

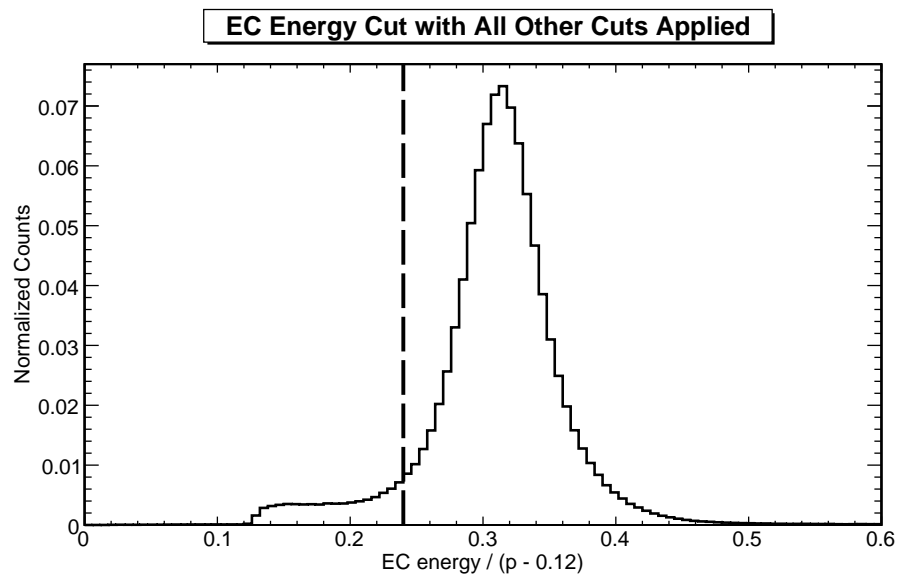


Figure 7.3: Distribution of EC energy divided by track momentum (minus 0.12 GeV) for events with all other electron cuts applied. The vertical line shows the cut value used in the analysis. The lack of events below 0.12 is mainly from the hardware trigger.

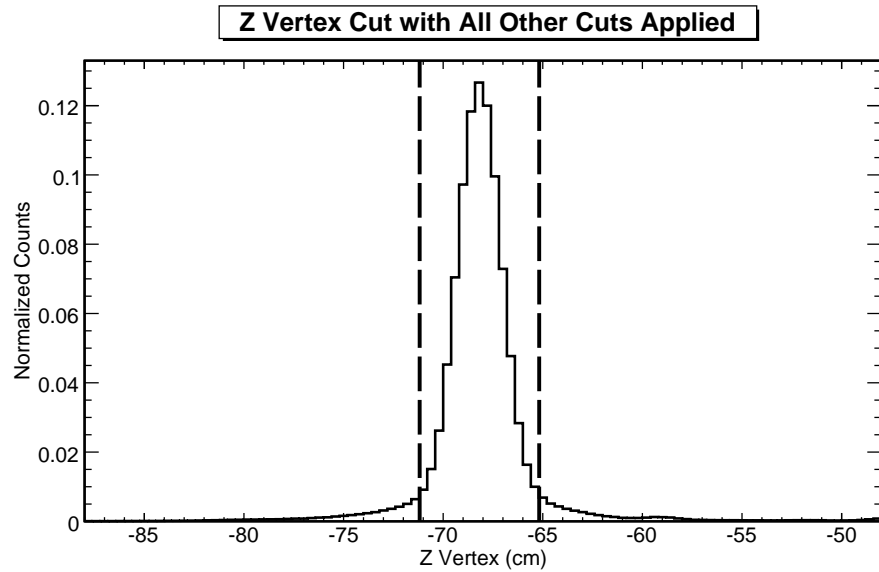


Figure 7.4: Distribution of vertex z for events with all other electron cuts applied. The vertical lines shows the cut values used in the analysis.

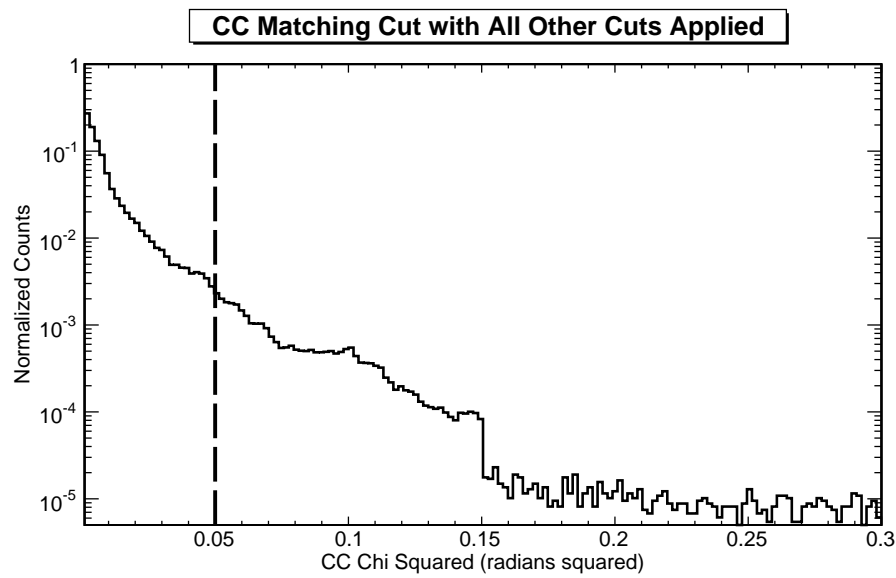


Figure 7.5: Distribution of χ^2 in the CC for events with all other electron cuts applied. The vertical line shows the cut value used in the analysis. χ^2 is the difference in azimuthal angle between the particle track and the position predicted by the hit mirror in the Cherenkov, measured in radians squared.

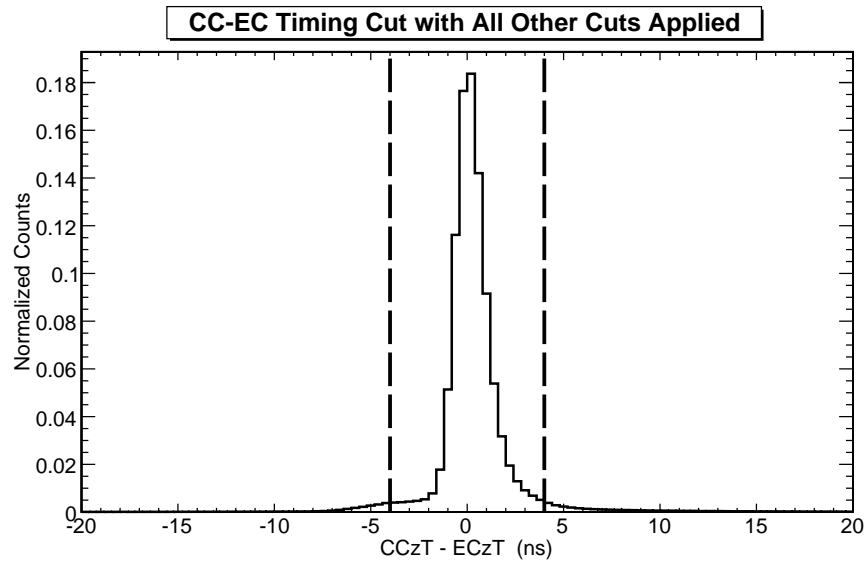


Figure 7.6: Distribution of time difference between CC and EC for events with all other electron cuts applied. The vertical lines shows the cut values used in the analysis.

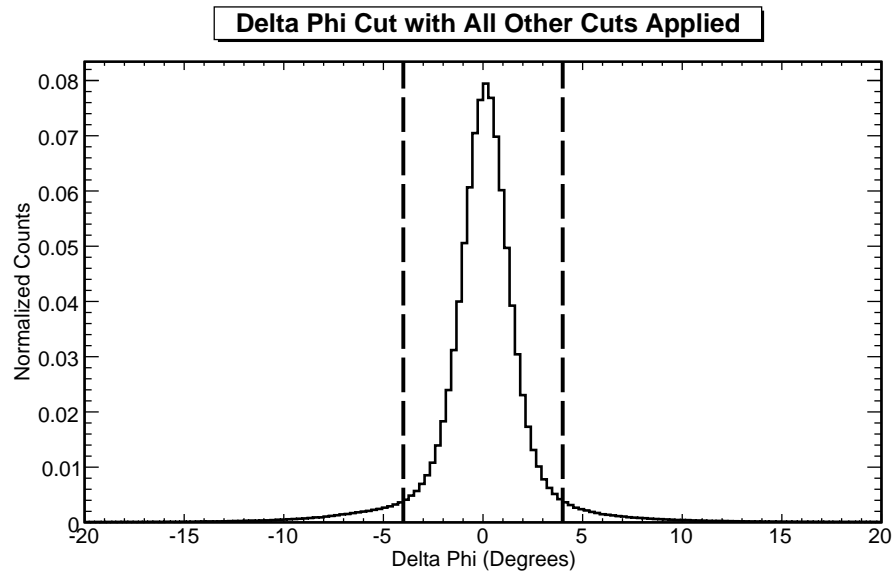


Figure 7.7: Distribution of $\delta\phi_{DC1}$ with all other cuts applied. The vertical lines shows the cut values used in the analysis.

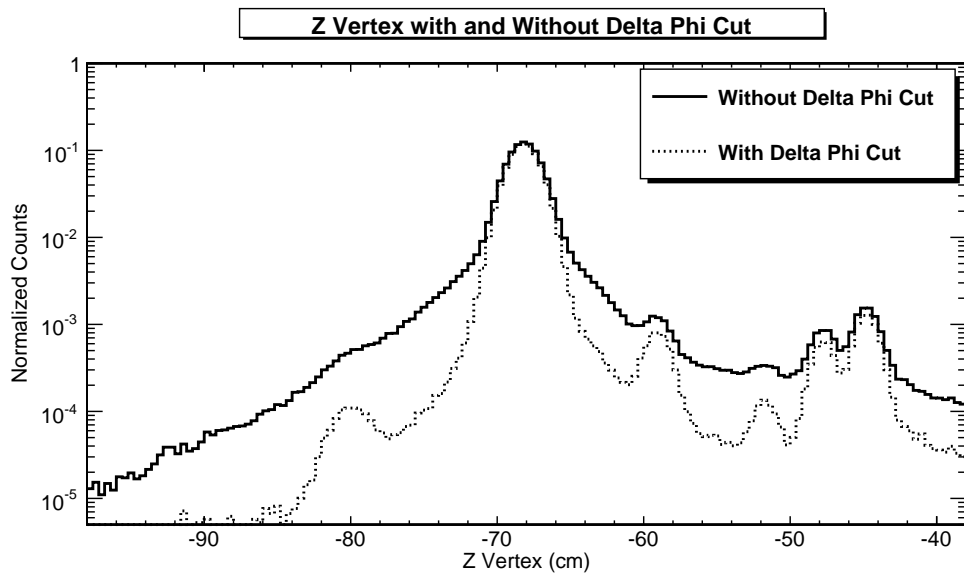


Figure 7.8: Z Vertex distribution plotted in log scale. The distribution is shown both with and without the $\delta\phi_{DC1}$ cut. As can be seen in the curve with the $\delta\phi_{DC1}$ cut, the broad background is significantly reduced without much change in particles that directly scatter from the target. The various peaks that appear after the delta phi cut is implemented correspond to features of the target apparatus such as the evaporation chamber windows and the magnet vacuum window.

7.5 Quality Checks

After the calibrations have been done and suitable particle id cuts have been made, the data is almost ready for analysis. There are, however, still a few reasons that the data may be unfit to use. Most of these reasons are related to various problems that can occur with the beam or detectors, so any “cuts” made based on the quality checks are generally applied on a file-by-file basis.

7.5.1 Beam Scraping

Due to the multitude of changing variables involved in controlling the electron beam, the position of the beam can change over time. This can lead to problems if the beam comes into contact with the walls of the target cell, since these walls are plastic instead of ammonia and are unpolarized. Thanks to careful monitoring during the run period, very few data were taken with the beam scraping the target cell’s walls. An off-line check for hot spots in the detector revealed a few files with this problem [41], and they were excluded from further analysis.

7.5.2 Rate Stability

In order to avoid significant corrections to measured asymmetries (target single spin asymmetries, in particular), and also to obtain reliable dilution factors from the comparison of ammonia and carbon target rates, we removed data files where an obvious drop in the efficiency of the detector occurred [42, 27]. The most common reason for decreased efficiency was that the DC high voltage tripped off, with the next most common being the EC high voltage tripping off. Other problems were associated with the beam quality; issues such as decreased beam current or wandering beam position are not uncommon. In two cases, the Wein filter (which controls the beam

helicity direction) was reversed in the middle of a run. Standard procedure is to end a run when the Wein filter is moved, however mistakes are sometimes made. These runs were removed. Some files were also removed due to low target polarization. In total, less than 5% of the data was discarded for one reason or another.

The stability of the inclusive electron rates is illustrated in Fig. 7.9. The rates have been corrected for the luminosity-dependence discussed in Section 9.2.3, as well as the raster position correction for some of the ND₃ runs as discussed in Section 7.3.2. The rates for NH₃ (blue and red points for top and bottom targets) are generally stable within one percent for long periods of time. Over longer time periods, there are slow drifts, possibly corresponding to changes in effective target thickness or overall detection efficiency. The stability of the carbon runs (black points) is quite good for parts B and C, but less so for the Part A, for which the rates have a total spread of about 7%. The reason for this instability was not found after an exhaustive search.

7.5.3 Asymmetry Stability

Another important quality check, for all analyses, is the measurement of the average inclusive electron double-spin asymmetry. Although this is the asymmetry used for the analysis described in this thesis, the quality check is done before applying the majority of the corrections.

The double-spin asymmetry is essentially zero for carbon targets, and generally at least 3-sigma difference from zero for polarized targets, which makes this a particularly useful way to check if the target being irradiated is the one listed in the run data base. However, for Part C the rates for ND₃ and carbon targets are very similar, so this method could not be used to check if any runs were associated with a wrong target, which happened for about ten runs all together. [27]

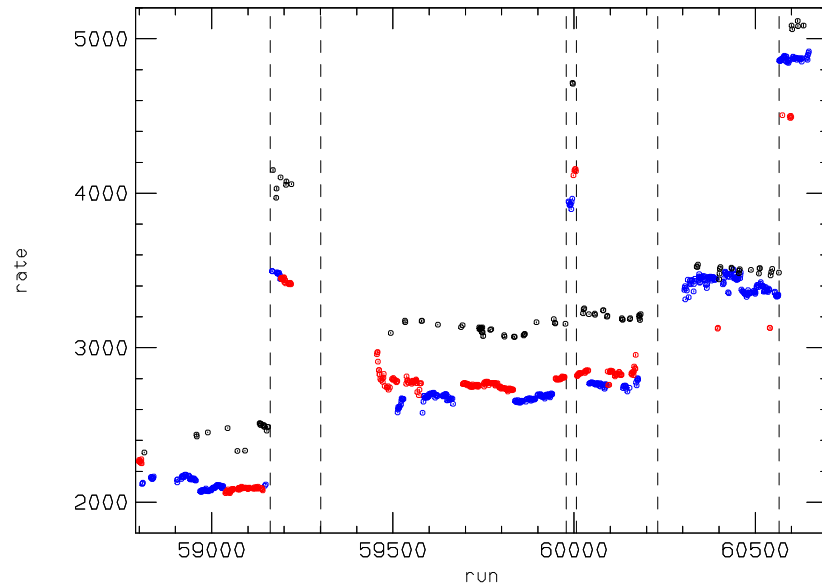


Figure 7.9: Rates of electrons passing inclusive pid cuts, normalized by incident beam charge, vs. run number. Deuteron runs (Part C) start after run 60232, and are shown in blue. The black points are carbon runs, the red points for the bottom NH_3 targets, and blue points for the top NH_3 target in parts A and B. The vertical dashed lines correspond to changes in beam energy or torus polarity. Figure courtesy of P. Bosted [27].

The sign of the asymmetry is also checked, because it can show whether the overall beam and target polarization signs were correct in the data base. Several mistakes were found; for example when the beam half-wave-plate was changed at a different time than initially recorded. Finally, this check was used to remove two runs where the half-wave plate was changed in the middle of a data run, and several runs where the target polarization suddenly dropped to zero due to target problems. [27] Figure 7.10 shows the final results for the double spin asymmetry as a function of run number. In Part C, the NH_3 and ND_3 targets could also be distinguished due to the much smaller asymmetries for ND_3 compared to NH_3 . Once the problems discussed above are taken into account, the polarized target runs all show a positive asymmetry and the carbon runs are all consistent with zero.

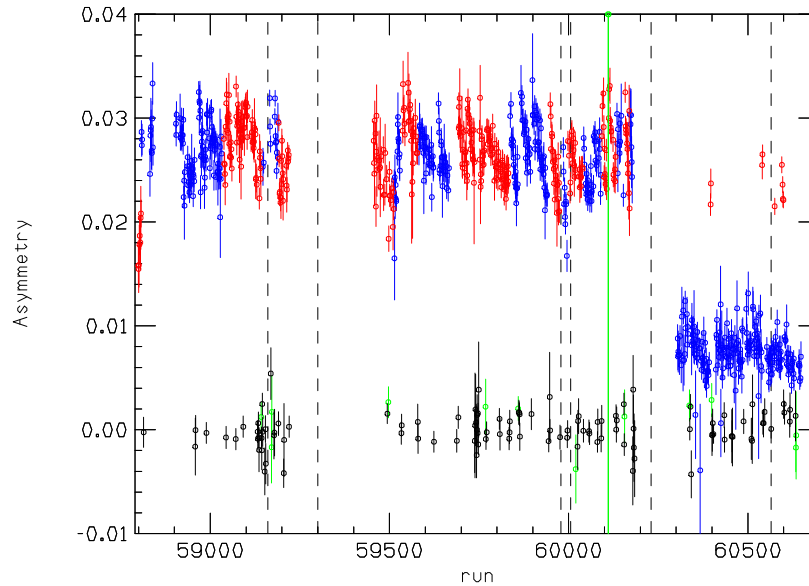


Figure 7.10: Average raw double-spin asymmetry as a function of run number. The color scheme is the same as in 7.9. Figure courtesy of P. Bosted [27].

7.5.4 Electron Detection Efficiency

Although the electron detection efficiency cancels in forming the double-spin asymmetries used to determine g_1 , it is still important to check that it is reasonably high so that enough data is being collected and we can obtain the smallest possible statistical error. The efficiency was determined by comparing the measured rates from the carbon target to those expected from a model of the target composition and inclusive radiated cross sections [43]. Only events within $\pm 7^\circ$ in azimuthal angle of the center of each sector were used, to ensure that the acceptance would not be blocked by the torus coils. [27] A correction to the data was made for contributions from pair-symmetric production, similar to the pair-symmetric correction that will be applied to the final data as described in Section 8.5. As shown in Fig. 7.11, the results show efficiencies between 70% and 95% over most of the kinematic range of the experiment. Gaps in the drift chamber efficiency can be attributed to dead wires, and the very low Cherenkov detector efficiency for sector 5 for parts B and C [27] is explained by a

problem with the detector itself: a large leak, so that the gas medium was air instead of the desired C_4F_{10} . For a more complete description of this check, see Ref. [44].

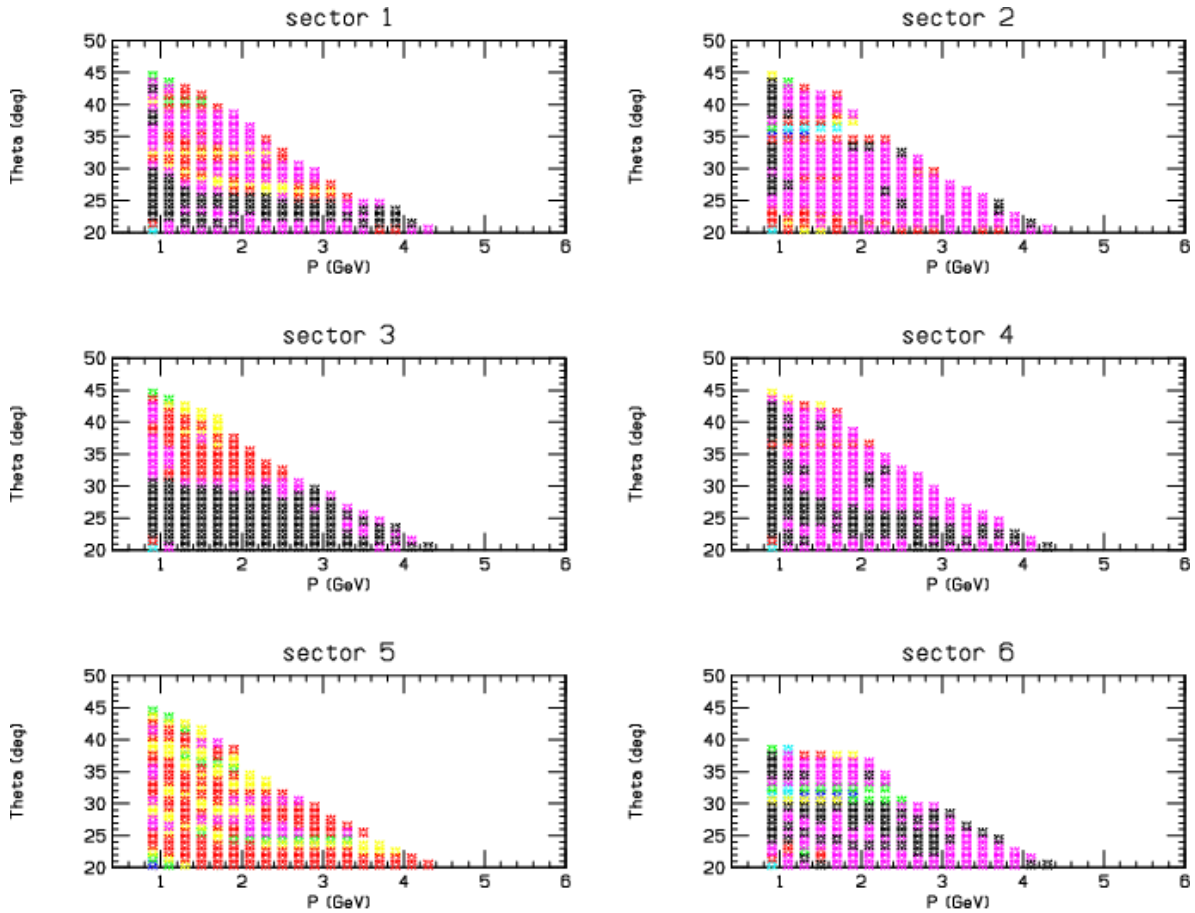


Figure 7.11: Electron detection efficiency as a function of electron momentum P and azimuthal scattering angle θ for each sector for the 5.9 GeV beam energy runs of Part B. The color scheme, from lowest to highest efficiency in the interval 0 to 1, has the order blue, cyan, green yellow, red, magenta, and black (i.e. black is 0.84 to 1.0). Figure courtesy P. Bosted.

7.5.5 Ad-hoc Momentum and Angle Corrections

Another quality check was to determine if any ad-hoc momentum or angle corrections were needed. Systematic variations in momentum that depend sector number, momentum, or angle have been found for CLAS experiments in the past. These cor-

rections are due to slight misalignments in the drift chambers or movements caused by the forces exerted by/on the coils.

Perhaps due to the careful DC alignment done for this experiment using both surveying and straight-through tracks [34], combined with the improved tracking through the target and torus magnetic fields discussed above [32], it was found that no significant improvements could be made with ad-hoc corrections [27]. This was determined by looking for deviations from the mass of the proton, M , for the missing mass in the reaction $ep \rightarrow e\pi^+(n)$. A neutron was required to be detected within a few degrees of the predicted angle to reduce backgrounds. For more details, see Ref. [45].

7.5.6 Beam Energy

The beam energy, E_0 , is a vital quantity in this analysis because it contributes to the kinematic factors Q^2 , x , as well as the depolarization factor, D . Therefore, we must determine the value of E_0 as well as possible.

The primary method was based on ep elastic scattering, using the relation

$$E_0 = M\{[\tan(\theta_e/2)\tan(\theta_p)]^{-1} - 1\}$$

where θ_e and θ_p are the electron and proton azimuthal angles with respect to the beam line, M is the proton mass. The results agreed with accurate measurements made in Hall A and Hall C, within 10 MeV. The results are presented in Table 7.1.

The estimated error is 5 MeV. These values correspond to the average value at the center of the target: the energy before entering the target is a few MeV higher due to ionization energy loss. The Technical Note about this correction, Ref. [46], provides full details on the procedure.

Table 7.1: Calibrated beam energies for eg1-dvcs

E_0 (GeV)	Part of Run
5.887	Part A (beginning)
4.730	Part A (end)
5.954	Part B
5.752	Part C

Chapter 8

Asymmetry

8.1 Double Spin Asymmetry

Each physics bin of the double-spin asymmetry A_{\parallel} is filled using:

$$A_{\parallel} = \frac{N_1 - N_2 r_c}{N_1 + N_2 r_c} \frac{c_s}{f (1 + c_1 + c_2) P_b P_t f_{RC}} + A_{RC} \quad (8.1)$$

where N_1 (N_2) are the number of counts in the anti-parallel (parallel) helicity bins, r_c is the ratio of incident beam charges for the two helicities, f is the bin-averaged dilution factor, defined as the ratio of events from polarized proton or deuterons in the NH_3 or ND_3 target to the total number of counts, c_s is the pair-symmetric correction, c_1 accounts for polarized nitrogen in the NH_3 and ND_3 targets, and c_2 accounts for the polarized NH_3 contaminating the ND_3 target. The radiative corrections, f_{RC} and A_{RC} , make adjustments for processes other than Born scattering. Each of these correction factors is discussed in the following sections.

8.2 Raw Asymmetry

The basic data processing consists of counting the number of electron events passing the particle ID cuts discussed in Section 7.4. The counts are accumulated for each run and then sorted in bins of momentum P , azimuthal scattering angle θ , and helicity. Helicity is divided in two bins, one for beam and target polarizations aligned and the other for anti-aligned. The main reason for choosing bins in (P, θ) at the data processing stage was to enable more intuitive checks on whether code and corrections were performing as expected. Data were also binned in (Q^2, W) for comparison with other colleagues' results.

The counts are saved into files, which are then summed for each target configuration for either in-bending or out-bending runs. As seen in Fig. 7.9, the rates are similar enough across the range of runs for Part C that no significant bias is introduced, especially taking into account the relatively small spread in the value of the double-spin asymmetry as a function of run number (see Fig. 7.10) [27].

A simulation showed that the small bias introduced by first summing counts, then forming asymmetries, is very well canceled if the same method is used for inclusive and elastic asymmetries [27].

The bin sizes were 0.04 GeV in momentum and 0.2 degree in θ , chosen to be small enough to allow redistribution into physics bins of (x, Q^2) and (W, Q^2) . During the re-distribution process, the average value of all relevant physics quantities is measured [27].

8.3 Beam and Target Polarization ($P_b P_t$)

For this inclusive analysis, because the asymmetry of interest is a double spin asymmetry, the target polarization (P_t) and beam polarization (P_b) come into play as a product. There is also a very small parity-violating correction which will be treated as a systematic error.

There are two ways to determine this product: P_b and P_t can be found individually or the product itself can be determined. P_b can be determined using Møller scattering measurements which were taken during the run period and P_t can be determined using NMR data. Alternatively, to find the product elastic (or quasi-elastic for the deuteron) scattering can be employed.

For proton runs, the relative systematic errors for measurements made with Møller runs and NMR readings are over 5%. The preferred method, then, is to use ep elastic scattering to calculate $P_b P_t$, because the error is of order 1% statistical, and $< 2\%$ systematic [27]. This was the procedure used for Parts A and B, which used only NH_3 targets, as well as the NH_3 runs from Part C.

For the ND_3 target, the kinematic region where there is the best sensitivity to ep quasi-elastic scattering is heavily contaminated by the 10% NH_3 contamination in the target discussed in Section 8.4.3. On the other hand, the direct deuteron polarization measurements using NMR are reasonably accurate, thanks to the “double peak” fitting method, which removes the sensitivity to the hard-to-measure thermal equilibrium signal. See Section 8.3.1 or Ref. [47] for a discussion of the process.

We therefore used the count-weighted product of target polarization from NMR and beam polarization from Møller measurements to obtain:

- Part C in-bending runs: deuteron $P_b P_t = 0.216 \pm 0.010$

- Part C out-bending runs: deuteron $P_b P_t = 0.236 \pm 0.010$

The error is based on an estimated systematic error of 3% in P_t and 4% in P_b .

Using these values as a constraint, we then fit the ep coincidence data in the region of small missing momentum, to obtain $P_b P_t = 0.50$ for the protons in the ND₃ target [48]. Section 8.3.2 gives a description of the process used to calculate this number.

8.3.1 Deuteron Target Calibration

Part C of the EG1-DVCS experiment primarily used a polarized deuteron target. The basic process of measuring the polarization of the target is described in Sec. 5.1.4. The following gives a more detailed description of the process used to calibrate the data from this experiment.

The Data There are about 80,000 NMR scan files from the part C run period. Each file contains one scan, with each scan having 400 points. These files are stored on the CUE system and are kept under version control with Subversion (svn). They can be accessed both on and off site via the JLab server cvs.jlab.org. Persons wishing to check out this data should get the location of the repository from the Polarized Target Group at JLab. The files consist of three columns: the first is the fraction of the scan frequency, ranging from -1 to 1, the second is the baseline scan which was being used when the scan was taken, and the third is the amplitude from the NMR scan.

Background Fit To determine both the area and the peak heights, the background from the NMR signal must be removed. To start with, the baseline signal included as the second column of each file is subtracted from the raw signal. This will not

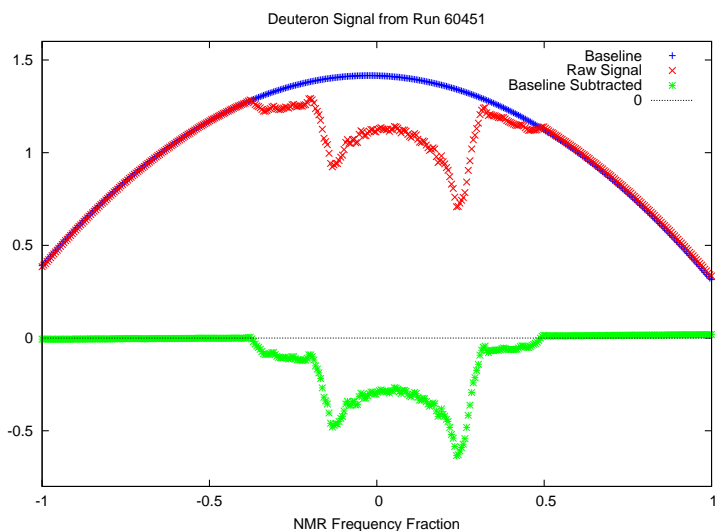


Figure 8.1: A deuteron signal from Run 60451 showing the raw signal, the baseline, and the resulting subtracted signal.

entirely remove all the background in most cases. A third-order polynomial can be fit to the baseline-subtracted signal [21] to remove background resulting from changes in the Q-curve. See Figure 8.1. Additionally, a number of signals exhibited a sinusoidal background signal, with a frequency of approximately 250 Hz, like that in Figure 8.2. Although the area of this sine wave should average out over a whole scan, if the peaks line up in a specific way it will change the value of the polarization as shown in Figure 8.3.

Sorting Each raw data file is named according to the following convention: YYYYMMDD.HH:MM:SS_ (“Top” or “Bottom”)(possibly including “.TE”).csv. “Top” or “Bottom” refers to the cup in the target stick which was being used when the scan was taken. All the deuteron scans for Part C are from the top cup, while any scans from the bottom cup are from protons. Files that include “.TE” were taken when a

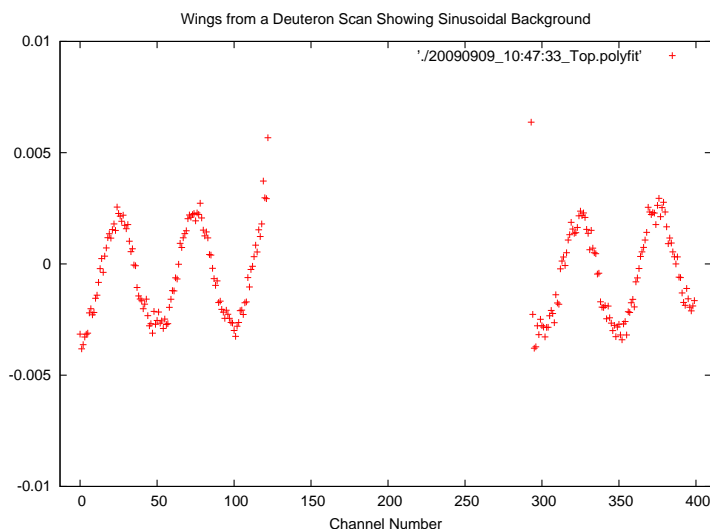


Figure 8.2: The sinusoidal background is much smaller in magnitude than the signal itself.

thermal equilibrium measurement was in progress.

In order to provide a polarization measurement for each run, the files must be sorted by Run Number. There is a script called “runSort.pl” which takes each file and moves it into a folder with the appropriate Run Number. The start and end times for each run must be specified in a file called “runTimes.txt”. I acquired the data in this file courtesy of Erin Seder. Because the NMR system scans even when there is no data being taken, a substantial number of files do not belong to a run and will remain unsorted.

Ratio Method As mentioned in Sec. , the ratio between the areas of the two components to the deuteron signal can be used to determine the polarization. To accurately find the areas, a function must be fit to the data and the ratio extracted from the fitting parameters. Chris Dulya [21] developed a program which takes a

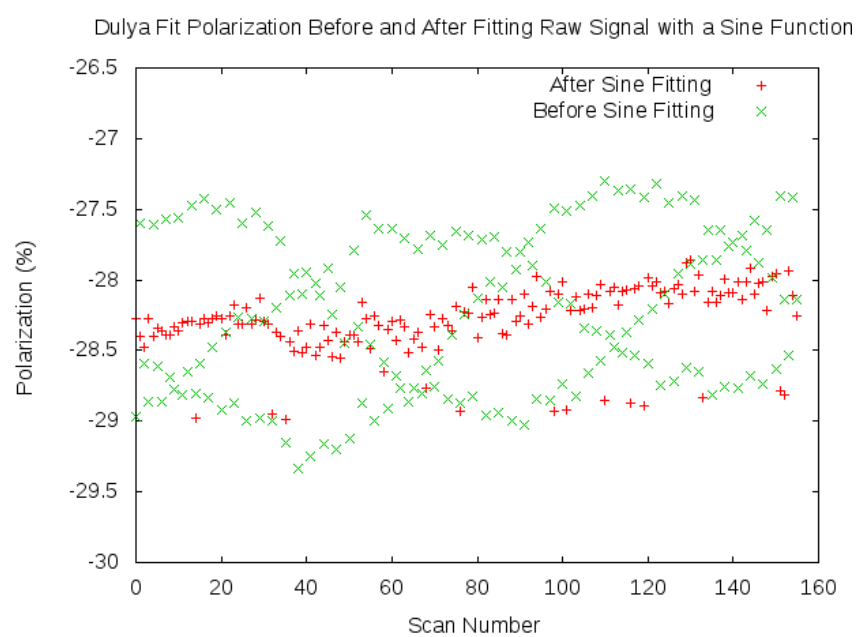


Figure 8.3: Graph shows all scans from Run 60478. Removal of the sinusoidal background greatly decreases the spread between points. The pattern in pre-removal polarizations is a result of the magnitude of the sine wave varying in time.

set of data points and fits a function describing the deuteron signal to it using a set of 12 parameters. One of these parameters is the ratio from which the polarization is derived. Unfortunately, the success of the fit is highly dependent on the initial parameters, so that one set of initial guesses will not allow the program to fit the entire data set. As illustrated by Figure 8.4, only some runs return reasonable results for each set of initial parameters. An appropriate set of initial values can be chosen for a scan through tedious trial and error. Parameters found in this way will typically be useful for a range of runs.

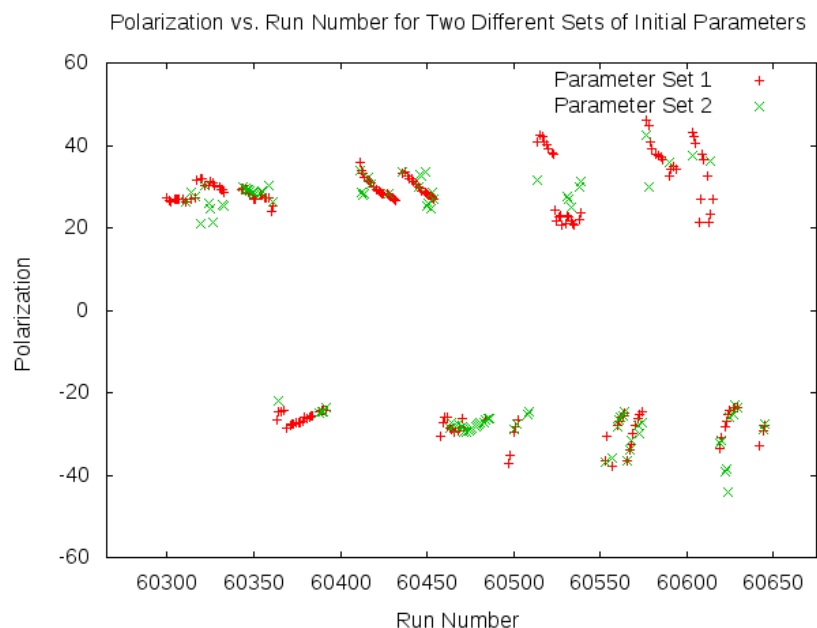


Figure 8.4: Graph shows polarizations for all runs as determined by fitting with Dulya's program. Two different sets of initial parameters are shown.

Calibration Constants The method of finding a Calibration Constant used for TE measurements can be adapted to the ratio method. The calibration constant represents the amount of polarization for each unit of area in one scan. Whereas the TE method relates a polarization that is determined from the temperature, magnetic

field, etc. to the signal area, the ratio method can provide a polarization based on the shape of the NMR scan. To find a calibration constant, a set of initial parameters was found that would give reasonable results for most of an entire run. After checking to be sure that the fitted line conformed well to the signal, cuts were applied to any points that did not fit the polarization trend for that run. Scans where the polarization was more than 5 standard deviations away from the average polarization for a run were excluded with these cuts. From this, the polarization of each scan was divided by the area of that scan to give a calibration constant. Any outliers in the calibration constant distribution are cut, and then the average of this calibration constant distribution becomes the calibration constant for a section of the data.

The data are divided into sections based on the condition of the target. Annealing, accumulated dose, or other changes to the target can affect the calibration constant. Any action which disturbs the arrangement of granules within the target cell will alter the calibration constant. During the run period, there was an event where high current pulsed beam was sent through the target which resulted in some settling of the ammonia granules. This is reflected in the relatively large change in calibration constant seen part way through the run period. Calibration constants were generated and applied as shown in Table 8.3.1.

8.3.2 Proton Contamination Polarization

The manufacturer's specifications for the material used to make the ND_3 granules was about 1% NH_3 . A check was made using *ep* elastic data and the actual contamination was, surprisingly, found to be an order of magnitude larger. The amount of proton contamination is corrected for in the dilution factor, and the discussion can be read in Section 8.4.3. The contamination will also polarize somewhat, which leads to a value

Beginning Run	End Run	Ratio Method Calibration Constant
60316	60361	-0.720247
60362	60392	-0.719535
60393	60454	-0.683744
60455	60509	-0.56567
60510	60539	-0.598247
60540	60574	-0.550721
60575	60615	-0.647120
60616	60648	-0.553632

Table 8.1: The calibration constants are applied in sections covering the range of runs.

of $P_b P_t$ specifically for these protons, the measurement of which is discussed here.

The process for finding $P_b P_t$ for the proton contamination begins essentially the same way as for finding $P_b P_t$ for purely proton targets, namely by finding the elastic asymmetry. In calculating the elastic asymmetry, an electron and a proton must both be identified in each event. Electrons were selected using similar particle ID cuts as those used for the inclusive analysis. Protons were identified using a ± 0.7 nanosecond cut on the difference in predicted and measured time between the electron and proton, determined using the SC system [27]. The cuts used to select ep elastic events were:

- missing energy less than $120 \text{ MeV}/c^2$
- missing longitudinal momentum less than $120 \text{ MeV}/c$
- missing transverse momentum less than $80 \text{ MeV}/c$
- $|W - M| < 0.08 \text{ GeV}/c^2$
- beam energy reconstructed from electron and proton azimuthal angles only agrees with nominal beam energy within 70 MeV .

The last cut was especially powerful in reducing the background from quasi-elastic events from nitrogen to about 3% [27]. This was determined by scaling the rates from the carbon target by the ratio of nuclear ($A > 1$) material thicknesses. After scaling, the rates were found to match closely outside the region of the E_0 cut. The sensitivity to cuts was checked by calculating $P_b P_t$ with varying values for the cuts. The results were found to be consistent within the expected errors.

The dilution-corrected double-spin asymmetry was formed in bins of Q^2 . Normally, $P_b P_t$ is then extracted by comparing the measured asymmetry to the expected asymmetry. However, even when elastic cuts are made, a significant fraction of events have scattered from deuterons. Knowing the percentage of deuterons and their polarization allows for the measured asymmetry to be corrected and the value of $P_b P_t$ for the proton to be found. Table 8.2 shows the results. The values found are reasonable; even though protons typically will polarize upwards of 90%, the polarizing microwave frequency will not be tuned exactly for protons, so the polarization will end up significantly lower than would be expected from a normal proton target.

	Case	$P_b P_t$
Part C (in-bending)		0.50 ± 0.04
Part C (out-bending)		0.51 ± 0.06

Table 8.2: The value of $P_b P_t$ for the 10.5% of NH_3 contaminating the ND_3 target.

8.4 Dilution Factor

Due to the composition and configuration of the target not every event that passes the “good event” cuts has actually scattered from a deuteron. Many electrons can also scatter from the liquid helium, the nitrogen atoms in the ammonia, or the windows of the target cell. A detailed description of the materials in the target which are

in the beamline can be found in Section 5.2 and Ref. [26]. Because these species are unpolarized, (or less polarized, in the case of N^{14}) events scattered from them all contribute to the denominator of the asymmetry, Eq. 8.1, which 'dilutes' the measured value for the asymmetry. In order to correct for this fact, a dilution factor must be calculated. The dilution factor, then, is defined to be the ratio of events scattered from the deuteron to the total number of detected events.

If the desired asymmetry is:

$$A_{undiluted} = \frac{n^{\uparrow} - n^{\downarrow}}{n^{\uparrow} + n^{\downarrow} - \text{background}} \quad (8.2)$$

and the dilution factor (DF) is:

$$DF = \frac{n^{\uparrow} + n^{\downarrow} - \text{background}}{n^{\uparrow} + n^{\downarrow}} \quad (8.3)$$

then it is clear that:

$$A_{undiluted} = \frac{n^{\uparrow} - n^{\downarrow}}{n^{\uparrow} + n^{\downarrow}} * \frac{n^{\uparrow} + n^{\downarrow}}{n^{\uparrow} + n^{\downarrow} - \text{background}} = A_{\text{experimental}}/DF \quad (8.4)$$

A molecule of deuterated ammonia, ND_3 , has a total of 20 nucleons. If the cross sections for scattering from protons and neutrons were the same and there were no other materials to scatter electrons, we would expect a dilution factor of 6/20. This gives a convenient upper limit on the dilution factor; there are, however, other scattering centers in the target, notably the helium and the foils that compose the target system. (see Chapter 5.2 for more details) The dilution factor can thusly be written as:

$$DF = \frac{n_D}{n_{He} + n_{Al} + n_K + n_{Ammonia}} \quad (8.5)$$

where the n 's are event rates, and the subscripts stand for Deuterons, Helium, Aluminum (from the vacuum window foils), Kapton (from the target window foils), and the total Ammonia molecule, respectively [15]. Each of these rates is proportional to the areal density and the cross section for that material, as shown in Eq. 8.6,

$$n_i \propto \tilde{\rho}_i \sigma_i \propto \rho_i l_i \sigma_i, \quad (8.6)$$

so both of these properties must be identified for each scattering material. The constant of proportionality is related to the detector acceptance; since each material is part of the same target they should have identical constants which will cancel out.

The areal density is the product of the density of the material and the length of that material that is exposed to beam. The values for the experiment are shown in Table 8.3. Since the entirety of the deuteron data was taken on one target load, there is only one length of Ammonia needed, though in general this length, known as the “packing fraction” must be determined for each target load. The length of the Helium depends solely on the target length and the Ammonia length, both of which can be determined from the data (see Section 8.4.2), and the length of the various foils was measured. The densities are standard values, easily found in the Particle Data Group’s materials reference [49], except for Ammonia, which has been measured experimentally[50].

Table 8.3: Material Properties Used for Calculation of Dilution Factor

Material	Density (g/cm ³)	Length (cm)	Radiation length X_0 ($\frac{\text{gm}}{\text{cm}^2}$)	Molar Mass ($\frac{\text{gm}}{\text{mol}}$)
NH ₃	0.867	l_A	40.80	17
ND ₃	1.007	l_A	50.93	20
Aluminum	2.700	0.0166	24.03	27
Carbon	2.193	0.398	42.66	12
Helium	0.145	$L - l_A$	94.26	4
Kapton	1.430	0.0066	40.54	382

The cross sections for each material were calculated using a model that includes radiative corrections. These radiated cross sections are generated by fitting to world data, as explained in [43], and a value is given for 1% of a radiation length and 2% of a radiation length. The cross section needed for the dilution factor is then linearly interpolated from these two points.

8.4.1 Target Length L (Length Between Banjo Windows)

The distance L between the aluminum banjo windows was measured to be 2.3 ± 0.3 cm at room temperature. The large uncertainty arises because the windows are thin and flexible and can bend towards or away from each other, depending on the internal pressure of the banjo. Additionally, when running, the windows are cooled to cryogenic temperatures which will introduce effects we are unable to directly measure.

We therefore relied primarily on data taken with the empty target and no helium bath. The two peaks in Fig. 8.5 are from the aluminum banjo windows, with the small inner shoulder coming from the much thinner Kapton foils. The peak separation from these measurements is 2.0 ± 0.1 cm.

A check was made by extracting L from measurements of the ratio of rates from empty and carbon targets, with and without helium present, and assuming a helium density of $0.145 \frac{\text{g}}{\text{cm}^3}$. This method is essentially the same as that used to calculate l_A and is discussed in greater depth in Sec. 8.4.2. Using this method gave us a large range of values as shown in Figure 8.6. The average over the range of runs for parts A and B was $L = 2.17$ cm with a standard deviation of $\sigma_L = 0.244$ and the average for Part C was 2.04 cm. We concluded that it was more reliable to use the fit to the two peaks for the Aluminum windows as described earlier, so this procedure was then used as a consistency check for L .

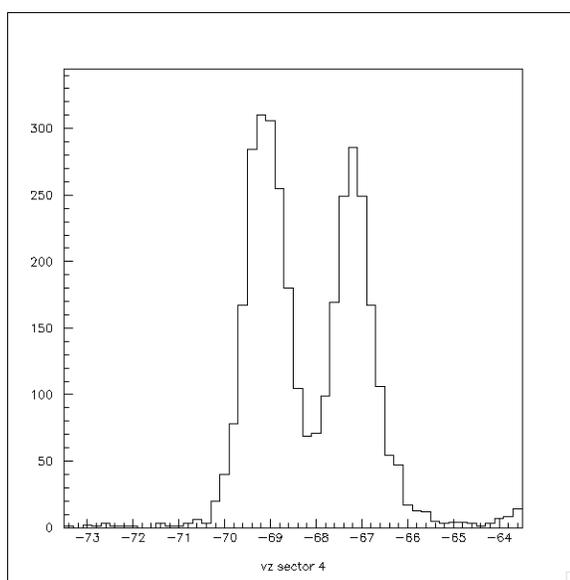


Figure 8.5: Data from an empty run with no helium bath. L is calculated from the distance between these two peaks.

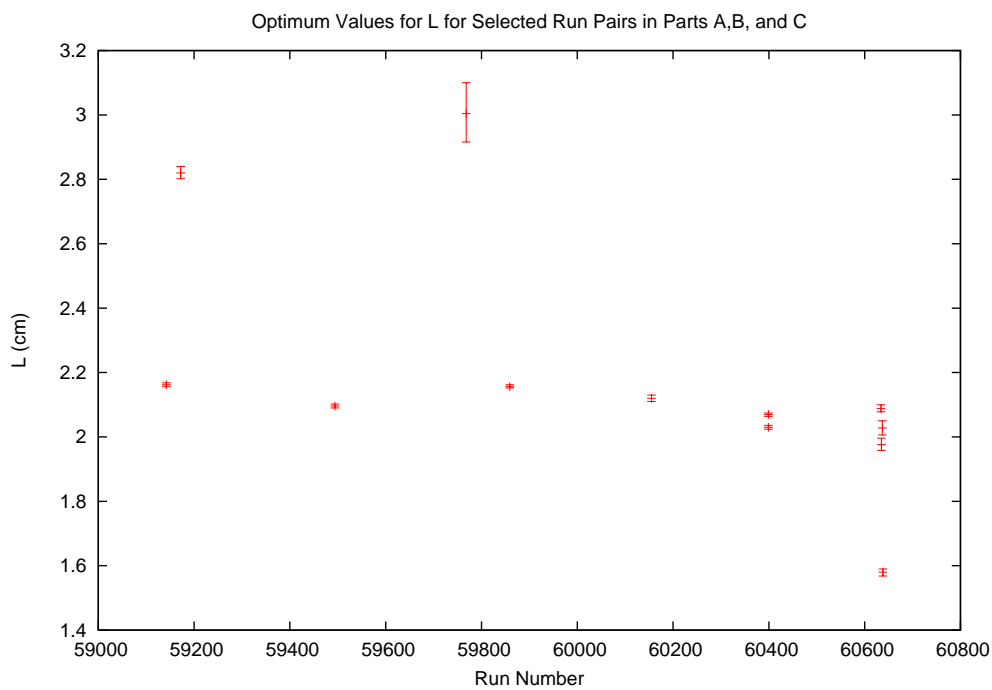


Figure 8.6: L calculated over a range of the run periods using different pairs of carbon and empty runs.

8.4.2 Ammonia Length l_A (Packing Fraction)

An important part of determining the dilution factor is knowing how much ammonia is actually contained in a target cell. This quantity, also known as the “packing fraction”, can be thought of as the length the ammonia would be if it was a solid piece instead of numerous small granules submersed in liquid helium. This, together with the length of the target, are also related to the amount of Helium which is exposed to the beam.

The method for determining l_A involves comparing the ratios of event rates for two different types of target, shown in Eq. 8.7.

$$\frac{n_{Empty}}{n_{Carbon}} \quad \frac{n_{Empty}}{n_{noHe}} \quad \frac{n_{Carbon}}{n_{Carbon}} \quad (8.7)$$

Ratios are using in order to cancel out systematic effects. These ratios, obtained from data, are then compared to theoretical ratios obtained using the example of Equation 8.9. The predictions used fits to world data while taking into account radiative effects; Ref. [43] has more details about the radiative cross-section models.

To find L , these rates are used to calculate χ^2 where

$$\chi_{DoF}^2 = \frac{\sum_i^{bins} (\frac{r_{exp} - r_{model}}{\Delta_r})^2}{N_{bins} - N_{parameters}} \quad (8.8)$$

The value of L is varied in order to minimize χ_{DoF}^2 ; the minimum value of the resulting curve is taken to be the optimum value for L and the error is the range of data that have a raw χ^2 that is 1 unit above the minimum, where the raw χ^2 is the χ_{DoF}^2 before it is divided by the (number of degrees of freedom-1). An example of the curve resulting from this process is shown in Fig. 8.7

$$DF = \frac{\frac{3}{17}\rho_A l_A \sigma_A}{\rho_{He}(L - l_A)\sigma_{He} + (\frac{14}{17}\sigma_N + \frac{3}{17}\sigma_p)\rho_A l_A + \rho_{Al} l_{Al} \sigma_{Al} + \rho_K l_K \sigma_K} \quad (8.9)$$

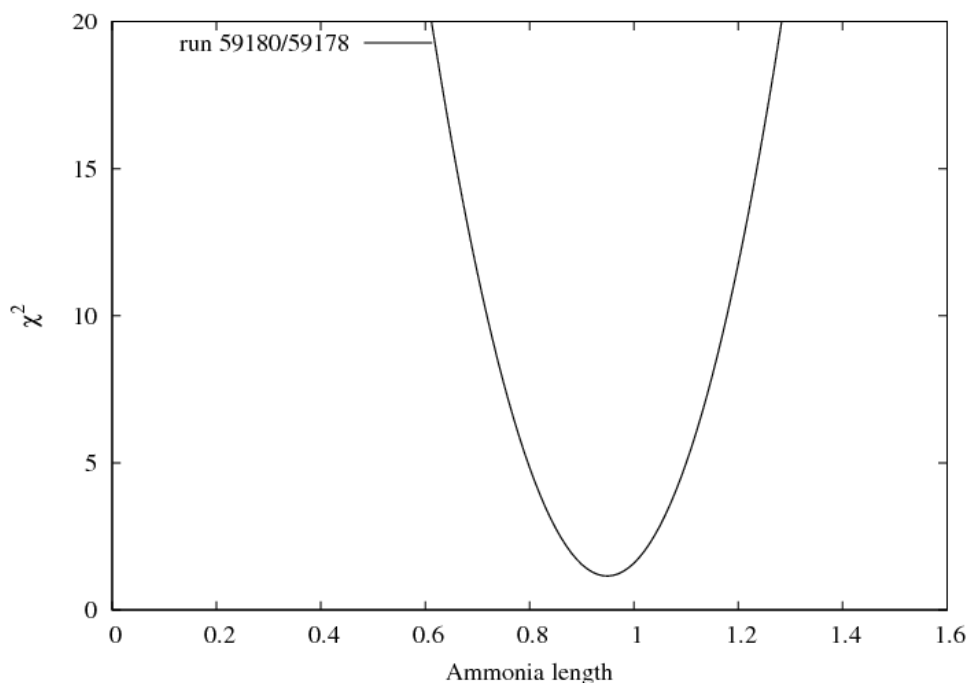


Figure 8.7: A χ_{DoF}^2 curve obtained by varying the target length L for a pair of runs in Part A [15]. The value of L is at the minimum of this curve.

Figures 8.8 and 8.9 shows the values obtained over the range of the run period. Values are shown for all of the separate targets, including the Top and Bottom cups for Parts A and B and Part C. The ammonia granules were changed after run number 59300 thus the packing fraction changed here.

A summary of the data is presented in Table 8.4.

8.4.2.1 Raster Correction to the Effective Length of ND_3

At the beginning of Part C, the ND_3 target cell was entirely filled with granules. During a beam-tuning procedure, the target received a dose of “pulsed” beam with

	Run Range	Target Cup	L (cm)	l_A (cm)	l_A Error (cm)
Part A	(58799 - 59300)	Top	2.1	0.853	± 0.0024
Part A	(58799 - 59300)	Bottom	2.1	0.851	± 0.0014
Part B	(59300 - 60185)	Top	2.01	0.860	± 0.001
Part B	(59300 - 60185)	Bottom	2.01	0.910	± 0.001
Part C	(60242 - 60645)	Top	2.05	0.922	± 0.001
Part C	(60242 - 60645)	ND3	2.05	0.890	± 0.001

Table 8.4: A summary of target length and ammonia length data for all parts.

high peak current. After this event, investigation of the raster pattern revealed that there was a gap with no granules near the top of the cell that was several millimeters high. It appears that some of the granules were broken up into smaller pieces and subsequently settled within the cell. To compensate, the magnitude of the vertical raster was decreased, changing the raster pattern from round to elliptical, and re-centered to minimize the amount of beam that was not encountering ammonia. For a period of time, the raster scan drifted too high and the event rate dropped as a result of hitting only liquid helium. This is illustrated in Fig. 8.10, where the rate of good electrons is plotted versus the average vertical raster magnet ADC reading. A correction function, representing the effective decrease in target thickness, was developed by parameterizing the data in terms of average magnet current Y_r . This equation, given by Eq. 8.10, is shown on the figure as a dashed line. The correction is only applied for $Y_r > 3800$. [27]

$$Correction = 1 + \frac{140}{2150} \frac{(Y_r - 3800)}{400} \quad (8.10)$$

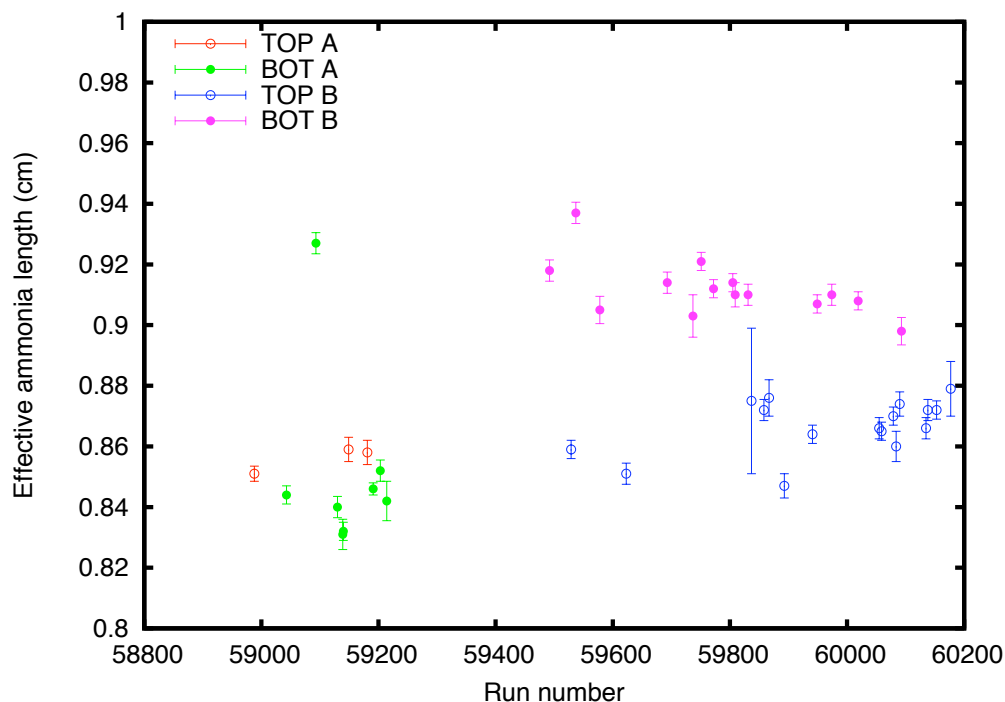


Figure 8.8: l_A calculated over a range of runs from parts A and B using different pairs of carbon and ammonia runs. Selections from both top and bottom cup from each part are shown. [15]

8.4.3 Scattering Measurement of Hydrogen Contamination in ND_3

The manufacturer's specifications for the material used to make the ND_3 granules was about 1% NH_3 . A check was made using *ep* elastic data and the actual contamination was, surprisingly, found to be an order of magnitude larger. After standard *ep* elastic exclusivity cuts, the events from hydrogen, deuterium, and heavier nuclei could clearly be distinguished; due to the Fermi motion of the nucleons, the momentum distribution for each species becomes increasingly broad. Spectra for carbon, NH_3 , and ND_3 targets are given in Figure 8.11. [51] The polarization of this contamination is discussed in Sec. 8.3.2

The best sensitivity was found by using the correlation between polar scattering

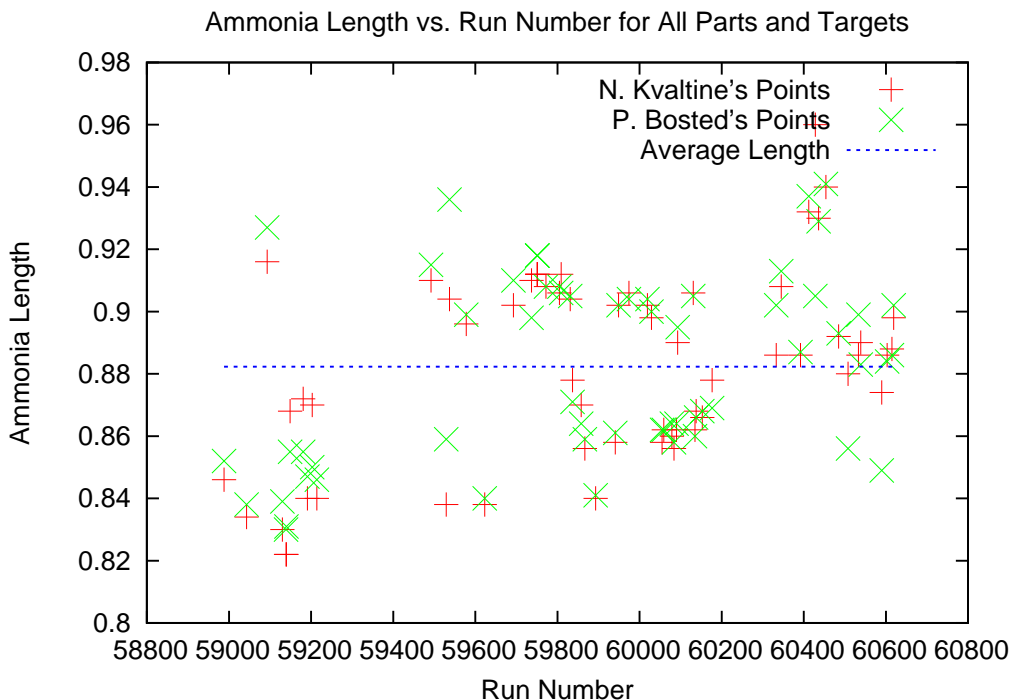


Figure 8.9: l_A calculated over a range of runs from Part C using different pairs of carbon and ammonia runs. Only deuterated ammonia runs are shown. Points in red were calculated by the author while points in green were calculated by P. Bosted; there is generally good agreement between the two.

angles for the scattered electron and detected proton. This is because angles are measured more precisely in CLAS than momenta. The polar angular resolution is better than the azimuthal resolution due to the large ϕ rotations from the polarized target magnetic field as well as the inherent resolution of the drift chambers.

Two alternative methods of utilizing the polar resolution were used; one reconstructs the beam energy using the measured proton angle and the other reconstructs the proton angle using the known beam energy. Both methods give contamination fractions that agree reasonably well and the process for obtaining the contamination fraction for either method is similar so only the general process will be discussed. For full details see Ref. [48] and Ref. [51].

Nuclear contributions must be subtracted, so Faraday-Cup-normalized data com-

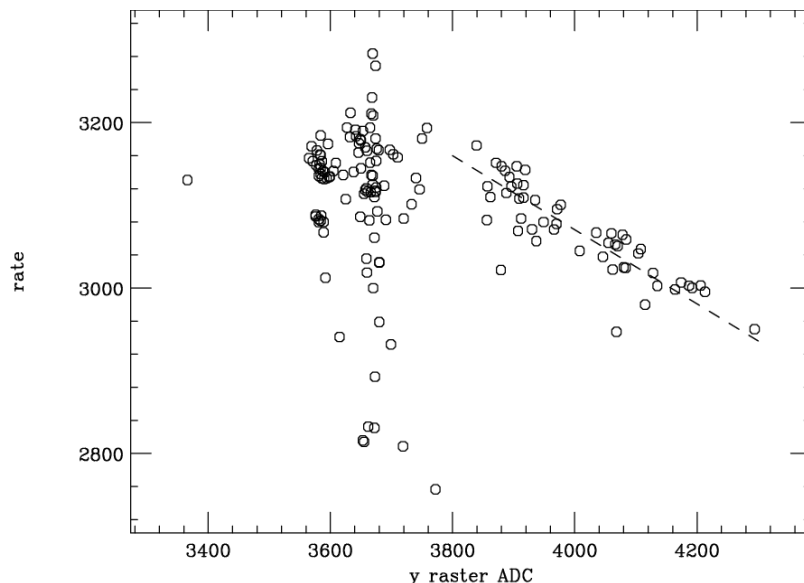


Figure 8.10: Rate of detected electrons from the ND_3 target in Part C (inbending runs only) as a function of the average vertical raster magnet reading [27].

ing from the Carbon target is subtracted from both NH_3 and ND_3 spectra, which must also be normalized. The signal resulting from this subtraction is then composed of NH_3 and ND_3 elastic and quasi-elastic peaks. With the beam-energy method [48], the NH_3 peak was scaled by a factor C to match the proton peak seen in the ND_3 spectra. This scaled peak was subtracted from the ND_3 spectra in order to verify that the proton events were removed. Upon proper selection of the scale factor, it can be interpreted as the fraction of proton events in the ND_3 spectra, and thus as the contamination fraction. The distributions for the energy reconstruction method are shown in Fig. 8.12 with cuts given in Table 8.5.

Cut number	E_{miss} (GeV)	Pz_{miss} (GeV)	Pt_{miss} (GeV)
1	0.20	0.20	0.16
2	0.10	0.10	0.07
3	0.05	0.05	0.04
4	0.03	0.03	0.02

Table 8.5: Values of the cuts on missing energy and momentum for ep coincidences used for each of the cut numbers.

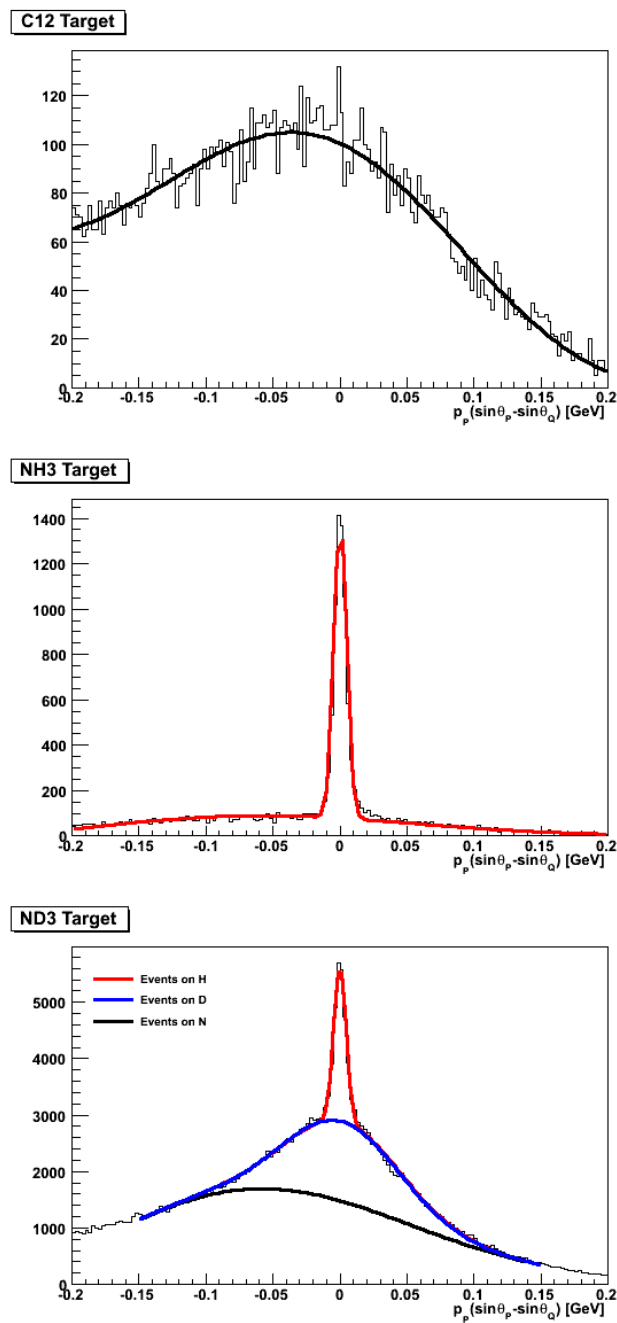


Figure 8.11: Elastic rates, plotted versus the polar component of the fermi-momentum, are shown for three different targets, carbon, NH_3 , and ND_3 . Figure from S. Koirala.

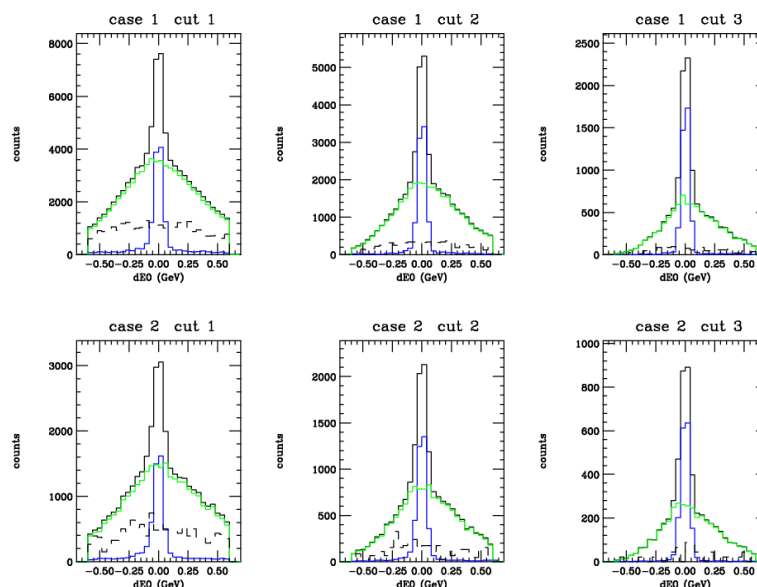


Figure 8.12: Distributions using cuts from Table 8.5 plotted against difference between nominal and reconstructed beam energy. [48]

The result of the study was that $10.5 \pm 0.04\%$ of the ND_3 effective target length was hydrogenic, stemming from NH_3 , NDH_2 , or ND_2H , for the inbending runs, and $12.0 \pm 0.7\%$ for the outbending runs. The hydrogenic contamination is suspected to be due to contact between water and the ammonia, since deuterated ammonia will readily exchange deuterium for hydrogen with water. Since water is always present in the air, and can condense from the atmosphere when presented with the temperatures used for ammonia handling, there are a number of opportunities for the sample to be contaminated.

8.4.4 NMR Measurement of Hydrogen Contamination in ND_3

In a polarized target experiment, one of the main factors for finding the physics asymmetry is the target polarization, so it is important to have an accurate measurement of this number. As discussed previously, using elastic and quasi-elastic scattering data it was found that the deuterated ammonia target used in Part C had a substantial

hydrogen contamination[48, 51]; the nominal hydrogen contamination for purchased ND_3 gas is about 1%, while the contamination in the target, found from scattering, was about 10.5%. As a check on this measurement, a direct chemical assay of the target material was requested. It was determined that mass spectrometry would be unsuitable for several reasons, e.g. the reactive nature of ammonia or the difficulty of using cryogenic materials in the apparatus. A method using nuclear magnetic resonance (NMR) was devised which would allow for a measurement despite these shortcomings. The NMR measurement requires the ammonia granules be dissolved in deuterated water infused with a known concentration of a hydrogenic marker. The procedure will be discussed in detail in Sec. 8.4.4.

Target Material Background As discussed in Sec. 5.3, the process for making ammonia target material is complicated. A recap is provided here, to provide background on the suspected cause of the contamination.

The ammonia used for the target material is purchased in a standard gas cylinder. To form it into the frozen granules used for physics targets, a custom apparatus is used to freeze the gas into a small cylindrical chunk using liquid nitrogen. This chunk is then crushed and graded in order to select the desired size of granules. In order for the ammonia to stay frozen, the crushing and grading must be done under liquid nitrogen. Once frozen and crushed, the ammonia must also undergo an irradiating procedure under liquid argon in order for the polarization mechanism to function. The multiple handlings required to create this material and the propensity for ammonia to exchange a proton for a deuteron when exposed to water expose it to contamination by hydrogenic materials. There also exists the possibility of contamination by granules of entirely hydrogenated ammonia which were used during the same runs in different target cups.

Procedure A full description of NMR techniques is beyond the scope of this document, but the salient feature is that it will give a measurement that is proportional to the number of atoms of a particular isotope in a sample. Due to the nature of the NMR machine, the sample must be in a liquid state; deuterium oxide (heavy water) was the solvent of choice for this experiment. Additionally, a chemical marker is needed to determine the constant of proportionality. Acetonitrile was used because of its solubility in water and its resistance to exchanging protons for deuterons in the sample or solvent. Finally, measurements must be made with only solvent and marker in order to determine the amount of hydrogen already present in the deuterium oxide.

Sample Preparation The basic procedure for preparing samples for an NMR measurement is as follows:

- Weigh one empty 15 mL sample vial and then one 1 mL sample vial for each sample to be measured. Usually 3 samples were measured in one session.
- Add 10 mL of D₂O to 15 mL sample vial and weigh.
- Add 52 μ L CH₃CN to 15 mL sample vial and weigh. This will be referred to as the “standard solution” from now on.
- Add 1 mL of the standard solution to each small sample vial and weigh.
- Set up a glove box containing the ammonia to be used for the samples (in liquid nitrogen, of course), the 1 mL vials of standard solution, and the appropriate tools for manipulating frozen granules of ammonia.
- Pump out the glove box and purge it with dry nitrogen 3 times.
- Drop two granules of ammonia into each 1 mL sample of standard solution and close lids. These will be called sample solutions from now on.

- Weigh sample solutions.
- Transfer sample solution to sealable NMR probes. Also transfer 1 mL of remaining standard solution to an NMR probe.

Measurements The NMR pulse sequence is important in order to get an accurate reading. The pulse width that was used was 22.2 ms with an acquisition time of 3.1 ms. An inter-pulse delay of 100 seconds was used so that the relaxation time would be long enough and each measurement was an average of 4 pulses. Generally, each sample was subjected to two measurements, as time allowed.

Analysis The output from a measurement is a graph like that shown in Fig. 8.13. Each peak represents the number of atoms of hydrogen from a particular chemical; in this case the acetonitrile marker's hydrogen comes in at around -5 ppm, while the peak around -2 ppm stems from the contamination of the heavy water and ammonia.

The area of a peak, A_{peak} , is given by:

$$A_{peak} = CC \frac{\text{molH}}{L_{soln}} L_{exp} \quad (8.11)$$

where CC is a calibration constant, molH is the number of moles of hydrogen atoms, L_{soln} is the volume of the solution, and L_{exp} is the volume of sample that is measured experimentally. This volume is related to the size of the uniform field region for the particular NMR magnet and is not known; fortunately it will cancel in the following calculations.

The acetonitrile marker allows us to find the calibration constant. Using Eq. 8.11 we see that:

$$CC = \frac{A_{mark} L_{soln1}}{\text{molH}_{mark} L_{exp}} \quad (8.12)$$

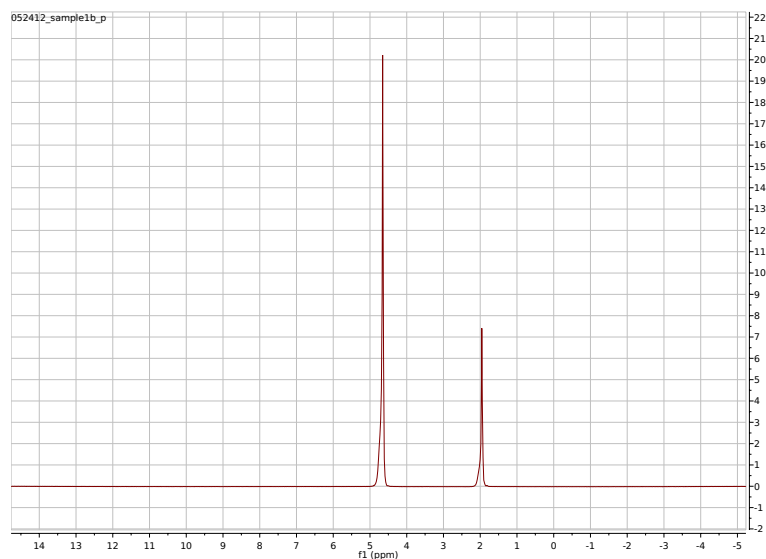


Figure 8.13: A typical NMR scan. The x-axis is frequency, given in parts per million shift from the Larmor Frequency for Hydrogen. The y-axis is an arbitrary magnitude. The larger peak on the left corresponds to the hydrogen in the acetonitrile marker, while the smaller peak on the right corresponds to the hydrogen from the heavy water and the sample combined.

where the various constants are relabeled to reference the marker solution. $molH_{mark}$ can be rewritten as $\frac{3g_{mark}}{41.05 \frac{g}{mol}}$ where g_{mark} is the mass of acetonitrile, and the 3 comes from the 3 hydrogens per acetonitrile molecule.

The area of the other peak for the sample solutions, using Eq. 8.11, is:

$$A_H = CC \left(\frac{molH_{D_2O}}{L_{soln1}} + \frac{molH_{ND_3}}{L_{soln2}} \right) \quad (8.13)$$

and for the standard solution:

$$A_H = CC \left(\frac{molH_{D_2O}}{L_{soln1}} \right) \quad (8.14)$$

The number of moles of hydrogen in the ND_3 can be written as:

$$3 \frac{g_{\text{ND}_3}}{20 \frac{\text{g}}{\text{mol}}} \text{cont}F \quad (8.15)$$

where the 3 comes from the number of deuterons per ammonia molecule, 20 is the molecular weight of deuterated ammonia, and $\text{cont}F$ is the contamination fraction.

Using Eq. 8.14 and the measurement done on the standard solution, along with Eq. 8.13 and the weights measured during sample preparation, the contamination percentage can be measured. Putting everything together and solving for contamination percentage:

$$\text{cont}F = \left(\frac{A_H}{A_{\text{mark}}} - \frac{A_{H_{D20}}}{A_{\text{mark}}} \right) \left(\frac{20}{41.05} \right) \left(\frac{g_{\text{mark}}}{g_{\text{ND}_3}} \right) \left(\frac{g_{\text{soln}2}}{g_{\text{soln}1}} \right) \left(\frac{\rho_{\text{soln}1}}{\rho_{\text{soln}2}} \right) \quad (8.16)$$

In getting this equation, $\frac{L_{\text{soln}2}}{L_{\text{soln}1}}$ is changed to $\left(\frac{g_{\text{soln}2}}{g_{\text{soln}1}} \right) \left(\frac{\rho_{\text{soln}1}}{\rho_{\text{soln}2}} \right)$. In general, the weights are measured more precisely than the volumes and the ratio of densities is approximately one, so this formulation gives a lower error.

Error There are a few explicit errors in the contamination fraction as written in Eq. 8.16. First, the densities of the two solutions are not measured, and their ratio is approximated as 1. The error due to this is small because the densities are quite similar, which results from the small amount of solute used. Second, although 20 is given as the molar mass of deuterated ammonia, the hydrogenous contamination being measured means that the actual molar mass will be slightly lower. With a 10% contamination the correction due to this is about 1.5%.

The measurement errors that are present result from the mass and the areas of the peaks. In practice, peak heights were used instead of areas, but the heights correlate quite closely to the areas and all peak measurements appear as ratios. The

heights appear to be consistent to within 1.5% for repeated measurements made on the same sample. Mass measurements were made with a digital balance that was precise to the hundred-thousandth of a gram. The smallest mass was that of the added granules and was generally around 20 milligrams. At worst case, each mass adds about half a percent of error.

Overall, these identified sources of error combine to about 4%. Unfortunately, the range of results that presented was much more variable than that.

Results The contamination percentages for the deuterated material varied wildly from sample to sample. Values are shown in Table 8.6. Additionally, there was a set of measurements that were invalidated due to the hydrogen peak being higher in the standard solution than in the sample solutions. The wide variability of measurements implies that there is some additional source of error. There was already some speculation that the contamination was not equally spread throughout the granules. For most of the measurements this is a plausible explanation, however there is a measurement that shows greater than 100% contamination. This, along with the sample with more Hydrogen in the standard solution, implies that there is some additional contamination occurring during the sample preparation phase.

A set of measurements was made using ammonia that was purely hydrogenated. The results are shown in Table 8.7. The range in these measurements was also quite large, given that the “contamination” in this case should be 100%.

40.4%	121.5%	6.4%	14.6%	15.7%	2.3%	4.2%	0.9%	1.1%	1.2%
-------	--------	------	-------	-------	------	------	------	------	------

Table 8.6: The various measured values of contamination percentage from samples of deuterated ammonia from egl-dvcs Part C.

The variability of these measurements means that this method does not provide

72.2%	80.7%	85.3%
-------	-------	-------

Table 8.7: The measured values of “contamination percentage” from purely hydrogenous ammonia, i.e. NH_3 . The expected result for this case is 100%, which implies further experimental refinement would be necessary for an accurate measurement.

a meaningful check on the contamination percentage. The limited supply of material from the experiment precludes using more granules as an attempt to reduce the error from introduced contamination and would also obscure the possibility of determining if there was a significant granule-to-granule difference in contamination levels.

8.4.5 Results

Using the method and corrections outlined above, we calculate the dilution factor for each target, beam, and position configuration. Examples are shown below for the proton target in the top position of Part A of the experiment and for the deuteron target from Part C.

8.5 Pion and Pair-Symmetric Correction

Another correction to the asymmetry stems from particles that are mistakenly identified as the scattered electron. The two main sources of these particles are negative pions and electrons that were produced in pair-production processes. The correction for this contamination is of the form:

$$A_{corr} = A_{raw} \frac{1 - \sum_i R_i A_i}{1 - \sum_i R_i} \quad (8.17)$$

where R_i is the ratio of rates for a particular process to the electron rate and A_i is the ratio of the asymmetry for the process to the electron asymmetry[52].

Dalitz decay of the π^0 , which results in a photon and an electron-positron pair,

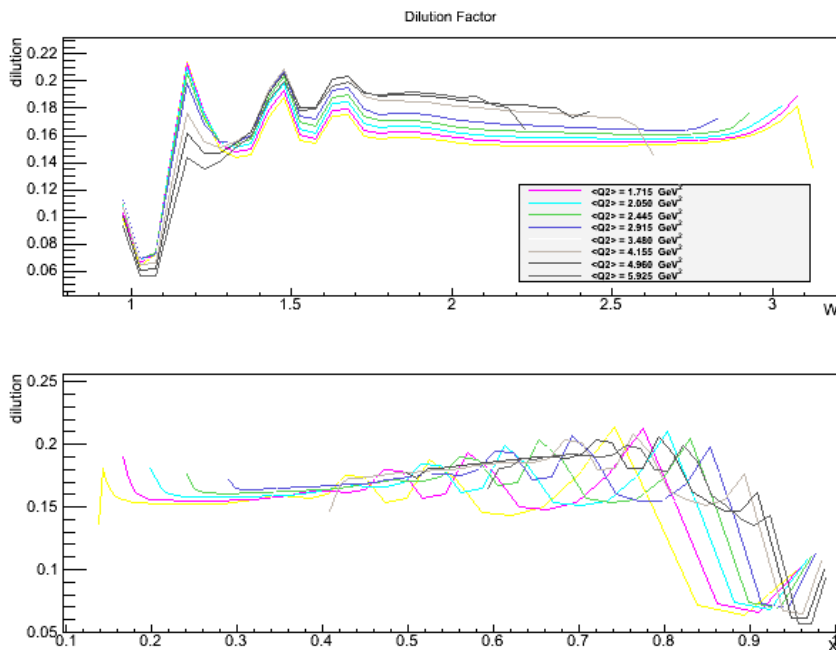


Figure 8.14: Dilution factor for the proton target as a function of W (GeV) and Q^2 on top figure, and as a function of Bjorken x on the bottom figure. [27]

occurs for about 1.2% of π^0 decay[53]. Bethe-Heitler processes will also produce electron-positron pairs where the electron can be mistaken for an inclusively scattered electron. Since the number of electrons and positrons created by these processes is equal (hence the name “pair-symmetric”), the number of positrons can be used to find the number of electrons if the acceptances are the same. Since electrons and positrons are essentially but with opposite charges, runs with opposite torus polarities are used in order to balance the acceptance. About 50 runs from each of the inbending and outbending sections of data were taken and analyzed with the standard electron cuts to count electrons, and with the electron cuts with charge equal to positive one to count positrons. The results, binned in momentum and azimuthal angle (p, θ) , are shown in Figure 8.16.

The ratios of e^+/e^- are compared with two predictions in Fig. 8.16. The black

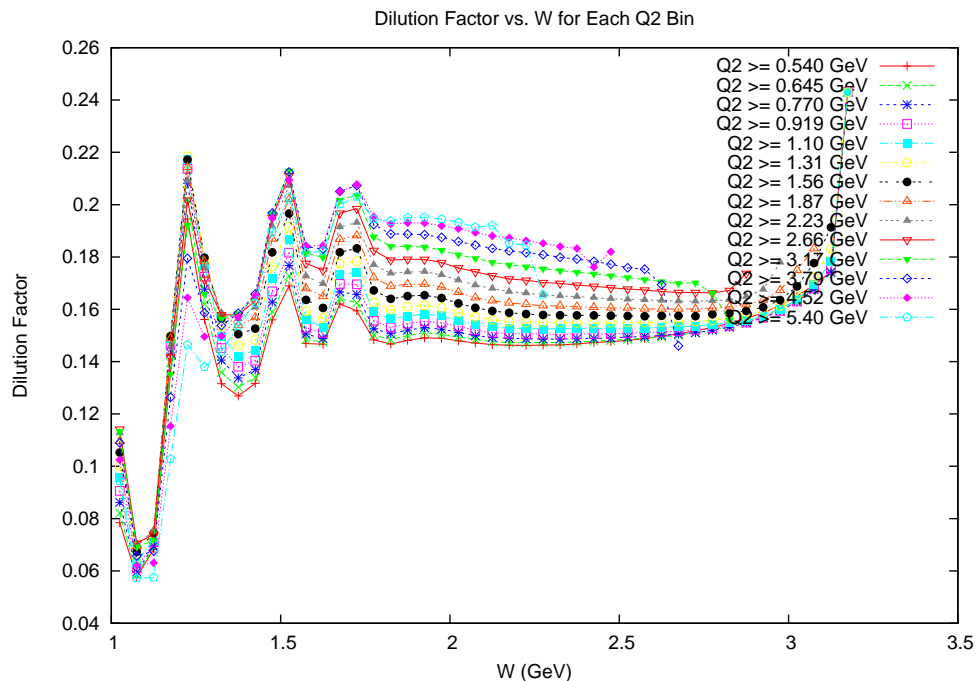


Figure 8.15: Dilution factor for the deuteron target as a function of W , with separate curves for each Q^2 bin.

curves are the predicted ratios assuming that all the positive particles are actually positrons and not mis-identified pions. As discussed in Ref. [52], the only significant source of positrons for $\theta > 16$ degrees and a beam energy of 6 GeV is from π^0 decays. This includes both the Dalitz decay into $\gamma e^+ / e^-$ which has a branching ratio of 1.2%, and the normal decay to $\gamma\gamma$ where one of the photon converts to e^+ / e^- in the field of one of the nuclei in the target, target windows, air between the windows and the first drift chamber (DC1), or in DC1 itself. The cross section for inclusive π^0 yields was taken as the average of yields for π^+ and π^- , measured at both 5 and 7 GeV electron beams at SLAC [54]. A simple Monte-Carlo generator taking into account our target configuration performed the π^0 generation and decays and calculated the cross sections in bins of spectrometer P and θ [27]. These were divided by the well-known inclusive electron cross section to obtain the ratios shown as the black curves. Good

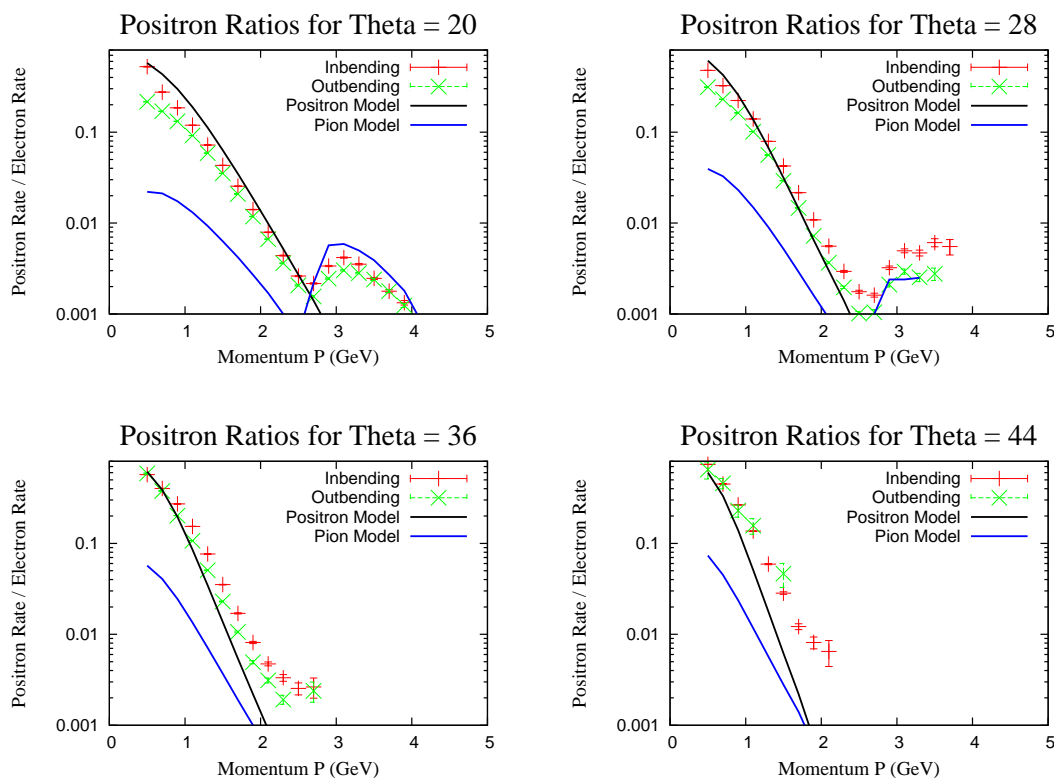


Figure 8.16: Positron to electron ratio plotted against momentum. Theta has been summed over ± 4 degrees, with the center value shown.

agreement is found in both shape and magnitude up to about 2.6 GeV, considering the approximately 30% uncertainty in the calculation.

The clear excess of positrons above 2.6 GeV can be attributed to detected π^+ passing the positron selection criteria. The expected rate, shown as the blue curves in Fig. 8.16, was modeled using the fit to SLAC data mentioned above to calculate the pion cross sections. The pion rate was reduced everywhere by a factor of ten to simulate the approximate rejection power of the E/P cut[27]. The Cherenkov detection efficiency (relative to that of an electron) was considered as 100% above 3.6 GeV, dropping to only 1% at the pion threshold of 2.65 GeV. The 1% value stems from a rough estimate of the pion colliding with an atomic electron in the Cherenkov window or gas medium and the “knocked-out” electron being well above the few-

MeV-threshold to emit Cherenkov radiation [27]. The simulation accounts quite well for the enhancement seen above 2.65 GeV, and also strongly suggests that positrons dominate over pions at lower momenta.

The other factor in determining the correction is the ratio of the electron and positron asymmetries. Figure 8.17 shows that the positron asymmetry is consistent with zero. Although the IC restricts a large amount of the lower angle particles which results in a limited W range for positrons, the positron asymmetry in the W range where there are good statistics is quite small.

8.6 Contribution from Polarized Nitrogen (c_1)

Incoming electrons can also scatter off of the nitrogen atom in the ammonia molecule and if the nitrogen is polarized this can contribute to the measured asymmetry. To remove this effect, the c_1 term in Eq. 8.1 accounts for the contribution of the polarized nitrogen to the double spin asymmetry. If the raw asymmetry is defined in terms of the physics asymmetries for each polarizable nucleus in the target, it can be shown that

$$c_1 = \left(\frac{\eta_N}{\eta_d}\right)\left(\frac{A_N\sigma_N}{A_d\sigma_d}\right)\left(\frac{P_N}{P_d}\right) \quad (8.18)$$

where η is the number of nuclei of a given species, σ is the cross section per nucleus, A is the double-spin asymmetry (hence $A\sigma$ is the cross section difference), and P is the polarization of a given species[55]. For each of these four variables, the subscript N is for nitrogen-14 and d is for the deuteron in the ND_3 target. The first term (η_N/η_d) in Eq. 8.18 is 1/3 because there are three deuterons and one nitrogen atom for each ammonia molecule.

In the nuclear shell model, the spin-1 nitrogen-14 nucleus can be considered as a

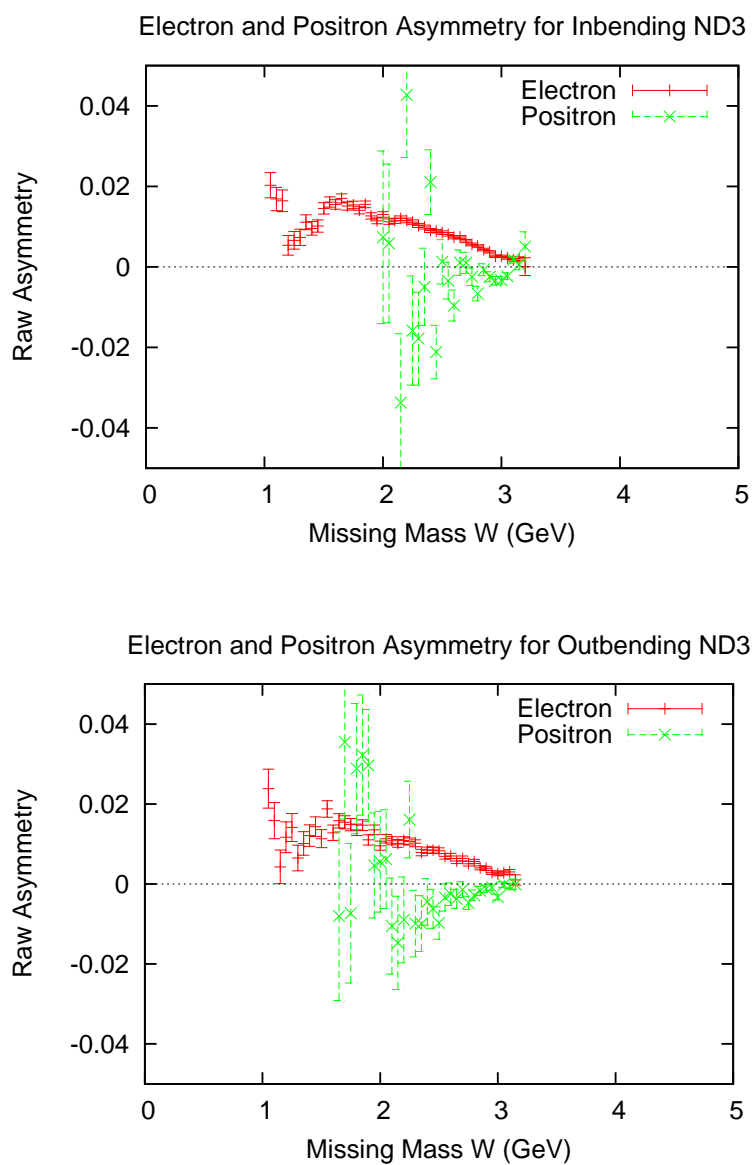


Figure 8.17: Positron and electron raw asymmetries, averaged over Q2.

spinless carbon nucleus surrounded by an extra proton and neutron, each in a $1p_{\frac{1}{2}}$ orbital state [56]. After doing the spin projections, it turns out that the proton and neutron are each twice as likely to have their spin anti-aligned with the nitrogen spin as having it aligned. It then follows that the second term in Eq. 8.18 can be evaluated using

$$A_N\sigma_N = -\frac{1}{3}(\sigma_p A_p + \sigma_n A_n) = -\frac{1}{3}\sigma_d A_d \quad (8.19)$$

where the subscript n refers to the neutron, and we have neglected the small d-state correction and used the relation $\sigma_d = \sigma_p + \sigma_n$ [19]. Inserting this into the second term of Eq. 8.18, we obtain a constant value of -0.33 ± 0.08 . The uncertainty of 0.08 comes from an evaluation [19] of a range of more sophisticated treatments of the nitrogen wave function than the simple shell model.

The third term, the ratio of nitrogen to deuteron polarization, can be evaluated using the Equal Spin Temperature (EST) theory [18, 19]. The EST theory posits that the electron spins are in thermal contact with the nuclear spins, leading to an equal spin temperature for all spins. The polarizations are not equal due to differing magnetic moments, but are correlated. For deuterated ammonia, the EST theory predicts $P_N/P_d = 0.48$, essentially independent of P_d [19]. An experimental study at SLAC (E143 experiment, unpublished) conducted using $N^{15}D_3$, which is spin- $\frac{1}{2}$, yielded a much lower value of $P_N/P_d = 0.33$. We therefore used an average: $P_N/P_d = 0.40 \pm 0.08$ [55].

Combining all these results together yields a value of c_1 for the deuteron that is independent of cross sections for either deuterons or protons:

$$c_1^d = -0.044 \pm 0.014 \quad (8.20)$$

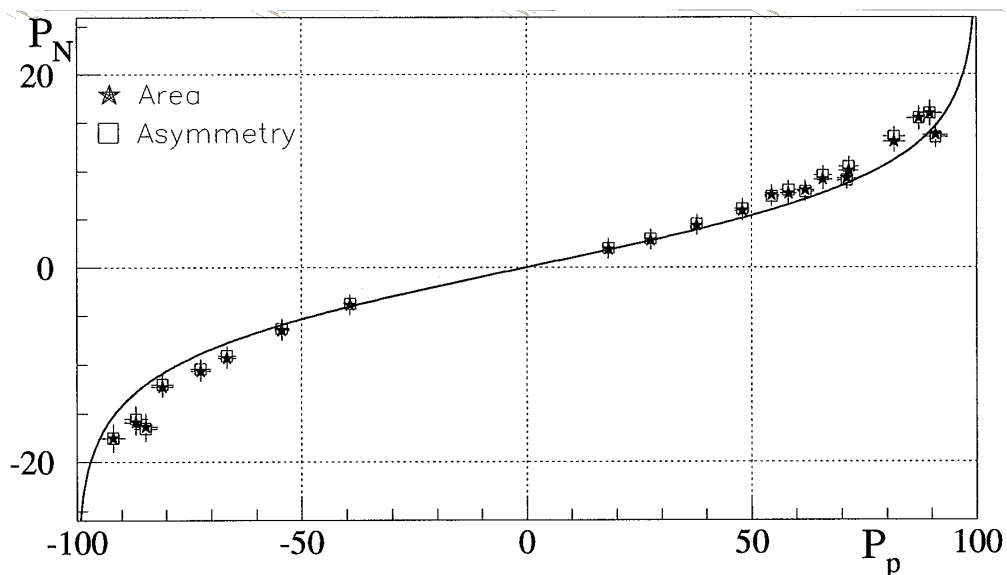


Figure 8.18: This figure shows a test of EST for ammonia. Plotted is the nitrogen polarization versus the proton polarization. The curve shown is the equal spin temperature equation, which shows good agreement with the data. [19]

On a proton target the C_1 correction depends on the cross sections and asymmetries for both protons and deuterons, which vary with Q^2 and x_j . Ref. [55] provides a greater explanation of the proton case.

8.7 Correction for NH_3 in ND_3 (c_2)

The c_2 term in Eq. 8.1 accounts for the contribution of polarized protons in NH_3 to the measured double spin asymmetry. As discussed in Section 8.4.3, the ND_3 target contained a approximately 10.5% (by weight) of hydrogenic material. The protons in this material are polarized by the same mechanism as the deuterons, but with lower efficiency due to the different frequencies that are required. For the pure NH_3 target, c_2 would of course be zero.

From the definition of A_{\parallel} , it is straightforward to show that

$$c_2 = \frac{\eta_p A_p \sigma_p P_p}{\eta_d A_d \sigma_d P_d} \quad (8.21)$$

where the symbols have the same meaning as in Eq. 8.18[55]. The derivation of Eq. 8.21 is valid only if the dilution factor f in Eq. 8.1 is defined using the number of polarizable nucleons in deuterium, not including the free protons, in the numerator of the ratio.

From the discussion above, the ratio of proton to deuteron nuclei is 0.105 ± 0.004 (0.120 ± 0.006) for the inbending (outbending) portion of Part C. The ratio of proton to deuteron polarizations is 2.31 ± 0.2 (2.15 ± 0.3) for the inbending (outbending) portion of Part C[55]. Section 8.3 describes the method for determining the polarization of the contaminating protons. Equation 8.21 then gives:

$$c_2 = (0.24 \pm 0.024) \frac{A_p \sigma_p}{A_d \sigma_d} \quad \text{inbending} \quad (8.22)$$

$$c_2 = (0.26 \pm 0.038) \frac{A_p \sigma_p}{A_d \sigma_d} \quad \text{outbending} \quad (8.23)$$

To evaluate A_p/A_d and σ_p/σ_d , we used the same global fits as for c_1 . The results for c_2 for Part C, in-bending polarity, are shown as a function of x in several Q^2 bins in Fig. 8.19, and vary between 0.51 at low x and 0.23 at high x [55].

8.8 Radiative Corrections

For this analysis the scattering process was approximated as one photon exchange, also known as Born scattering. In reality, there are higher order processes contributing to the total measured cross sections and asymmetries. These processes are taken into

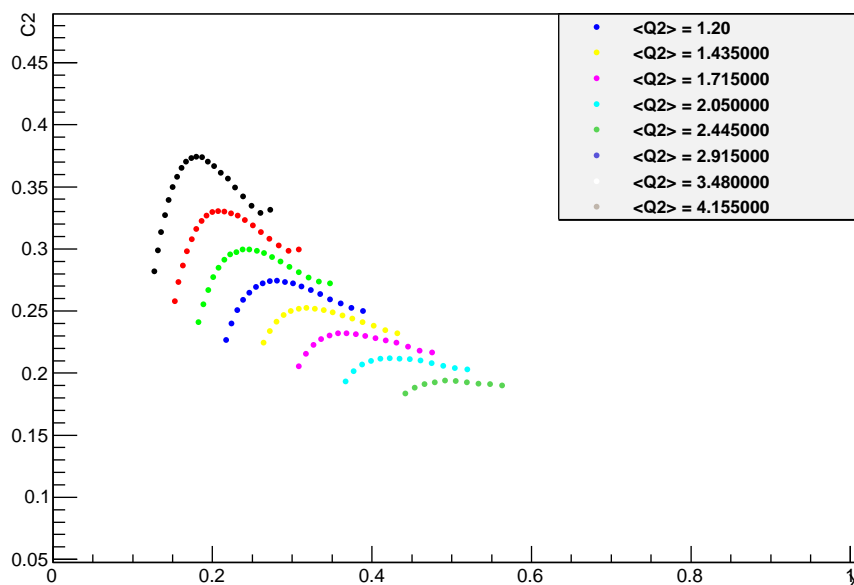


Figure 8.19: Correction factor C_2 as a function of Bjorken X .

consideration with a correction to the asymmetry called “Radiative Corrections.”

The radiative corrections can be broken into 2 kinds: internal and external [27]. The internal processes occur within the field of the scattering nucleus and consist of the Bremsstrahlung, vertex correction, vacuum polarization, and elastic and quasi-elastic scattering contributions [57]. Two of the diagrams which contribute to the internal radiative corrections are shown in Fig 8.20.

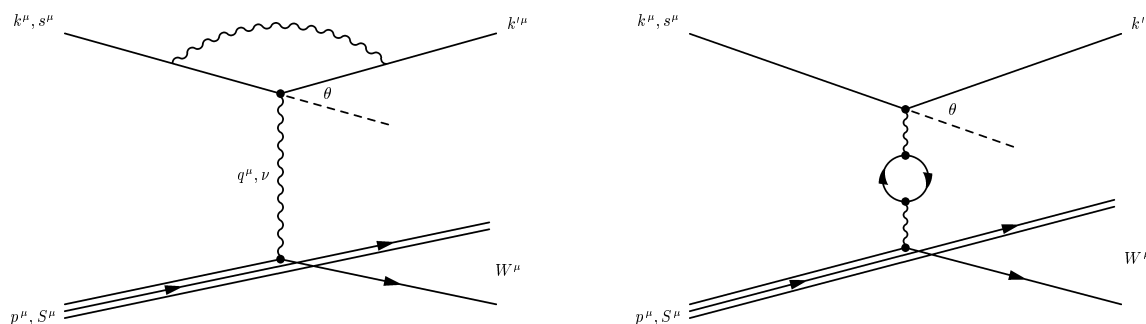


Figure 8.20: Vertex correction diagram (on the left) and vacuum polarization diagram (on the right)

The electron can lose energy while traveling through the target material; the cor-

rections to the asymmetry that result from those processes are the external radiative corrections. These losses can result from the bremsstrahlung radiation by the electron both before and after the scattering event, as illustrated in Fig 8.21, as well as range straggling due to ionization [27].

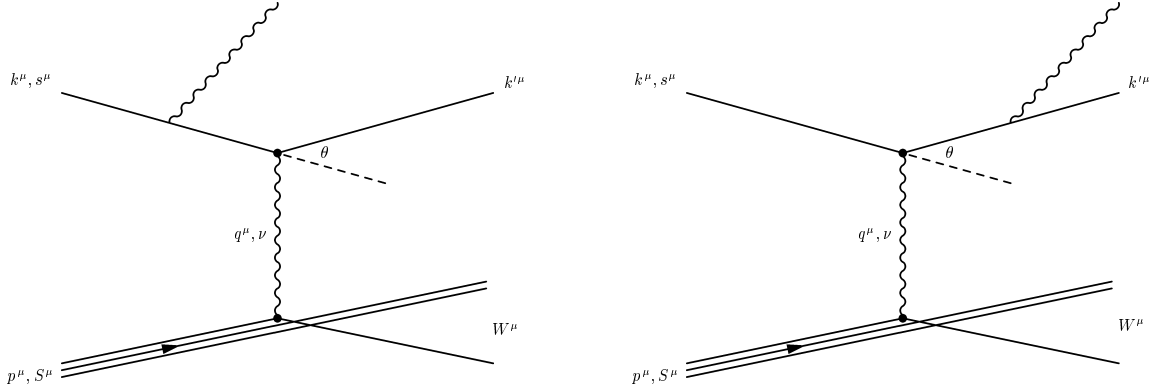


Figure 8.21: Bremsstrahlung radiation can occur before (on the left) and after (on the right) scattering from the nucleus.

The radiative corrections require the evaluation of both polarized and unpolarized components for Born, internally radiated and fully radiated cross sections and asymmetries. Polarization-dependent internal radiative cross sections were calculated using the code developed by Kuchto and Shumeiko [58]. The radiated cross sections can be decomposed as [59]:

$$\begin{aligned}\sigma_r^p &= \sigma_0^p(1 + \delta_v) + \sigma_{el}^p + \sigma_q^p + \sigma_{in}^p \\ \sigma_r^u &= \sigma_0^u(1 + \delta_v) + \sigma_{el}^u + \sigma_q^u + \sigma_{in}^u,\end{aligned}\tag{8.24}$$

where δ_v contains corrections for the electron vertex and vacuum polarization contributions, along with the term left after the infrared-divergent contributions are cancelled out [59]. The terms $\sigma_{el}, \sigma_q, \sigma_{in}$ are due to the internal bremsstrahlung radiation for elastic, quasi-elastic and inelastic processes respectively [27]. The deep-inelastic

component of the polarized cross sections is modeled using Q^2 -dependent fits to A_1 . The polarized resonance region model is based on the parameterization of existing data. The unpolarized cross sections are modeled from fits to structure function data in the deep inelastic region, and fits to cross sections in the resonance region. [27]

The external corrections were based on the work of ref. [60]. In the case of inclusive scattering the main effect of external radiation is the widening of the elastic peak called the “elastic radiative tail” [27]. This occurs because the elastic cross section grows rapidly with the decreasing beam energy; when a high energy photon is radiated, the electron, now lower in energy, has an increased probability of elastically scattering. In general, the external radiative correction depends on the amount of material the electron passes through before and after scattering.

In this correction scheme, the radiative corrections are broken into an additive correction A_{RC} and a “radiative dilution factor” f_{RC} [27]. The additive piece A_{RC} contains the quasi-elastic radiative tail, while the radiative tails of inelastic states are treated as a multiplicative correction to the cross sections. The dilution factor f_{RC} gets small at low x where the radiative corrections are significant from the quasi-elastic tails, and the statistical error bars in this region increase accordingly. The radiatively corrected asymmetry is then given by

$$A_{||} = A_{uncorr}/f_{RC} - A_{RC} \quad (8.25)$$

The result of radiative corrections is shown in Fig 8.22.

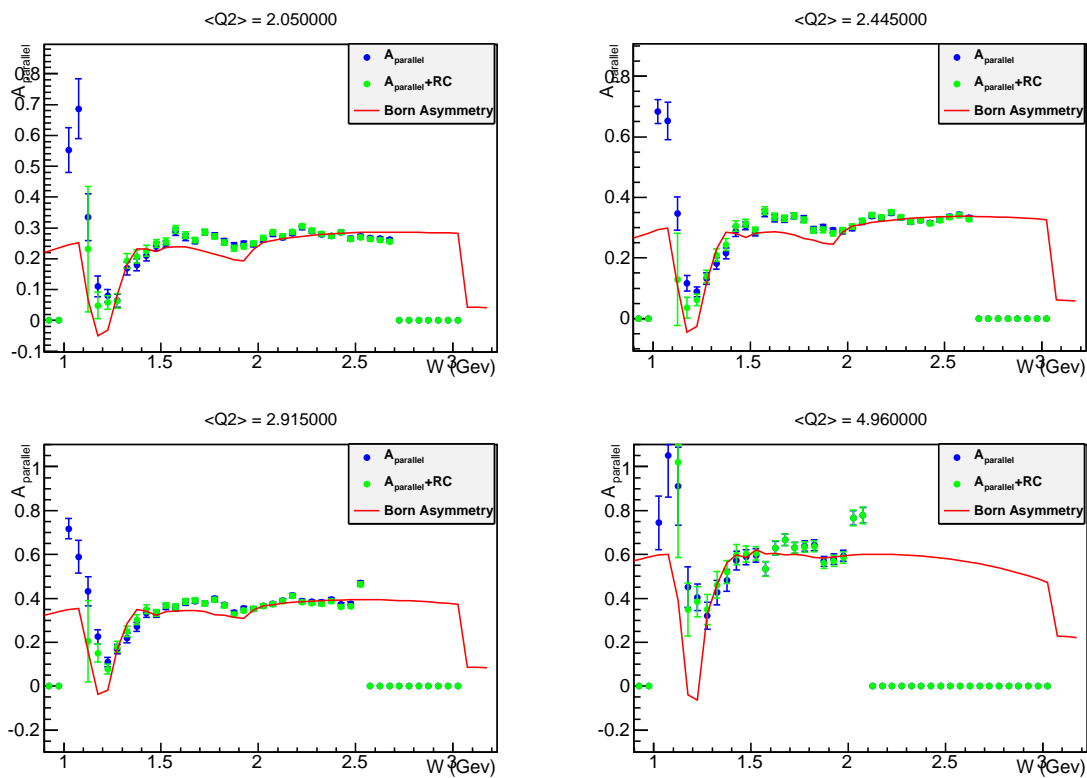


Figure 8.22: Radiatively corrected asymmetry as a function of W shown in four different Q^2 bins. The Born asymmetry is plotted as a red line, while $A_{||}$ is in blue dots. The corrected $A_{||}$ is shown at green squares.

Chapter 9

Results

9.1 g_1/F_1

In the one-photon-exchange (Born) approximation, the cross section for inclusive electron scattering with beam and target spin parallel ($\uparrow\uparrow$) or anti-parallel ($\uparrow\downarrow$) can be expressed in terms of the four structure functions F_1, F_2, g_1 and g_2 , all of which can depend on ν and Q^2 [30]:

$$\begin{aligned} \frac{d\sigma^{\uparrow\downarrow/\uparrow\uparrow}}{d\Omega dE'} &= \sigma_M \left[\frac{F_2}{\nu} + 2 \tan^2 \frac{\theta}{2} \frac{F_1}{M} \pm 2 \tan^2 \frac{\theta}{2} \right. \\ &\quad \left. \times \left(\frac{E + E' \cos \theta}{M\nu} g_1 - \frac{Q^2}{M\nu^2} g_2 \right) \right] \end{aligned} \quad (9.1)$$

where the Mott cross section

$$\sigma_M = \frac{4E'^2 \alpha^2 \cos^2 \frac{\theta}{2}}{Q^4}. \quad (9.2)$$

We can now define the double spin asymmetry $A_{||}$ as

$$A_{||}(\nu, Q^2, y) = \frac{d\sigma^{\uparrow\downarrow} - d\sigma^{\uparrow\uparrow}}{d\sigma^{\uparrow\downarrow} + d\sigma^{\uparrow\uparrow}}. \quad (9.3)$$

Introducing the ratio R of longitudinal to transverse virtual photon absorption cross section,

$$R = \frac{\sigma_L(\gamma^*)}{\sigma_T(\gamma^*)} = \frac{F_2}{2xF_1}(1 + \gamma^2) - 1 \quad (9.4)$$

we can define two additional quantities,

$$\eta = \frac{\epsilon\sqrt{Q^2}}{E - E'\epsilon} \quad (9.5)$$

and the “depolarization factor”

$$D = \frac{1 - E'\epsilon/E}{1 + \epsilon R}, \quad (9.6)$$

which allow us to express $A_{||}$ in terms of the structure functions[30]:

$$\frac{A_{||}}{D} = (1 + \eta\gamma)\frac{g_1}{F_1} + [\gamma(\eta - \gamma)]\frac{g_2}{F_1}. \quad (9.7)$$

9.1.1 $A_{||}$

$A_{||}$ is acquired from the data after the corrections listed in Chapter 8 are applied. Several examples, binned in Q^2 and W , are shown in Fig. 9.1. The combination of the various data sets is discussed further down.

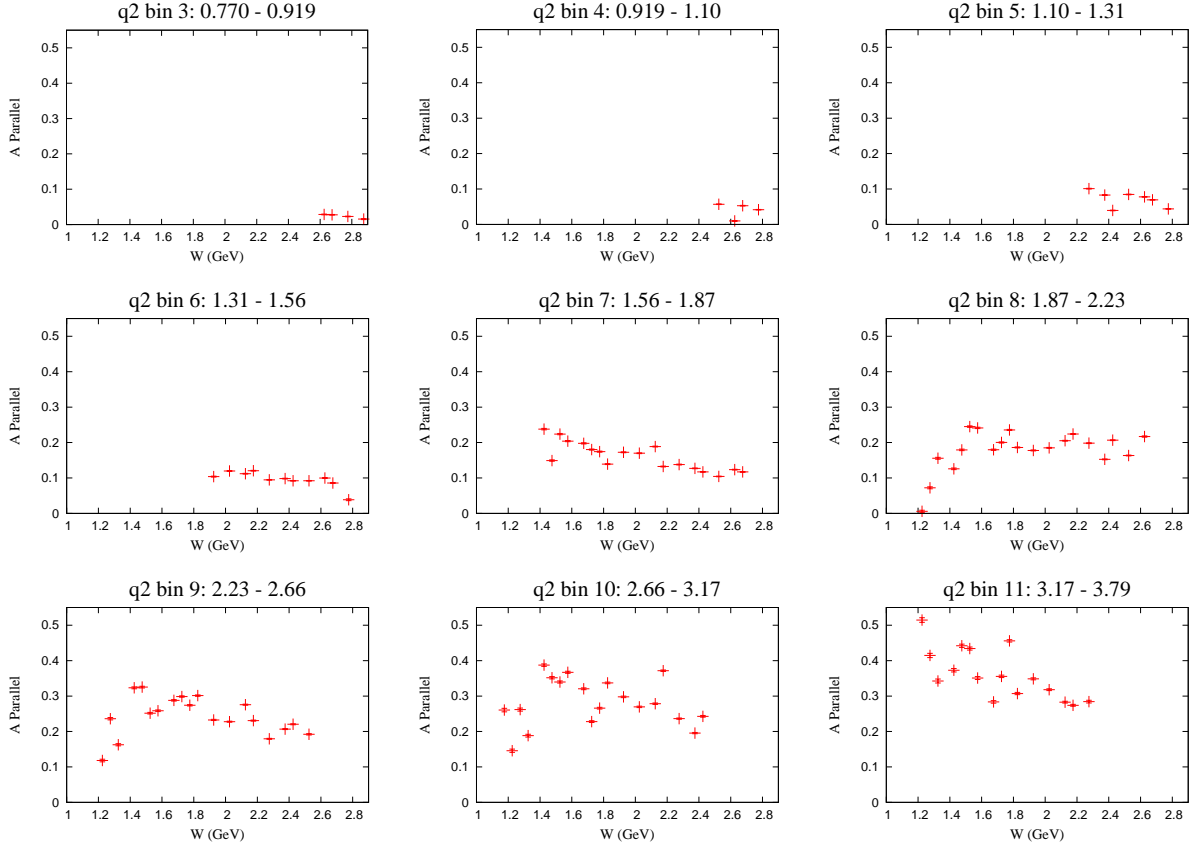


Figure 9.1: A_{\parallel} vs. W for several Q^2 bins for Part C. Statistical error bars are included, but are too small to be visible at this scale in most cases.

9.1.2 Depolarization Factor and R

The depolarization factor, shown in Eq. 9.6, is an important factor in calculating $\frac{g_1}{F_1}$. This factor is a function of R , Eq. 9.4, which is the ratio of the longitudinal to transverse photon absorption cross-section. The values for these factors are supplied from an empirical fit to world data by Christy and Bosted [61]. The cross-section parameterization contained 75 free parameters; among them were parameters for the resonance masses and widths, non-resonance contributions, as well as transition form factors. The fit describes the data well over the range $0 \leq Q^2 \leq 8 \text{ GeV}^2$ and $1.1 \leq W \leq 3.1 \text{ GeV}$ which covers the area of interest for this study [27].

9.1.3 g_2 Correction

As shown in Eq.9.7, A_{\parallel} has two components, one from each of the g_1 and g_2 structure functions. After some algebra, the equations can be re-written in the following form:

$$g_1/F_1 = (A_{\parallel}/D')C_{g_2} \quad (9.8)$$

where the depolarization factor in this case (note that $D \neq D'$) is given by

$$D' = \frac{(1 - \epsilon)(2 - y)}{y(1 + \epsilon R)} \quad (9.9)$$

where $y = \nu/E$. The g_2 correction factor is given by:

$$C_{g_2} = \frac{1 + E'/E^0}{1 + e' \cos(\theta)/E_0} \frac{1}{1 - 2(g_2/g_1)Mx/[E_0 + E' \cos(\theta)]} \quad (9.10)$$

[27] To gauge the rough order of magnitude of the correction, we note that for $\cos(\theta) = 1$, $x = 0.5$, and our beam energy $E = 6$ GeV, then

$$C_{g_2} \approx 1 + (g_2/g_1)/10 \quad (9.11)$$

Since g_2 is smaller in magnitude than g_1 , the overall correction differs by only a few percent from unity, as illustrated in Fig. 9.2.

The values of g_2/g_1 used in the analysis were taken from a fit to world data [62]. In order to estimate the systematic error on the correction, we also used the assumption that there are no deviations from the twist-two model of Wandzura and Wilceck (g_2^{WW}) [63]:

$$g_2(x, Q^2) = -g_1(x, Q^2) + \int_x^1 g_1(\xi, Q^2)d\xi/\xi \quad (9.12)$$

In this relation, the magnitude of g_1 cancels, and the result depends only on the x -dependence at higher x [27]. The corrections C_{g_2} using only the Wandzura and Wilczek contribution are shown as the dashed curves in Fig. 9.2. It can be seen that the difference from the world fit of Ref. [62] are quite small, except for $x = 0.525$ at low Q^2 , which corresponds to the low- W end of the resonance region [27].

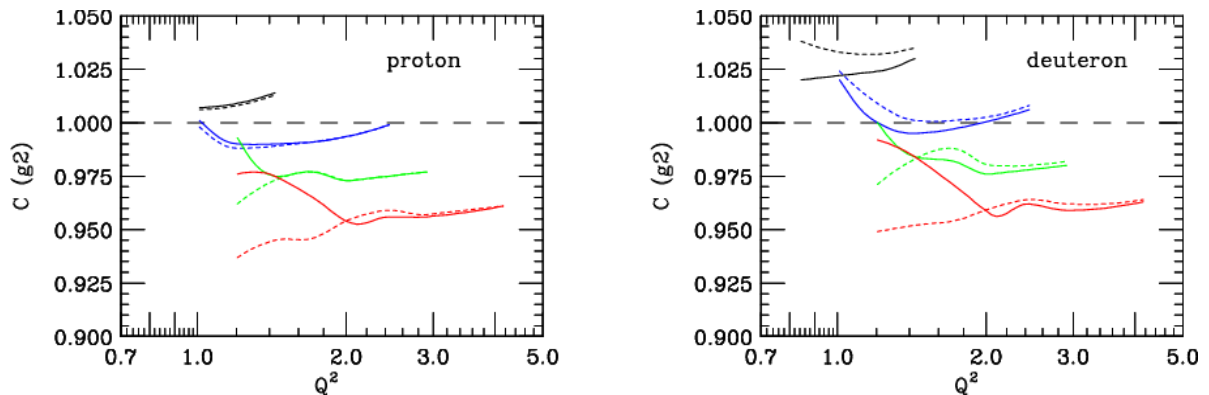


Figure 9.2: Correction factor C_{g_2} as a function of Q^2 for $x = 0.225$ (black), $x = 0.325$ (blue), $x = 0.425$ (green), and $x = 0.525$ (red). Left plot is for the proton target, right panel for the deuteron. Dashed curves use the lowest-twist Wandzura and Wilczek formula, while the solid curves use a fit to world data. [27]

9.1.4 Combining Data Sets

The entire data set for eg1-dvcs is broken up into several groups based on various differences between runs. Parts A and B ran in several sections with different beam energies, whereas Part C had the same beam energy throughout. The main torus polarity was switched (referred to as inbending and outbending) for roughly half of each data set, and the half-wave-plate and target polarizations were switched often as well. For each section of data, defined by these changes, the raw asymmetry is weighted by the appropriate factor. Since the beam polarization does not change with the half-wave-plate, those sections are weighted by their statistical errors. The

target polarization can differ between positive and negative states, so that is used to weight those sections, along with statistics. The other sections are then weighted by their statistics and $P_b P_t$ [27].

9.2 Systematic Errors

Every correction in Eq. 8.1 that is applied to the raw asymmetry introduces some systematic uncertainty. There are also additional sources of error that must be considered. Once these errors are determined, they can be added in quadrature and combined with the statistical error to get the total error on the measurement.

9.2.1 R

The world data used in the fit for R comes from several different sources and covers the range of kinematics useful for this experiment [27]. The overall error amounts to 3%; details of the error for this fit are discussed in [61].

9.2.2 Dilution Factor Systematics

The dilution factor is one of the most important sources of systematic error in the inclusive analysis. There are a number of factors which contribute to this error: the target length L , the ammonia length l_A , the length of the aluminum foils used in the target, and the density of the ammonia. The length and density of the carbon disk used in the carbon target also contribute to the error, but the effect is constrained to the target and ammonia lengths. The parameters for the carbon disk are known to less than a tenth of a percent as well, so the overall error they introduce is miniscule.

To estimate the error, the disparate parameters are separately varied and the

resulting dilution factor is compared to the normal value. The range in L used to find this error is taken from the spread in calculated values of the target length. See Section 8.4.1 for a description of the process used to calculate L . The ammonia length uses a similar calculation, so the range of l_A is determined from the spread in its calculated values in the same way as L . The density of ammonia, both deuterated and not, was taken from the literature, where the errors were listed. See Ref's [64] and [65]. For the length of the aluminum windows, a physical measurement was made and a length was inferred from scattering data. The error is then taken to be the difference between those two values.

The errors from each parameter are added in quadrature and the resulting value of 1.55% for both NH_3 and ND_3 is used as an estimate for the systematic error from the dilution factor. Figure 9.3 shows the error stemming from each of these parameters. As is evident in the graph, none of the errors vary much over the full range of W used in this experiment, so the overall error for the dilution factor will be considered as a normalization error.

9.2.3 Luminosity Dependence of Detection Efficiency

Measured asymmetries can be reduced from true asymmetries if the detection efficiency decreases with the overall rate of particles produced in the target. This occurs because fewer events with the preferred orientation are detected due to the lowered efficiency.

The nominal efficiency, ϵ_n , can be defined as:

$$\epsilon_n = 1 - abR \tag{9.13}$$

where a describes how the efficiency decreases with rate, R is the electron event rate,

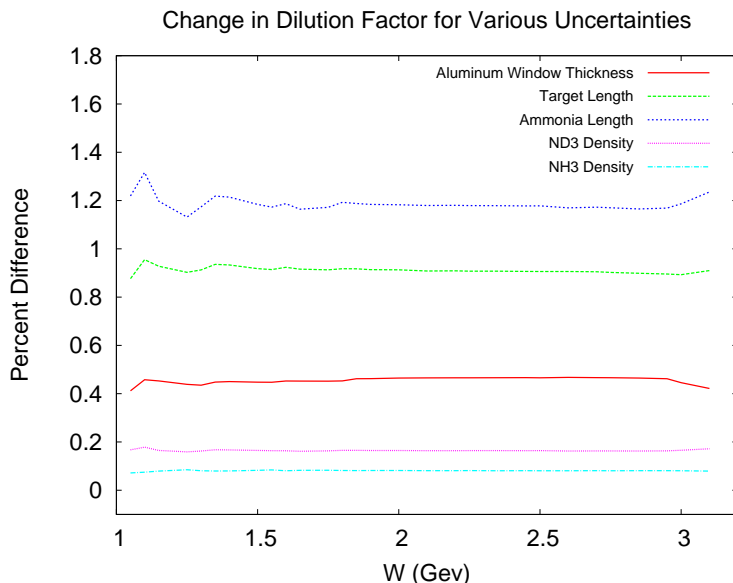


Figure 9.3: Error percentage from changes in the value of the parameters for the dilution factor.

and b is the ratio of the the experimental asymmetry to the asymmetry from all events. If r is the helicity-dependent electron event rate, then the true asymmetry A_t is $\frac{r}{R}$ and it can be shown that:

$$A_m = A_t(1 - aR) \quad (9.14)$$

where A_m is the measured asymmetry. Using Eqn's 9.13 and 9.14 we see that

$$A_m = A_t \frac{1 - \epsilon_n}{b} \quad (9.15)$$

On several occasions, runs were taken with the carbon target with a range of beam currents. The results of the best such study are shown in Fig. 9.4 [27]. It can be seen that there is a clear decrease of rate with increasing beam current, corresponding to about 1%/nA. The other studies were consistent with this result. The most likely cause for this decrease is reduced tracking efficiency with increased “occupancy” in

the drift chambers.

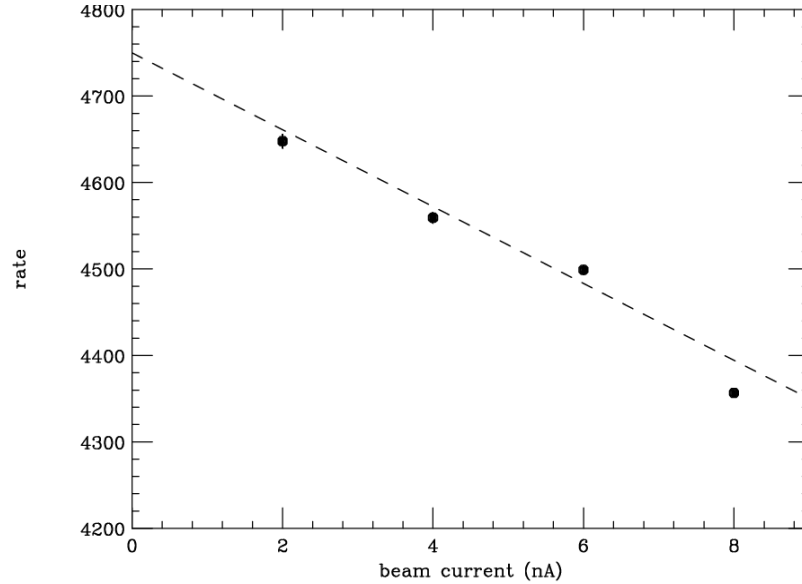


Figure 9.4: Rate of good electrons (counts divided by Faraday Cup reading) as a function of nominal beam current for Carbon target runs 60400 to 60404. The dashed line is a linear fit.

In our case, our typical beam current was 7 nA, and the efficiency decreases by about 1%/nA, yielding $\epsilon_n = 0.07$.

We obtained a rough measure of the total event asymmetry by using events with a “pion” trigger (no Cherenkov counter required), and found it to be at least a factor of ten smaller than the electron asymmetry. Thus, the relative change to A_m from this luminosity effect is less than 0.7%.

9.2.4 Error from beam charge asymmetry

A similar effect as above can arise from a helicity-dependent beam current A_t . A feed-back system was used to keep the average value of A_t well below 0.001 for each run, and below 0.0001 averaged over the entire experiment [27]. Since $A_e > 0.001$ for all kinematics, the net effect is less than 1% relative change in A_e . This possible

systematic error was further reduced to a negligible level by periodically inserting a half-wave plate in the injector, which reversed the beam helicity without affecting the beam current. The total running times with and without the plate inserted were equal within 10%.

9.2.5 Parity-violating background

The measured asymmetry arising due to eN parity-violating inelastic scattering from any of the nucleons in the target is approximately given by $A_{\parallel} = r_T P_B Q^2 [0.8 \times 10^{-4}]$, independent of x , where $r_T = (L^+ - L^-)/(L^+ + L^-)$ is the asymmetry in integrated luminosity with the target polarization aligned (L^+) or anti-aligned (L_-) with the beam direction. [27] Averaged over the entire experiment, $r_T = 0.04$ for NH_3 and $r_T = 0.11$ for ND_3 . Since the measured double-spin raw asymmetry is approximately given by $Q^2 \times 10^{-2}$, the relative parity-violating contribution was less than 0.1% in all (x, Q^2) bins, and was neglected. [27]

9.3 Physics Results

The final physics result from this analysis is the ratio g_1/F_1 for the deuteron. This ratio can be expressed as either a function of Q^2 and W or as a function of Q^2 and x . It is possible to examine it for resonance structure when expressed as a function of Q^2 and W , and when expressed as a function of x , to study QCD evolution.

9.3.1 g_1/F_1 as a function of W in bins of Q^2

Fig. 9.5 shows g_1/F_1 in nine bins of Q^2 for the deuteron. Similar results for the proton can be found in Ref. [27]. The comparison to the world data is reasonably

good; the world fit stems mostly from eg1b data, which had fewer statistics than this analysis. The main peak near $W = 1.5$ GeV appears a bit larger in the data than the fit. The dip just before the peak results from the $\Delta(1232)P_{33}$ resonance, where the asymmetry is expected to be negative. Statistics in that region do not allow for more precise measurements of the Δ transition, compared to eg1b, however.

The systematic errors, discussed in Sec. 9.2, are dominated by an overall normalization uncertainty rather than by point-to-point errors. The largest errors are in $P_b P_t$ and the c_2 correction, which is due mostly to the unexpected hydrogen contamination. The dilution factor presents the next highest error.

9.3.2 Results and Discussion

The results are in reasonable agreement with the published results from the Eg1b experiment [29] and the associated fit used for radiative and other corrections, as represented by the black curves. However, there are still differences on the order of 10% that can be seen, particularly at the lower values of Q^2 .

The data are completely consistent with higher Q^2 data from SLAC [5, 66], shown as the green points. The red and blue curves are pQCD calculations from the LSS group [67]. The curves differ in the gluon polarization: the blue curves are positive $\delta G(x)$ and the red are negative. Both curves use higher twist coefficients that were fit to 2007 data. The difference between the curves is of the same order or larger than our experimental errors. The data shows less Q^2 -dependence than either model; the magnitude of the model curves trends upwards with Q^2 , so it is above the data at low x and below at higher x . A new global pQCD fit that includes our data should be able to significantly improve the determination of higher twist corrections, and start to shed light on $\delta G(x)$. [27]

The data favor the curve for negative gluon polarization in the region of low x . This is suggestive that the gluon polarization will be negative in all regions. RHIC data limit the absolute value of δG to be less than 0.1 in the $0.05 < x < 0.2$ region, but don't determine the sign because they probe δG [68]. This curve corresponds to this value for gluon polarization and makes additional conclusions about the sign. However, further refinement will be needed to settle the spin puzzle once and for all.

Overall, the analysis discussed in this dissertation has been both thorough and meticulous. Excepting the proton contamination of the ND₃ material, the data is of high quality. Even with the contamination, the quantity of data taken outstrips previous measurements. As such, the resulting errors are much smaller and the data provide more information about the spin structure function of the deuteron. The most notable result is the lack of Q^2 dependence for $0.15 < x_b < 0.5$ and $W > 2$ GeV. These results provide important constraints to global pQCD fits to inclusive nucleon structure functions, and pave the way to a larger reach in Q^2 and x with higher energy beams in the future [27].

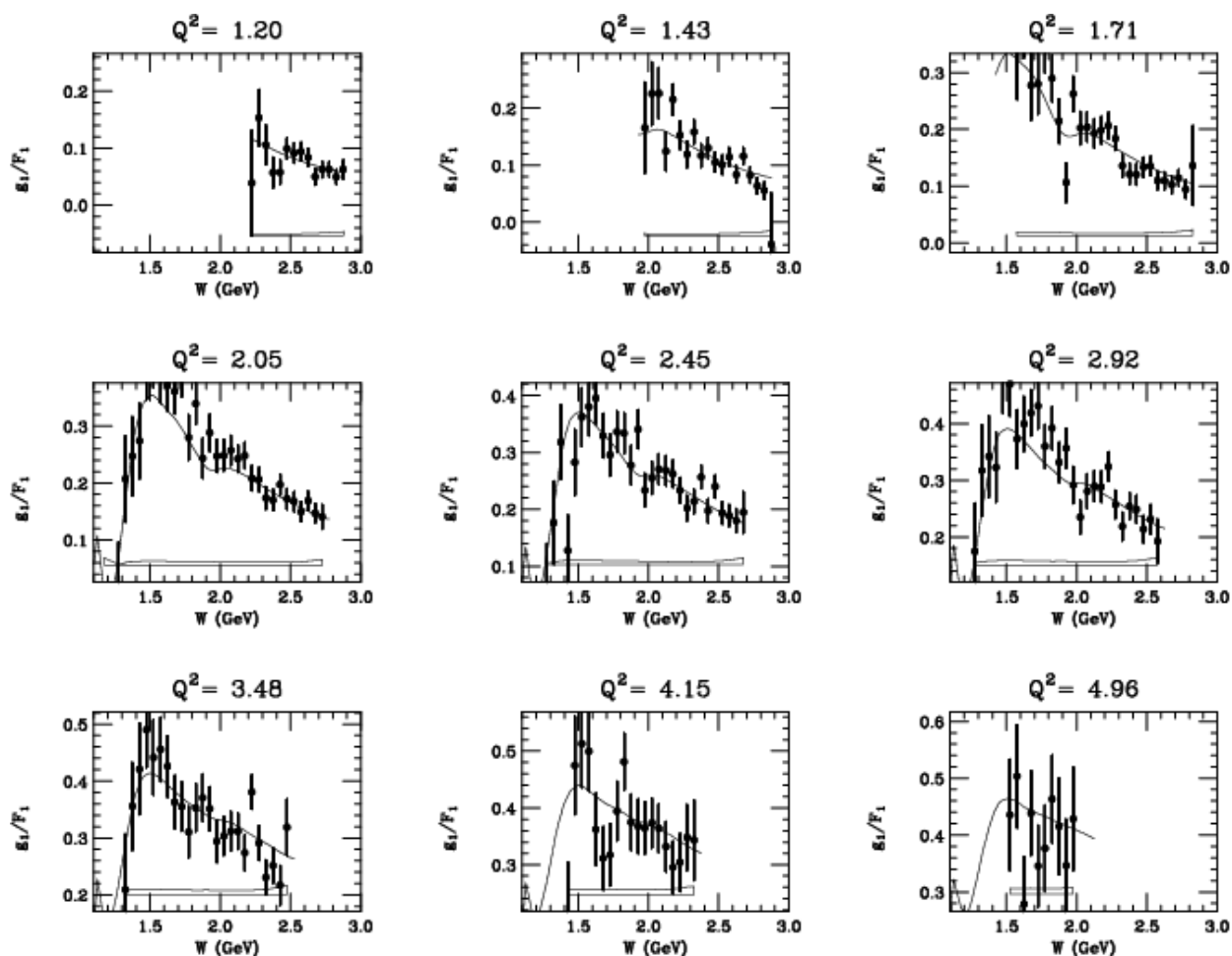


Figure 9.5: Results for g_1/F_1 for the deuteron as a function of W in nine bins of Q^2 . The curves are the fit to previous data (dominated by Eg1b) used for radiative and other corrections. The bands at the bottom of each panel represent the total systematic error. Figure from P. Bosted [27]

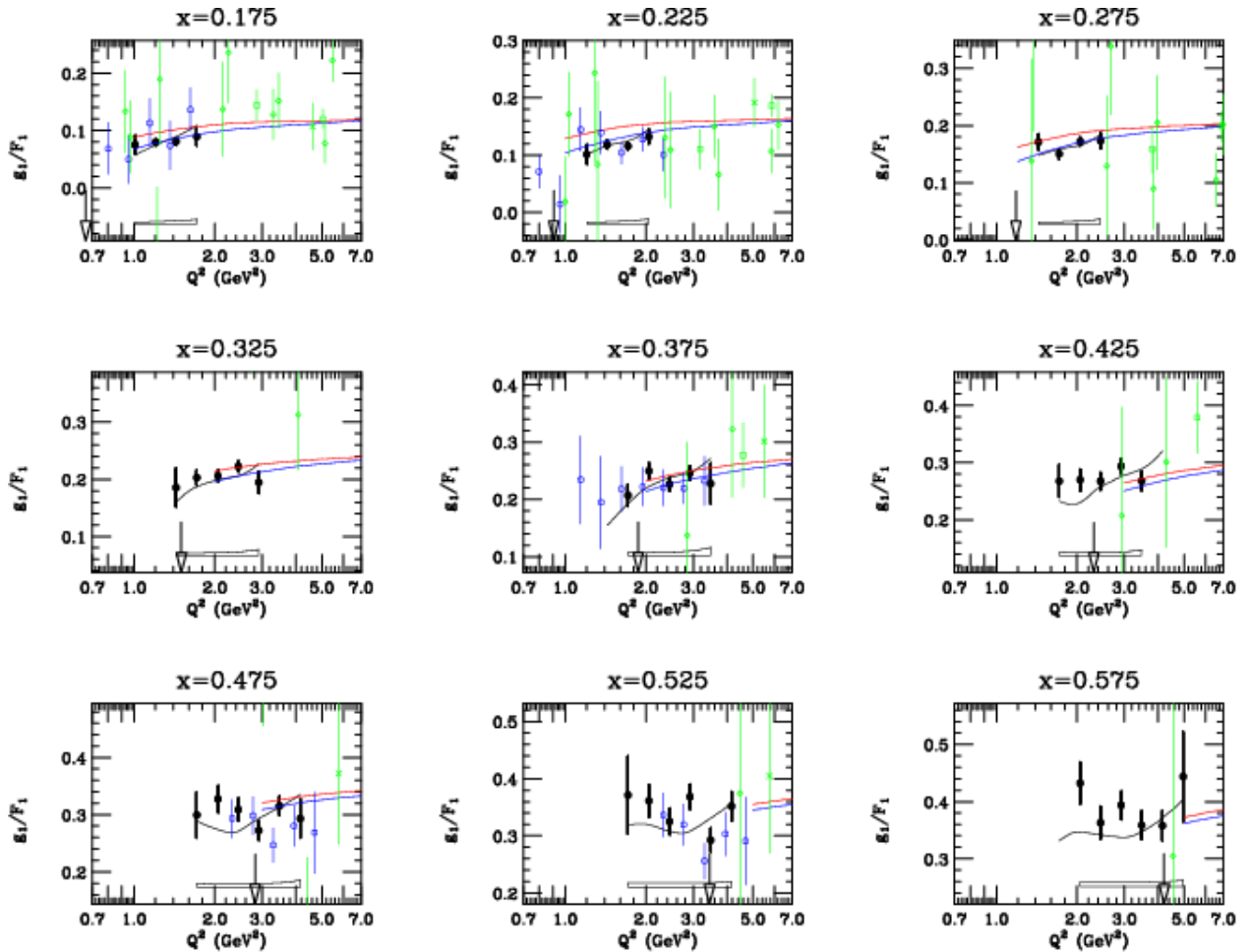


Figure 9.6: Results for g_1/F_1 as a function of Q^2 for the deuteron in nine bins of x . The present results are the black solid points, the published Eg1b results are shown in blue, and results from SLAC [5, 66] are shown in green. The arrows correspond to $W = 2$ GeV. The black curves are the fit to previous data. The bands at the bottom of each panel represent the total systematic error. The red and blue curves are representative pQCD calculation from the LSS group with two models for gluon polarization (positive and negative, respectively). Figure and caption from P. Bosted [27].

Appendix A

Deuteron Polarization Calibration Data

Table A.1: Calibrated Deuteron Polarizations

Run Number	Average Polarization	Max. Polarization	Min. Polarization
60300	24.4	24.3	24.4
60301	24.5	24.4	24.5
60302	22.0	19.8	24.3
60304	25.4	24.9	25.9
60305	26.3	25.9	26.7
60306	26.6	26.5	26.7
60307	27.0	26.5	27.6
60309	27.2	27.0	27.3
60311	28.6	28.2	29.3
60314	30.1	28.8	43.1
60316	22.4	20.8	23.9

Table A.1: Calibrated Deuteron Polarizations

Run Number	Average Polarization	Max. Polarization	Min. Polarization
60317	28.3	28.0	28.6
60319	29.9	29.6	30.1
60320	31.0	30.9	31.1
60322	30.5	29.8	31.3
60324	30.1	28.7	30.9
60325	31.3	30.3	31.8
60326	30.4	29.5	30.8
60327	29.2	29.1	29.4
60330	29.1	29.0	29.4
60331	27.9	26.9	29.0
60332	28.4	25.0	30.2
60333	27.9	22.1	29.6
60343	25.3	24.1	26.1
60344	27.0	26.4	27.5
60345	28.2	27.5	28.8
60346	28.2	27.8	28.7
60347	27.9	27.6	28.4
60348	28.1	27.7	28.3
60349	28.0	27.7	28.5
60350	26.9	24.2	28.5
60351	26.3	15.8	29.4
60354	28.4	28.0	28.7

Table A.1: Calibrated Deuteron Polarizations

Run Number	Average Polarization	Max. Polarization	Min. Polarization
60355	28.2	27.7	28.9
60356	27.6	27.2	27.9
60357	27.9	27.2	28.6
60359	27.6	27.4	27.7
60360	23.9	16.4	28.0
60361	25.9	25.1	26.9
60363	-24.2	-24.5	-23.3
60364	-23.8	-24.9	-18.2
60366	-24.5	-24.7	-24.2
60367	-24.3	-24.3	-24.3
60369	-28.0	-28.5	-27.7
60371	-27.6	-27.9	-27.3
60372	-27.6	-27.8	-27.4
60373	-27.4	-27.6	-27.2
60374	-27.3	-27.6	-26.9
60376	-27.3	-27.6	-27.0
60377	-27.1	-27.2	-27.0
60378	-26.9	-27.1	-26.3
60379	-26.1	-26.9	-25.6
60381	-26.8	-27.1	-26.0
60382	-26.4	-26.8	-26.2
60383	-26.1	-26.3	-25.8

Table A.1: Calibrated Deuteron Polarizations

Run Number	Average Polarization	Max. Polarization	Min. Polarization
60384	-26.0	-26.2	-25.7
60385	-25.7	-26.0	-25.5
60387	-25.4	-25.7	-25.2
60388	-25.0	-25.5	-24.4
60389	-24.6	-25.0	-23.6
60390	-24.4	-24.8	-23.8
60392	-23.8	-24.1	-23.5
60411	31.7	31.5	31.8
60412	31.2	30.9	31.6
60413	31.2	30.9	31.5
60414	30.3	29.7	30.8
60416	30.0	29.8	30.2
60417	30.1	29.6	30.4
60418	30.1	29.8	30.4
60419	29.6	29.3	30.0
60421	29.1	28.8	29.3
60422	28.7	28.5	29.0
60423	28.4	28.2	28.8
60424	28.3	28.2	28.4
60425	28.2	28.1	28.3
60427	28.2	28.1	28.2
60428	27.9	27.6	28.2

Table A.1: Calibrated Deuteron Polarizations

Run Number	Average Polarization	Max. Polarization	Min. Polarization
60429	27.5	27.0	27.7
60430	27.2	26.5	27.5
60431	26.8	26.4	27.1
60432	26.6	26.1	27.0
60436	27.3	24.1	29.4
60437	30.4	29.9	30.9
60439	31.0	30.6	31.3
60440	31.2	30.9	31.4
60441	31.5	30.9	32.2
60442	31.2	30.8	31.5
60444	30.3	29.6	30.8
60445	29.7	29.5	30.0
60446	29.4	29.2	29.8
60447	28.9	28.4	29.4
60449	28.8	28.5	29.1
60450	28.3	28.1	28.6
60451	28.1	27.9	28.4
60452	27.8	27.6	28.0
60453	27.5	27.0	27.6
60454	27.2	26.9	27.4
60458	-21.9	-22.3	-21.0
60459	-21.7	-22.0	-21.5

Table A.1: Calibrated Deuteron Polarizations

Run Number	Average Polarization	Max. Polarization	Min. Polarization
60460	-21.3	-21.9	-21.0
60462	-21.7	-24.4	-21.2
60463	-27.2	-27.5	-26.2
60464	-27.7	-28.0	-27.5
60466	-28.3	-28.3	-28.2
60468	-28.0	-28.2	-27.4
60469	-27.6	-27.9	-26.8
60470	-24.2	-28.6	-3.3
60471	-28.8	-29.7	-24.0
60473	-29.6	-29.7	-29.4
60474	-29.3	-29.5	-29.1
60475	-28.9	-29.2	-28.6
60476	-28.5	-28.7	-28.4
60478	-28.2	-28.5	-28.0
60479	-27.8	-28.0	-27.5
60480	-27.5	-27.6	-27.3
60481	-27.2	-27.5	-26.8
60483	-27.0	-27.2	-26.7
60484	-26.5	-26.9	-26.1
60485	-26.2	-26.4	-26.0
60486	-26.0	-26.2	-25.8
60496	-36.6	-37.0	-36.1

Table A.1: Calibrated Deuteron Polarizations

Run Number	Average Polarization	Max. Polarization	Min. Polarization
60497	-34.7	-35.6	-33.8
60498	-33.4	-33.7	-32.6
60499	-31.7	-32.6	-30.6
60500	-29.7	-30.7	-28.5
60501	-27.9	-28.5	-27.0
60502	-27.9	-28.0	-27.7
60503	-27.3	-27.8	-26.6
60504	-26.7	-27.0	-26.6
60505	-26.3	-26.9	-25.9
60507	-25.7	-26.0	-25.5
60508	-25.5	-25.6	-25.3
60509	-25.3	-25.5	-25.2
60514	35.3	29.6	38.6
60515	40.0	38.7	40.6
60517	40.7	40.4	41.0
60518	40.1	39.6	40.6
60519	40.3	39.8	40.9
60520	39.3	38.6	40.3
60522	38.1	37.6	38.8
60523	37.5	36.5	38.1
60524	33.7	32.8	34.3
60525	33.0	32.4	33.3

Table A.1: Calibrated Deuteron Polarizations

Run Number	Average Polarization	Max. Polarization	Min. Polarization
60526	32.7	32.2	33.1
60527	32.3	31.7	32.7
60528	31.8	31.5	32.1
60530	31.6	31.5	31.7
60531	31.4	30.6	31.8
60532	31.0	30.3	31.2
60533	30.4	29.8	31.1
60534	29.9	29.5	30.3
60535	29.6	29.2	30.1
60537	29.6	29.5	29.8
60538	29.3	28.8	30.2
60539	28.8	28.4	29.3
60553	-33.7	-37.6	-31.4
60554	-29.6	-31.3	-28.2
60557	-32.2	-33.2	-31.1
60558	-30.6	-31.0	-30.1
60559	-29.1	-29.9	-28.5
60560	-27.6	-28.4	-26.9
60561	-26.6	-26.9	-26.3
60562	-26.0	-26.4	-25.2
60563	-25.7	-26.1	-24.7
60564	-24.9	-25.2	-24.7

Table A.1: Calibrated Deuteron Polarizations

Run Number	Average Polarization	Max. Polarization	Min. Polarization
60566	-29.6	-30.6	-26.5
60567	-29.6	-30.2	-28.9
60568	-28.8	-29.1	-28.4
60569	-27.6	-28.5	-26.9
60570	-26.4	-26.9	-25.9
60572	-25.6	-26.3	-25.1
60573	-24.6	-25.0	-24.1
60574	-24.1	-24.2	-23.9
60577	42.1	41.3	42.5
60578	41.2	40.4	42.2
60579	40.3	39.7	41.0
60580	39.1	38.0	39.9
60582	37.6	37.0	38.1
60584	37.2	37.0	37.5
60585	36.7	36.0	37.1
60586	36.0	35.6	36.4
60588	35.5	35.0	35.9
60589	34.9	34.6	35.3
60590	34.5	34.1	34.7
60591	34.0	33.4	34.4
60592	34.1	33.9	34.4
60594	33.8	33.4	34.2

Table A.1: Calibrated Deuteron Polarizations

Run Number	Average Polarization	Max. Polarization	Min. Polarization
60603	40.9	37.8	41.7
60604	40.5	39.1	41.4
60605	38.8	38.1	39.3
60607	37.8	37.3	38.3
60608	37.4	37.2	37.6
60609	37.0	36.5	37.5
60610	36.3	35.9	36.6
60612	35.6	35.1	36.1
60613	34.9	34.5	35.3
60614	34.5	34.3	34.8
60615	33.8	33.3	34.3
60619	-29.0	-29.7	-28.0
60620	-28.2	-28.9	-27.3
60622	-26.5	-26.8	-25.9
60623	-26.2	-26.8	-25.5
60624	-25.2	-25.6	-24.9
60625	-24.3	-24.8	-23.9
60627	-23.7	-23.9	-23.4
60628	-23.5	-23.8	-23.2
60629	-23.3	-23.5	-23.1
60642	-29.5	-30.0	-29.1
60643	-29.1	-29.4	-28.7

Table A.1: Calibrated Deuteron Polarizations

Run Number	Average Polarization	Max. Polarization	Min. Polarization
60644	-27.7	-28.5	-26.9
60645	-26.5	-27.0	-26.0
60647	-25.4	-25.9	-25.1
60648	-25.0	-25.2	-24.9

Bibliography

- [1] Herman Melville. *Moby Dick*. 1851.
- [2] Harold C. Urey, F. G. Brickwedde, and G. M. Murphy. A hydrogen isotope of mass 2 and its concentration. *Phys. Rev.*, 40:1–15, Apr 1932.
- [3] P. A. M. Dirac. The Quantum Theory of the Electron. *Proceedings of the Royal Society of London. Series A*, 117(778):610–624, 1928.
- [4] Jonathan Mulholland. *SANE's Measurement of the Proton's Virtual Photon Spin Asymmetry, A_1^p , at Large Bjorken x* . PhD thesis, University of Virginia, 2012.
- [5] Abe, K. et. al. (E143 Collaboration). Measurements of the proton and deuteron spin structure functions g_1 and g_2 . *Phys. Rev. D*, 58:112003, Oct 1998.
- [6] Nicholas Alfred Jelley. *Fundamentals of nuclear physics*. Cambridge University Press, 1990.
- [7] Michael E Peskin and Daniel V Schroeder. Quantum field theory. *The Advanced Book Program, Perseus Books (Reading, Massachusetts, 1995*.
- [8] Francis Halzen and Alan Douglas Martin. Quarks and leptons: An introductory course in modern particle physics. 1984.

- [9] Christoph W Leemann, David R Douglas, and Geoffrey A Krafft. The continuous electron beam accelerator facility: Cebaf at the jefferson laboratory. *Annual Review of Nuclear and Particle Science*, 51(1):413–450, 2001.
- [10] J. Pierce. *Double Spin Asymmetry in Exclusive π^+ Electroproduction with CLAS*. PhD thesis, University of Virginia, 2008.
- [11] T. Maruyama, E. L. Garwin, R. Prepost, and G. H. Zapalac. Electron-spin polarization in photoemission from strained gaas grown on gaas_{1-x}p_x. *Phys. Rev. B*, 46:4261–4264, Aug 1992.
- [12] James Maxwell. *SANE’s Measurement of the Proton’s Virtual Photon Spin Asymmetry, A1p, at Large Bjorken x*. PhD thesis, University of Virginia, 2011.
- [13] B.A. Mecking, et. al. The CEBAF Large Acceptance Spectrometer (CLAS). *Nuclear Instruments and Methods in Physics Research Section A: Accelerators, Spectrometers, Detectors and Associated Equipment*, 503(3):513 – 553, 2003.
- [14] F. X. Girod *et al.*, [The CLAS Collaboration]. Measurement of deeply virtual compton scattering beam-spin asymmetries. *Phys. Rev. Lett.*, 100:162002, Apr 2008.
- [15] Sucheta Jawalkar. *Measurement of Single and Double Spin Asymmetries in $\vec{p}(e, e'\pi^{\pm,0})X$ Semi-Inclusive Deep-Inelastic Scattering*. PhD thesis, College of William and Mary, 2012.
- [16] et. al. [The CLAS Collaboration] G. Adams, V. Burkert. The {CLAS} cherenkov detector. *Nuclear Instruments and Methods in Physics Research Section A: Accelerators, Spectrometers, Detectors and Associated Equipment*, 465(23):414 – 427, 2001.

- [17] et al. [The CLAS Collaboration] M. Amarian, G. Asryan. The {CLAS} forward electromagnetic calorimeter. *Nuclear Instruments and Methods in Physics Research Section A: Accelerators, Spectrometers, Detectors and Associated Equipment*, 460(23):239 – 265, 2001.
- [18] DG Crabb and W Meyer. Solid polarized targets for nuclear and particle physics experiments. *Annual Review of Nuclear and Particle Science*, 47(1):67–109, 1997.
- [19] B. Adeva *et al.* [The Spin Muon Collaboration]. Nucl. Instrum. Meth. A 419 60, (1998).
- [20] W. Meyer, K.H. Althoff, V. Burkert, U. Hartfiel, T. Hewel, O. Kaul, G. Knop, E. Kohlgarth, H.D. Schablitzky, E. Schilling, and W. Thiel. Tensor polarization of deuterons in irradiated nd3. *Nuclear Instruments and Methods in Physics Research Section A: Accelerators, Spectrometers, Detectors and Associated Equipment*, 244(3):574 – 576, 1986.
- [21] C. Dulya, D. Adams, et. al. A line-shape analysis for spin-1 nmr signals. *Nuclear Instruments and Methods in Physics Research Section A: Accelerators, Spectrometers, Detectors and Associated Equipment*, 398(23):109 – 125, 1997.
- [22] C.D Keith, M Anghinolfi, M Battaglieri, P Bosted, D Branford, S Bltman, V.D Burkert, S.A Comer, D.G Crabb, R De Vita, G Dodge, R Fatemi, D Kashy, S.E Kuhn, Y Prok, M Ripani, M.L Seely, M Taiuti, and S Witherspoon. A polarized target for the clas detector. *Nuclear Instruments and Methods in Physics Research Section A: Accelerators, Spectrometers, Detectors and Associated Equipment*, 501(23):327 – 339, 2003.
- [23] Yelena Prok. *GDH Integral on the Proton from Asymmetries*. PhD thesis, University of Virginia, 2004.

- [24] G.R. Court, D.W. Gifford, P. Harrison, W.G. Heyes, and M.A. Houlden. A high precision q-meter for the measurement of proton polarization in polarised targets. *Nuclear Instruments and Methods in Physics Research Section A: Accelerators, Spectrometers, Detectors and Associated Equipment*, 324(3):433 – 440, 1993.
- [25] C.D. Keith *et al.*,. *Nucl. Instr. Meth.*, **501**(327), (2003).
- [26] P. Bosted and S. Jawalkar. eg1-dvcs Technical Note 08. <http://www.jlab.org/Hall-B/secure/eg1-dvcs/technotes/LandLAv2/LandLA.pdf>, accessed Dec. 2012.
- [27] N. Kvaltine P. E. Bosted, Y. Prok. Inclusive Polarized Structure Functions g_1^p and g_1^d from the eg1-dvcs Experiment, 2012.
- [28] R. Fatemi *et al.* (CLAS Collaboration). *Phys. Rev. Lett.*, 91:222002, (2003).
- [29] Y. Prok *et al.* (CLAS Collaboration). *Phys. Lett. B*, 672(12), (2009).
- [30] R.G. Fersch *et al.*, [The CLAS Collaboration]. to be published, accessed Dec. 2012.
- [31] P. Bosted and S. Jawalkar. eg1-dvcs Technical Note 07. <http://wwwold.jlab.org/Hall-B/secure/eg1-dvcs/technotes/nt22/nt22.pdf>, accessed Dec. 2012.
- [32] P Bosted. eg1-dvcs Technical Note 04. http://wwwold.jlab.org/Hall-B/secure/eg1-dvcs/technotes/targetinfo/target_info.pdf, accessed Dec. 2012.
- [33] M. Aghasyan. eg1-dvcs Technical Note 01. <http://wwwold.jlab.org/Hall-B/secure/eg1-dvcs/technotes/FCandHel/FCandHelicity.pdf>, accessed Dec. 2012.

- [34] B. Zhao. eg1-dvcs Technical Note 10. <http://www.jlab.org/Hall-B/secure/eg1-dvcs/technotes/DCAalign/DCAalign.pdf>, accessed Dec. 2012.
- [35] S. Jawalkar. http://clasweb.jlab.org/rungroups/eg1-dvcs/wiki/index.php/Drift_Chamber_Calibration, accessed Dec. 2012.
- [36] M. Ungaro. https://userweb.jlab.org/~ungaro/maureepage/proj/Cerenkov/cc_periods/eg1dvcs.html, accessed Dec. 2012.
- [37] P. Bosted and A. Kim. eg1-dvcs Technical Note 02. <http://wwold.jlab.org/Hall-B/secure/eg1-dvcs/technotes/raster.pdf>, accessed Dec. 2012.
- [38] P. Bosted. eg1-dvcs Analysis Archive. http://clasweb.jlab.org/rungroups/eg1-dvcs/wiki/index.php/Even_newer_IC_shadow_cut%2C_and_new_track_quality_cut, accessed Dec. 2012.
- [39] P. Bosted. eg1-dvcs Technical Note 12. <http://wwold.jlab.org/Hall-B/secure/eg1-dvcs/technotes/cc2/cc2.pdf>, accessed Dec. 2012.
- [40] P. Bosted. eg1-dvcs Technical Note 13. <http://wwold.jlab.org/Hall-B/secure/eg1-dvcs/technotes/fidcutic/fidic.pdf>, accessed Dec. 2012.
- [41] Y. Prok. eg1-dvcs Technical Note 09. <http://wwold.jlab.org/Hall-B/secure/eg1-dvcs/technotes/rastercheck/rasterTN.pdf>, accessed Dec. 2012.
- [42] A. Kim. eg1-dvcs Technical Note 22. <http://wwold.jlab.org/Hall-B/secure/eg1-dvcs/technotes/BadFileList/BadFileList.pdf>, accessed Dec. 2012.
- [43] P. Bosted. eg1-dvcs Technical Note 05. <http://wwold.jlab.org/Hall-B/secure/eg1-dvcs/technotes/radcor/radcor.pdf>, accessed Dec. 2012.

- [44] P. Bosted. eg1-dvcs Technical Note 06. <http://wwold.jlab.org/Hall-B/secure/eg1-dvcs/technotes/eleceff/eleceff.pdf>, accessed Dec. 2012.
- [45] P. Bosted. eg1-dvcs Technical Note 11. <http://wwold.jlab.org/Hall-B/secure/eg1-dvcs/technotes/momcorr/momcorr.pdf>, accessed Dec. 2012.
- [46] P. Bosted and A. Kim. eg1-dvcs Technical Note 03. <http://wwold.jlab.org/Hall-B/secure/eg1-dvcs/technotes/energy/energy.pdf>, accessed Dec. 2012.
- [47] N. Kvaltine. eg1-dvcs Technical Note 15. <http://www.jlab.org/Hall-B/secure/eg1-dvcs/technotes/deuteronTargetCalibration/DeuteronTargetCalibration.pdf>, accessed Dec. 2012.
- [48] P. Bosted. eg1-dvcs Technical Note 17. <http://wwold.jlab.org/Hall-B/secure/eg1-dvcs/hind/hind.pdf>, accessed Dec. 2012.
- [49] Particle Data Group's Atomic and Nuclear Properties of Materials. <http://pdg.lbl.gov/2011/AtomicNuclearProperties/>, June 2012.
- [50] O. Rondon. Density of Ammonia at the Boiling Point of Nitrogen. *UVA Internal Report*, 1993.
- [51] S. Koirala. eg1-dvcs Technical Note 17 prime. <http://www.jlab.org/Hall-B/secure/eg1-dvcs/technotes/hind/hindSuman.pdf>, accessed Dec. 2012.
- [52] P. Bosted. Pair-Symmetric and Pion Backgrounds for EG1b. CLAS-NOTE, 2004-2005.
- [53] J. Beringer et al. (Particle Data Group). Phys. Rev. D86, 010001, (2012).
- [54] D. Wiser. PhD thesis, University of Wisconsin, 1977.

- [55] Y. Prok. eg1-dvcs Technical Note 14. <http://www.jlab.org/Hall-B/secure/eg1-dvcs/yprok/n14/n14note.pdf>, accessed Dec. 2012.
- [56] O.A. Rondon. Phys. Rev. C 60 035201, (1999).
- [57] Gregory S. Mitchell. *A precision measurement of the spin structure function $g_1(x, Q^2)$ for the proton and deuteron*. PhD thesis, 2000.
- [58] T.V. Kuchto and N.M. Shumeiko. Radiative effects in deep inelastic scattering of polarized leptons by polarized nucleons. *Nuclear Physics B*, 219(2):412 – 436, 1983.
- [59] K. Abe *et al.*,. Slac e143. Phys. Rev. Lett. 74 (1995) 346; Phys. Rev. Lett. 75 (1995) 25; Phys. Lett. B364 (1995) 61; Phys. Rev. D58, 112003 (1998).
- [60] L. W. MO and Y. S. TSAI. Radiative corrections to elastic and inelastic ep and up scattering. *Rev. Mod. Phys.*, 41:205–235, Jan 1969.
- [61] M.E. Christy and P.E. Bosted. “Empirical Fit to Precision Inclusive Electron-Proton Cross Sections in the Resonance Region”. Phys. Rev. C 81, 055213 (2010). (arXiv:0712.3731).
- [62] S. Kuhn *et al.*, N. Guler. to be published.
- [63] S. Wandzura and F. Wilczek. Phys. Lett. B72 195, (1977).
- [64] O. Rondon. UVa Internal Report, 1993.
- [65] I. Fisk. UVa Internal Report, 1993.
- [66] P. L. Anthony *et al.*,. Slac e155. Phys. Lett. B463 339, (1999).
- [67] A. V. Sidorov E. Leader and D. B. Stamenov. Phys. Rev. D **73**, 034023, (2006).

- [68] Daniel de Florian, Rodolfo Sassot, Marco Stratmann, and Werner Vogelsang. Global analysis of helicity parton densities and their uncertainties. *Phys. Rev. Lett.*, 101:072001, Aug 2008.